Theoretical Investigations of Electronic Structure and Opto-electronic Properties of a few DNA and Modified DNA Systems

A Thesis

Submitted for the Degree of

DOCTOR OF PHILOSOPHY

in the Faculty of Science

by

Pralok Kumar Samanta

THEORETICAL SCIENCES UNIT
JAWAHARLAL NEHRU CENTRE FOR ADVANCED SCIENTIFIC RESEARCH
Bangalore – 560 064

FEBRUARY 2014

To my family

DECLARATION

I hereby declare that the matter embodied in the thesis entitled "**Theoretical Investigations of Electronic Structure and Opto-electronic Properties of a few DNA and Modified DNA Systems**" is the result of investigations carried out by me at the Theoretical Sciences Unit, Jawaharlal Nehru Centre for Advanced Scientific Research, Bangalore, India under the supervision of Prof. Swapan K. Pati and that it has not been submitted elsewhere for the award of any degree or diploma.

In keeping with the general practice in reporting scientific observations, due acknowledgement has been made whenever the work described is based on the findings of other investigators.

Pralok Kumar Samanta

CERTIFICATE

I hereby certify that the matter embodied in this thesis entitled "**Theoretical Investigations of Electronic Structure and Opto-electronic Properties of a few DNA and Modified DNA Systems**" has been carried out by Mr. Pralok Kumar Samanta at the Theoretical Sciences Unit, Jawaharlal Nehru Centre for Advanced Scientific Research, Bangalore, India under my supervision and that it has not been submitted elsewhere for the award of any degree or diploma.

Prof. Swapan K. Pati
(Research Supervisor)

Acknowledgements

"As we express our gratitude, we must never forget that the highest appreciation is not to utter words, but to live by them." -John Fitzgerald Kennedy

I know that a few sentences are not enough to thank all the people who have helped me to overcome the obstacles in my journey, words really fail me! Still I would like to take this opportunity to show up how grateful I am to them.

First of all, I would like to thank my research supervisor, Prof. Swapan K. Pati, for helping me to be what I am as a researcher today. Working with him has been a thoroughly enjoyable experience. The freedom of expression that I have enjoyed with him has been so very instrumental in building up my confidence like nothing else has ever been. I am very much fortunate to have been able to work with such a wonderful person.

I have also been very fortunate to attend excellent courses here at JNCASR. Many thanks to Prof. Subir K. Das, Prof. Shobhana Narasimhan, Prof. N. S. Vidhyadhiraja, Prof. S. Balasubramanian, Prof. Aloknath Chakraborty (IISc), Prof. Hemalatha Balaram and Prof. Swapan K. Pati.

I thank CSIR for research fellowship.

I am grateful to JNCASR for providing a world class environment in

which to do research. I would like to thank all the administrative, technical, Complab, Dhanvantari and TUE-CMS staffs, whose work behind the scenes keeps *our* work running. I would like to thank the Indo-Italian project, which made it possible for me to work with our collaborators in Italy.

I thank all my excellent collaborators Prof. Anna Painelli (Università degli Studi di Parma, Italy), Prof. T. K. Maji, Prof. T. Govindraju, Dr. Debabrata Maity, M. B. Avinash, Ritesh Halder and N. Nagarjun. Special acknowledgement is to Prof. Anna Painelli, with whom I enjoyed working during a month long project in Italy twice. I owe special gratitude to her student Dr. Cristina Sissa. Apart from working together, her constant guidance in Italy never let me feel I was in a foreign country.

This acknowledgement would be incomplete without thanking my labmates. Research has its ups and downs, and it is hard to imagine the past five years without their support and friendship. I would like to acknowledge Dr. Sudipta Dutta and Dr. Sasmita Mohakud for their help from the first day of my life in JNC and wasted no time in making me feel comfortable when I newly joined the group. Then I met Dr. Arun K. Manna and Dr. Prakash Parida. They were good friends as much as they are were good seniors and guides to me. I appreciate the fact that they were always ready to interrupt their own work in order to answer questions whenever I had them. Work is never dull with the laughter and conversations between us. Alex and Ershaad who were very good friends of mine, helped me a lot and taught me how to install and use a variety of different softwares. I am also thankful to Dr. Ganga Periyasamy and Dr. Siamkhanthang Neihsial for collaboration and guidance, Dr. V. Meera and Dr. Elizabeth for caring me

as a brother. Sharma, with whom I always enjoy being around and discuss on variety of topics. Dibyajyoti for his strong company, not only in lab, also in time of shopping, going to restaurants, playing cricket or cooking in hostel in week-ends ... Bradraj and Pallavi for their help and friendship. Somananda and Swastika with whom I always enjoy being around, both during and after work hours. Shubhajit and post-doc Dr. Madhuri Mukhopadhyay who joined recently in our group, but took no time to get to know. Many many thanks to Arkamita for her extensive help at all the moments. I thank my former labmates Dr. Ayan Datta and Dr. Sairam S. Mallajosyula for scientific discussions related to my research work.

I thank Anusooya Ma'am and Sohan for their love, support and encouragement. They are like my family members and have created a homely environment for me in Bangalore.

I would like to convey my gratitude to all TSU faculties and students for their help and support. I thank Dasari and Sharmila for many fruitful scientific discussions since the beginning of my life in JNC. I would like to thank Anitha for various academic activities.

IACS and SNBNCBS (Kolkata) will always be very special for me for the Int. PhD program in Chemical Sciences (2007-2009), it really built my interest in research, and also, all my friends and course-instructors there. I am very much lucky to get the guidance of Prof. S. P. Bhattacharyya and Prof. D. S. Ray. I thank Amit, Biswajit, Dibakar, Kanchan-da, Ramprasad-da, Pushpita-di, Sabyasachi, Shekhar, Shubhasree-di, Sohini, Subhra, Susmita-di for their help and company.

I will always be indebted to all my friends and teachers from schools and

college, who had helped to build the first steps of my life.

I would to like to thank all my JNC and IISc friends Abhijit, Alok-da, Ananya, Anindita, Anirban, Arpan, Arup-da, Barun-da, Chandradhish, Debu-da, Dheeraj, Dipankar-da, Gautam-da, Jiarul, Jia-ul, Kanoo-da, Koushik, Moumita, Nivedita, Pallabi, Papri, Partha-da, Rajdeep Payal, Rajib, Ramana, Rana, Ritesh, Sabyasachi-da, Saikat, Sananda-di, Sandip-anna, Sandy-da, Sisir, Sohini, Somnath, Sougataa-di, Soumyabrata, Srinu, Subhajit, Sudipda, Sunita, Sudeshna, Suman-da, Supti-di, Sutapa-di, Syamantak, Tarak, Vasudevan, Wasim and others.

As Alex Haley had told once, "the family is link to our past, bridge to our future", finally and most importantly I would like to thank my parents, my sisters and my brother, with whom I share all my joys, whose love saw me through testing times, and who have stood by me no matter what. In my childhood days, I have spent a lot of time with my uncle and aunt. After having a hard day's play, I would be half asleep and they would be feeding me food so that I could go again and play the next day. I can't forget these moments. I am like their son and I am glad it has continued to be the same way.

Synopsis

For nanoscale architectures, one requires a controlled self-assembly of the device components. DNA presents itself as an ideal molecule that possesses superior properties of self-assembly. The natural Watson-Crick (WC) base pair can be replaced or modified artificially. Currently, an automated DNA synthesizer can make oligomers of the order of 100 nucleotides possessing pre-designed base sequences. By replacing WC base pair with metal-mediated base pair, one can selectively form a one-dimensional array of metal ions. Artificially modified base pair having fluorescence activity can be used as fluorescent probe. Single-stranded DNA, being flexible, can be of use for the formation of few atoms metal cluster. Properties of the few atoms metal clusters is also dependent on the nucleobase sequences used. Because of its self-assemble property, DNA can also form super coil, *i.e.*, quadruplex.

Majority of the works in this thesis have been carried out using density functional methods and molecular dynamics simulations. The thesis is divided into six chapters.

In the **first chapter**, a brief introduction to the DNA and modified DNA structures have been discussed. We have presented a comprehensive review of earlier theoretical and experimental studies. Overviews of different

computational methodologies used in the subsequent chapters, *viz.*, Density Functional Theory (DFT), Molecular Dynamics (MD) are discussed in detail in this chapter. We also have discussed briefly the Heisenberg models and how to solve it to obtain exchange coupling constants.

In the **second chapter**, we investigate the structure, energetics, bonding aspects and optical properties of two analogues of RNA nucleosides (thieno modified and size-expanded nucleosides). The results are compared against the findings obtained for the natural and both the modified nucleosides, as well as with the available experimental data. We find that the modified nucleosides form the hydrogen bonded (H-bonded) WC base pairing with similar H-bonding energy profile as found for the natural nucleosides. These modified nucleosides can also form WC base pairing with their natural complementary nucleosides. Further, we focus on the optical absorption properties of these modified nucleosides and their WC H-bonded base pairs in gas phase as well as in implicit water solvent. Our simulated results show that the low energy peaks in the absorption spectra mainly arise because of the π-π^* electronic transition for both the modified nucleosides.

In the **third chapter**, we look into the structures, energetics, electronic, and optical properties of a duplex DNA, containing metal-mediated base pairs. The duplex DNA consists of three imidazole (Im) units linked through metal (Im-M-Im, M = metal) and four flanking A:T base pairs (two on each side). We examined the role of artificial base pairing in the presence of two distinctive metal ions, diamagnetic Ag^{+} and magnetic Cu^{2+} ions, on the stability of duplex DNA. We find that the metal-mediated base pairs form stable duplex DNA by direct metal ion coordination to the Im bases.

We furthermore find that DNA, modified with Im-Ag^{+}-Im shows the low-energy optical absorption characteristic of π-π^{*} orbital transition of $A:T$ base pairs. On the other hand, the low-energy optical absorption peaks for DNA, modified with Im-Cu^{2+}-Im originate from spin-spin interactions, which is found to be weakly ferromagnetic.

In the **fourth chapter**, we study the structures, energetics, magnetic and optical properties for a variety of transition metal ($M = Mn$, Fe, Co, Ni and Cu) ions incorporated into modified-DNA (M-DNA) double helices. The DNA is modified with either hydroxyperidone (H) or bis-(salicylaldehyde)-ethylenediamine (S-en) metalated bases and we find the formation of extended M-O network leading to the ferromagnetic interactions for the case of H-DNA for all the metal ions. More ordered stacking arrangement was found for S-en-DNA. We calculate the exchange coupling constant (J) considering Heisenberg Hamiltonian for quantitative description of magnetic interactions within the DNA duplex. The ferromagnetic and anti-ferromagnetic interactions are obtained by varying the transition metal ions with different (+2 and +3) valencies as suggested by a number of experiments.

In the **fifth chapter**, we explore the formation of a few atoms metal (Silver and gold) clusters in presence of ssDNA in aqueous media at neutral pH. These few atoms metal clusters have high applicability in bio-systems as fluorescent sensors. We study the formation of these metal clusters using MD simulations and explain the origin of their optical properties using DFT.

In the **sixth (last) chapter**, we study the kinetics and folding pathway of Human Telomeric G-quadruplex. Although, G-triplexes have been proposed and demonstrated as intermediates in the folding pathway of G-quadruplexes,

there is still an ongoing debate on their folding pathways. In this work, we employ steered molecular dynamics simulation to investigate the folding kinetics of single human telomeric G-quadruplexes in presence of different alkali metal ions (Na^+ and K^+). Here, we find that the G-triplex is an in pathway intermediate during the folding of the G-quadruplex.

List of Publications

Publications Related to the Thesis Work

1. *"Computational Studies on Structural and Optical Properties of Single-stranded DNA encapsulated Silver/Gold cluster"*

   Pralok K. Samanta, Ganga Periyasamy, Arun K. Manna, and Swapan K. Pati,

   J. Mater. Chem. **22**, 6774 - 6781 (2012).

2. *"Thieno Analogues of RNA Nucleosides: A Detailed Theoretical Study"*

   Pralok K. Samanta, Arun K. Manna, and Swapan K. Pati,

   J. Phys. Chem. B **116**, 7618-7626 (2012).

3. *"Structural, Electronic and Optical Properties of Metallo Base-Pairs in Duplex DNA: A Theoretical Insight"*

   Pralok K. Samanta, Arun K. Manna, and Swapan K. Pati,

   Chem. Asian J. **7**, 2718-2728 (2012).

4. *"Structural, Electronic and Photophysical Properties of Analogous RNA Nucleosides: A Theoretical Study"*

   Pralok K. Samanta and Swapan K. Pati,

   New J. Chem. **37**, 3640-3646 (2013).

5. *"Structural and Magnetic Properties of a Variety of Transition Metal Incorporated DNA Double Helices"*
   Pralok K. Samanta and Swapan K. Pati,
   Chem. Eur. J. **20**, 1760-1764 (2014).

6. *"Understanding of Folding Pathway of Human Telomeric G-quadruplex using Steered Molecular Dynamics Simulation"*
   Pralok K. Samanta and Swapan K. Pati,
   (submitted, 2014)

Other Publications by the Author

7. *"Understanding the Binding Mechanism of Various Chiral SWCNTs and ssDNA: A Computational Study"*
   Siamkhanthang Neihsial, Ganga Periyasamy, **Pralok K. Samanta**, and Swapan K. Pati,
   J. Phys. Chem. B **116**, 14754-14759 (2012).

8. *"Molecular Architectonics of Stereochemically Constrained π-Complementary Functional Modules"*
   M. B. Avinash, **P. K. Samanta**, K. V. Sandeepa, S. K. Pati, and T. Govindaraju,
   Eur. J. Org. Chem., 5838-5847 (2013).

9. *"A Probe for Ratiometric Near-infrared Fluorescence and Colorimetric Hydrogen Sulfide Detection and Imaging in Live Cells"*
   D. Maity, R. Anand, **P. K. Samanta**, D. Karthigeyan, T. K. Kundu,

S. K. Pati, and T. Govindaraju,

RSC Adv., DOI: 10.1039/C4RA00401A (2014).

List of Figures

1.1 Chemical composition of nucleic acid components. (a) A purine nucleotide, deoxyadenosine 5′-monophosphate. (b) A pyrimidine nucleotide, thymidine 5′-monophosphate. 2

1.2 (a) Purine bases (Adenine, Guanine) and pyrimidine bases (Thymine, Cytosine, Uracil). (b) Watson-Crick base pairs, A:T and G:C. 3

1.3 Schematic diagram of single-stranded DNA (ssDNA) and duplex DNA.) 5

1.4 The three different conformations of duplex DNA (A-DNA, B-DNA and Z-DNA). 7

1.5 Schematic diagram of silver metal-mediated base pair (a) and Ag^{+} incorporated duplex DNA (b). 9

1.6 Schematic structure of G-tetrad (a) and in presence of metal ion (M^{+}) (b). Side (c) and top (d) view of G-quadruplex (PDB ID: 1KF1) in presence of K^{+}. 10

1.7 Comparison of a wave function in the Coulomb potential of the nucleus (blue) to the one in the pseudopotential (red). [1] The real and the pseudo wave function and potentials match above a certain cutoff radius r_c. 24

2.1 Optimized structures of natural RNA nucleosides, their thieno-analogues (thieno[3,4-d] pyrimidine nucleosides) and sized-expanded RNA nucleosides. Atom color code: blue (N), cyan (C), white (H), red (O), and yellow (S). 46

2.2 H-bonding between A:U, G:C (a), thA:thU, thG:thC (b) and ^{x}A:^{x}U, ^{x}G:^{x}C (c). Atom color code: blue (N), cyan (C), white (H), red (O), and yellow (S). 48

2.3 H-bonding potential profile for A:U, thA:thU, ^{x}A:^{x}U, G:C, thG:thC and ^{x}G:^{x}C. 51

2.4 Watson-Crick like base pairing between the thieno-nucleosides and size-expanded nucleosides with their natural complementary nucleoside. Atom color code: blue (N), cyan (C), white (H), red (O), and yellow (S). 52

2.5 Calculated absorption (solid line) and emission (dash line) spectra of modified A (black), modified U (red), modified G (green) and modified C (blue) in both water solvent (left) and gas phase (right). 55

2.6 Calculated highest occupied molecular orbital (HOMO) and lowest unoccupied molecular orbital (LUMO) of thieno-nucleosides and size-expanded nucleosides (in water). 57

3.1 Duplex structure of Im-Ag^+-Im modified DNA (Ag^+-DNA). . 67

3.2 Optimized structure of non-planar and planar Im-Ag^+-Im unit. Important bond distances (N-Ag) are written in unit of $\mathring{A}$. 67

3.3 Difference in charge density distribution ($\Delta\rho$) plot of (a) hydrogen passivated Ag^+-DNA, (b) Na^+ counter ion added Ag^+-DNA and (c) Na^+ counter ion and water added Ag^+-DNA. The red and blue colors indicate gain and loss in electron density, respectively. The above results show that electron transfer occurs from imidazole base to positively charged silver atoms. 74

3.4 Electronic DOS plots of (a) H-passivated Ag^+-DNA, (b) Na^+ counter ion added Ag^+-DNA and (c) Na^+ counter ions and 24 water molecules added Ag^+-DNA. 75

3.5 Frontier molecular orbital (FMO)diagram of (a) H-passivated to phosphate group, (b) Na^+ counter ions added and (c) Na^+ counter ions and 24 water molecules added to Ag^+-DNA. . . . 76

3.6 Optical absorption for H-passivated to phosphate group, Na^+ counter ions added and Na^+ counter ions and 24 water molecules added to Ag^+-DNA. 78

3.7 (a) Fragments considered for TD-DFT calculation and (b) molecular orbitals plot for the fragment (Im-Ag^+-Im)-($A:T$) and ($A:T$). 79

3.8 Optimized structure of (a) Im-Cu^{2+}-Im, (b) Im-$Cu(OH)_2$-Im and (c) Im-Cu^{2+}-Im modified DNA (Cu^{2+}-DNA). 81

3.9 Difference in (a) charge density distribution and (b) spin density diagrams. The plots are shown using VMD visual tool with isovalue 0.01. 86

3.10 (a) DOS plot of Cu^{2+}-DNA complex and (b) optical absorption spectra of Cu^{2+}-DNA. 88

3.11 Single occupied molecular orbital (SOMO) of Cu^{2+}-DNA. . . . 88

4.1 (a) hydroxyperidone MBP (H-MBP) and (b) salicylic aldehyde MBP in presence of ethylenediamine (S-en-MBP). 93

4.2 Displacement energy (E_d) for nH-DNA and nS-en-DNA with different metal (M) ions. 97

4.3 Optimized structure of 1H-DNA and 1S-en-DNA. 1H-DNA: (a) Mn^{2+}-DNA, (b) Co^{2+}-DNA, (c) Ni^{2+}-DNA, and (d) Cu^{2+}-DNA. 1S-en-DNA: (e) Mn^{3+}-DNA, (f) Fe^{3+}-DNA, (g) Co^{3+}-DNA, (h) Ni^{2+}-DNA and (i) Cu^{2+}-DNA. 98

4.4 Optimized structure of 2H-DNA and 2S-en-DNA. 2H-DNA: (a) Mn^{2+}-DNA, (b) Co^{2+}-DNA, (c) Ni^{2+}-DNA, and (d) Cu^{2+}-DNA. 2S-en-DNA: (e) Mn^{3+}-DNA, (f) Fe^{3+}-DNA, (g) Co^{3+}-DNA, (h) Ni^{2+}-DNA and (i) Cu^{2+}-DNA. 98

4.5 Optimized structure of 3H-DNA and 3S-en-DNA. 3H-DNA: (a) Mn^{2+}-DNA, (b) Co^{2+}-DNA, (c) Ni^{2+}-DNA, and (d) Cu^{2+}-DNA. 3S-en-DNA: (e) Mn^{3+}-DNA, (f) Fe^{3+}-DNA, (g) Co^{3+}-DNA, (h) Ni^{2+}-DNA and (i) Cu^{2+}-DNA. 100

4.6 Spin density diagram of 2H-DNA and 2S-en-DNA. 2H-DNA: (a) Mn^{2+}-DNA, (b) Co^{2+}-DNA, (c) Ni^{2+}-DNA, and (d) Cu^{2+}-DNA. 2S-en-DNA: (e) Mn^{3+}-DNA, (f) Fe^{3+}-DNA, (g) Co^{3+}-DNA, (h) Ni^{2+}-DNA and (i) Cu^{2+}-DNA. Color code: Red and blue define two different spin densities. 102

4.7 Optical conductivity diagram of nH-DNA and nS-en-DNA for n=1-3. 105

5.1 The initial configuration of Ag_{12}-$ssdC_{12}$ nanocomposites considered for MD simulations. 110

5.2 Schematic representations of two different thermodynamic cycles (Scheme-I and Scheme-II) used for free energy computations. 113

5.3 The configurations of Ag_{12}-$ssdA_{12}$ (a), Ag_{12}-$ssdT_{12}$ (b), Ag_{12}-$ssdG_{12}$ (c) and Ag_{12}-$ssdC_{12}$ (d) after 1.5 ns. For clarity, Ag_{12} clusters and nearby nucleobases are represented in sphere and tube formats, respectively. Nucleobases far from the Ag_{12} clusters are shown in wire frame. The water molecules and the counter ions (Na^+) are not shown. 114

5.4 The configurations of Au_{12}-$ssdA_{12}$ (a), Au_{12}-$ssdT_{12}$ (b), ug_{12}-$ssdG_{12}$ (c) and Au_{12}-$ssdC_{12}$ (d) after 1.5 ns. For clarity, Au_{12} clusters and nearby nucleobases are represented in sphere and tube formats, respectively. Nucleobases far from the Au_{12} clusters are shown in wire frame. The water molecules and the counter ions (Na^+) are not shown. 118

5.5 Computed absorption spectra of Ag_{12} and Au_{12} clusters. High intensity peaks are indicated '*' notation and their values are given in Table 5.3. The line spectra are broadened with Gaussian functions of width 0.05 eV. 121

5.6 Computed electronic density of states (DOS) for Ag_{12} and Au_{12} clusters using DFT. The energy is scaled with respect to Fermi energy (E_F). 123

5.7 Computed absorption spectra for different ssDNA (ssA_{12} (a), ssT_{12} (b), ssG_{12} (c) and ssC_{12} (d)). High intensity peaks are indicated by '*' notations and their values are given in Table 5.3. The line spectra are broadened with Gaussian functions of width 0.05 eV. 124

5.8 Electronic total density of states (DOS) and projected density of states (pDOS) for different ssDNA (ssA_{12} (a), ssT_{12} (b), ssG_{12} (c) and ssC_{12} (d) (black, red and green denote DOS, pDOS of nucleobase and backbone, respectively)). The energy (E) is scaled with respect to the Fermi energy (E_F). 125

5.9 Computed absorption spectra of Ag_{12}-ssA_{12} (a), Ag_{12}-ssT_{12} (b), Ag_{12}-ssG_{12} (c) and Ag_{12}-ssC_{12} (d). High intensity peaks are indicated by '*' notations and their values are given in Table 5.3. The line spectra are broadened with Gaussian functions of width 0.05 eV. 126

5.10 Electronic total density of states (DOS) and projected density of states (pDOS) of Ag_{12}-ssA_{12} (a), Ag_{12}-ssT_{12} (b), Ag_{12}-ssG_{12} (c) and Ag_{12}-ssC_{12} (d). The line spectra are broadened with Gaussian functions of width 0.05 eV. 127

5.11 Computed absorption spectra of Au_{12}-ssA_{12} (a), Au_{12}-ssT_{12} (b), Au_{12}-ssG_{12} (c) and Au_{12}-ssC_{12} (d). High intensity peaks are indicated by '*' notations and their values are given in Table 5.3. The line spectra are broadened with Gaussian functions of width 0.05 eV. 128

5.12 Electronic total density of states (DOS) and projected density of states (pDOS) of Au_{12}-ssA_{12} (a), Au_{12}-ssT_{12} (b), Au_{12}-ssG_{12} (c) and Au_{12}-ssC_{12} (d). The line spectra are broadened with Gaussian functions of width 0.05 eV. 129

5.13 Highest occupied molecular orbital (HOMO) and lowest unoccupied molecular orbital (LUMO) of Ag_{12}-$ssdC_{12}$. Orbital energy is scaled with respect to Fermi-energy (E_F). 130

6.1 NPT equilibration structure of Na^+ solution (seq1 = $d[AG_3(T_2AG_3)_3]$, PDB ID: 143D) (a) and K^+ solution (seq2 = $d[A_3G_3(T_2AG_3)_3A_3]$, PDB ID: 2HY9) (b). 138

6.2 Evolution of the structure of G-quadruplex during the stretching of seq1 in Na^+ solution (a) and seq2 in K^+ solution (b). . 139

6.3 Potential of mean force (PMF) as a function of end-to-end distance (nm) for seq1 in Na^+ solution (a) and seq2 in K^+ solution (b). 140

6.4 Number of H-bonds with time for seq1 in Na^+ solution (a) and seq2 in K^+ solution (b). 140

List of Tables

1.1 Average structural parameters of three different DNA conformations. 7

2.1 H-bonding stabilization energy (ΔE_{stab} in kcal mol^{-1}) and its Basis Set Superposition Error (BSSE) and zero-point-energy (ZPE) corrected values with different exchange and correlation energy functionals. 53

2.2 HOMO-LUMO gap (ΔE_{HL}) and lowest excitation energies and corresponding Oscillator Strengths (Os. Str.) of the thieno-nucleosides and size-expanded nucleosides. Experimentally the excitation energies are reported for thieno-nucleosides in water and for size-expanded nucleosides in methanol solvent. 56

2.3 Emission peaks of the thieno-nucleosides and size-expanded nucleosides. 58

2.4 Calculated Normal Mode Vibrational Frequencies (in cm^{-1}) for N-H Bond Stretching Directly Involved in Watson-Crick Base Pairing. 59

3.1 The binding energy ($E_b{}^c$) and displacement energy ($E_d{}^c$) per Ag and average electron transfer (ET) from imidazole to Ag^+. -*Ve* sign indicates electron transfer from Ag to the ligand. Basis set superposition corrected displacement energies are given within bracket. 73

3.2 Binding energy ($E_b/E_b{}^c$) and displacement energy ($E_d/E_d{}^c$) per metal atom, average electron transfer (ET) from ligand to each Cu^{2+}, and magnetic moment (μ_B). Basis set superposition corrected displacement energies are given within bracket. 87

4.1 Spin Stabilization Energy (ΔE_s) and Exchange Coupling Constant (J). 95

4.2 Metal-metal distances (d1 and d2 in $\mathring{A}$) in nH-DNA and nSen-DNA (n=2,3). 100

4.3 Exchange Coupling Constant (J) of different M-DNA Systems. 103

5.1 Number of nucleobases (N) involving in two types of interactions, computed interaction energy (E_{int} in kJ mol^{-1}) at 1.5 ns and binding free energy (ΔF_{bind} in kJ mol^{-1}, both scheme-I and scheme-II in Fig. 5.2) values for the simulated Ag_{12}-ssDNAs nanocomposites. N' and N'' are the number of nucleobases, interacting *via* π-cloud and specific atoms (Nitrogen and/or oxygen). 116

5.2 Number of nucleobases (N) involving in two types of interactions, computed interaction energy (E_{int} in kJ mol^{-1}) at 1.5 ns and binding free energy (ΔF_{bind} in kJ mol^{-1}, both scheme-I and scheme-II in Fig. 5.2) values for the simulated Au_{12}-ssDNAs nanocomposites. N' and N'' are the number of nucleobases, interacting *via* π-cloud and specific atoms (Nitrogen and/or oxygen). 119

5.3 Excitation energies (eV) corresponding to intense peaks of the Ag_{12}, Au_{12}, ssDNAs, Ag_{12}-ssDNAs and Au_{12}-ssDNAs. 122

Contents

Acknowledgements **v**

Synopsis **ix**

1 Introduction **1**

1.1 Components of nucleic acid structure 2

1.2 Single stranded DNA 4

1.3 Duplex DNA 4

1.4 Modified DNA and RNA 8

1.5 Nucleic Acid Quadruplex 11

1.6 Theoretical Models and Methods 12

1.6.1 Quantum Mechanical Calculations 12

1.6.2 Heisenberg Model 16

1.6.3 Density Functional Theory 17

1.6.4 Classical Molecular Dynamics 26

1.7 Softwares and Hardwares used 39

1.8 Outline of Thesis 40

2 Structural, Electronic and Photophysical Properties of Analogous RNA Nucleosides 43

2.1 Introduction 43

2.2 Computational Methods 46

2.3 Results and Discussion 47

2.3.1 Structural and energetics analysis of the WC base pairs 47

2.3.2 Optical Absorption and Emission 54

2.4 Conclusions 59

3 Structural, Electronic and Optical Properties of Metallo Base-Pairs in Duplex DNA 61

3.1 Introduction 61

3.2 Computational Methods 65

3.3 Results and Discussion 66

3.3.1 Structure and Stability 66

3.3.2 Electronic Structure 74

3.3.3 Optical Absorption 77

3.3.4 A proposed model system: Im-$Cu(OH)_2$-Im modified duplex DNA (Cu^{2+}-DNA) 80

3.4 Conclusions 89

4 Magnetic Properties of a Variety of Transition Metal Incorporated DNA Double Helices 91

4.1 Introduction 91

4.2 Computational Methods 93

4.3 Results and Discussion 96

4.4 Conclusions 105

5 Structural and Optical Properties of Single-stranded DNA encapsulated Silver/Gold clusters 107

5.1 Introduction 107

5.2 Computational Methods 110

5.3 Results and Discussion 114

5.3.1 Structural analysis of Ag_{12}/Au_{12} and ssDNA sequences in aqueous media 114

5.3.2 Structural and energetic analysis of Ag_{12}-ssDNA nanocomposites 115

5.3.3 Structural and energetic analysis of Au_{12}-ssDNA 117

5.3.4 Absorption Spectra 120

5.4 Conclusions 129

6 Kinetic and Folding Pathway of Human Telomeric G-quadruplex 133

6.1 Introduction 133

6.2 Computational Methods 136

6.3 Results and Discussion 137

6.3.1 Equilibrium Simulations 137

6.3.2 Force Induced Conformational Changes 138

6.3.3 Free Energy Profile 139

6.3.4 Hydrogen Bonding Profile 141

6.4 Conclusions 141

Bibliography 143

Chapter 1

Introduction

Nucleic acids, the blue-print of life, have been known to be the central molecules in transmission, expression, and conservation of genetic information in all the living organisms (animals, plants, fungi, bacteria etc.). Deoxyribonucleic acids (DNA), ribonucleic acids (RNA) and proteins are essentials for all known forms of life. Nucleic acids were discovered by Swiss scientist Friedrich Miescher in 1869. [2] Later, he realized that the nucleic acid (DNA) could be involved in heredity. Experimental studies on nucleic acids constitute a major part of modern biological and medical researches. [3] It is very much important for genome and forensic science too. [4] It has a huge variety of applications in modern biotechnology and pharmaceutical industries. Currently, an automated DNA synthesizer can routinely make oligomers in the order of 100 nucleotides possessing pre-designed base sequences. [5] Nucleic acid analogues are compounds which are structurally similar to naturally occurring RNA and DNA, used in medicine, molecular biology and in advanced nanotechnology research. [6] Nucleic acid exists in many possible

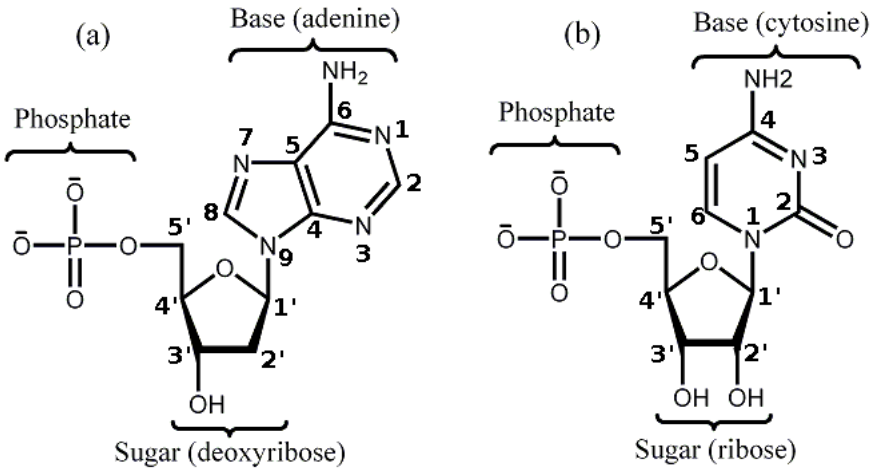

Figure 1.1: Chemical composition of nucleic acid components. (a) A purine nucleotide, deoxyadenosine 5′-monophosphate. (b) A pyrimidine nucleotide, thymidine 5′-monophosphate.

conformations. It can be single-stranded, double-stranded (duplex), triple-stranded (triplex), quadruple-stranded (quadruplex) and other telomere-like structures. [7, 8]

1.1 Components of nucleic acid structure

DNAs and RNAs are built from a basic unit called nucleotide. Each nucleotide unit consists of three chemically and structurally distinct components: a nitrogenous base, a pentose sugar and a phosphate group. There are four nitrogenous bases, Adenine (A), Thymine (T), Guanine (G) and Cytosine (C) for naturally occurring DNA. In case of naturally occurring RNA, Uracil (U) replaces Thymine (T). Also, DNA and RNA differ in their sugar part. In case of DNA the sugar is 2′-deoxyribose whereas, in case of RNA the sugar is ribose (see Fig. 1.1). The 2′-deoxyribose is derived from ribose by

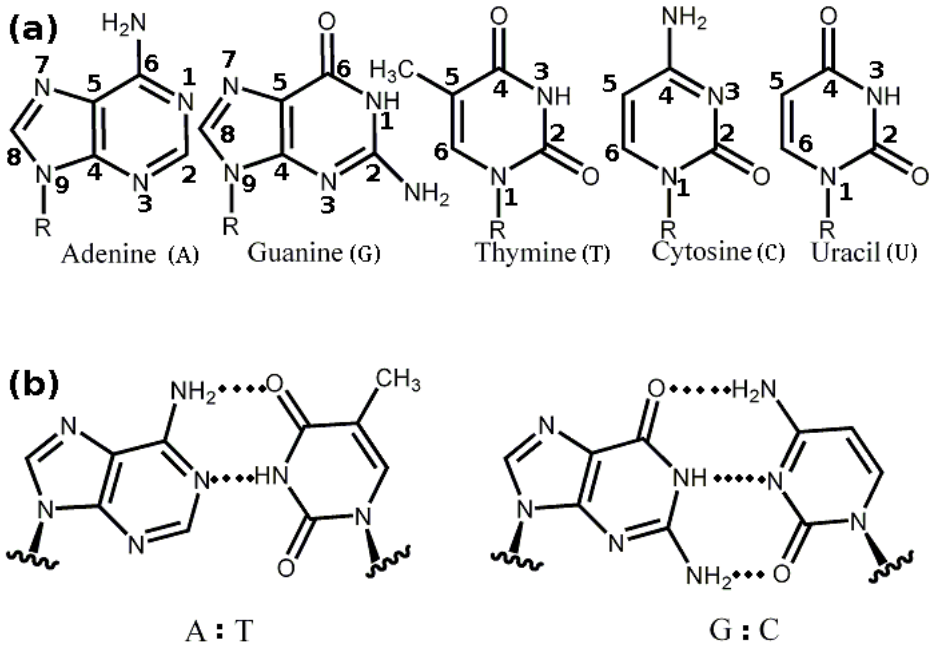

Figure 1.2: (a) Purine bases (Adenine, Guanine) and pyrimidine bases (Thymine, Cytosine, Uracil). (b) Watson-Crick base pairs, A:T and G:C.

the replacement of hydroxyl group at the 2′ position with hydrogen, leading to the net loss of an oxygen atom. DNA and RNA are formed when a nucleobase forms a glycosidic bond with the 1′ anomeric carbon of deoxyribose (for DNA) or ribose (for RNA), called a nucleoside, and then the nucleoside gets connected with a phosphate group attached at the 5′ carbon forming nucleotide (see Fig. 1.1). Thus a poly nucleotide has a 3′ end and a 5′ end. Nucleotide is the basic unit of nucleic acid.

1.2 Single stranded DNA

Most RNAs are linear and single-stranded polynucleotides whereas, most DNAs are usually double-stranded polynucleotides in biological systems. Single-stranded DNA (ssDNA) is formed when the strands in a duplex DNA separate and exist in solution as two entirely independent polynucleotides (see Fig. 1.3). Also the ssDNA can be synthesized with a predefined sequence of nucleobases. In a cell, ssDNA is produced during all aspects of duplex DNA metabolism: replication, recombination and repairing. Single-stranded DNA-binding protein binds to single-stranded regions of DNA to prevent premature annealing, protecting the ssDNA and to remove secondary structure from the DNA to allow other enzymes to function on the ssDNA. These ssDNA molecules are more flexible than double-stranded DNA (dsDNA). These ssDNAs have very important applications in advanced technology. In fact, these can be used to purify different chiral carbon nanotubes [9,10] and to form few atoms metal clusters. [11]

1.3 Duplex DNA

Within eukaryotic cells, DNA stay in the form of chromosomes. DNA consists of two anti-parallel polynucleotides, one backbone being $3'$ and the other as $5'$. Two strands are connected by nucleobase pairs. Double helical structure of DNA was first discovered by Watson and Crick [12], based on the X-ray diffraction patterns reported by Franklin *et al.* [13] and Wilkins *et al.* [14], along with the chemical evidence of base complementarity proposed by

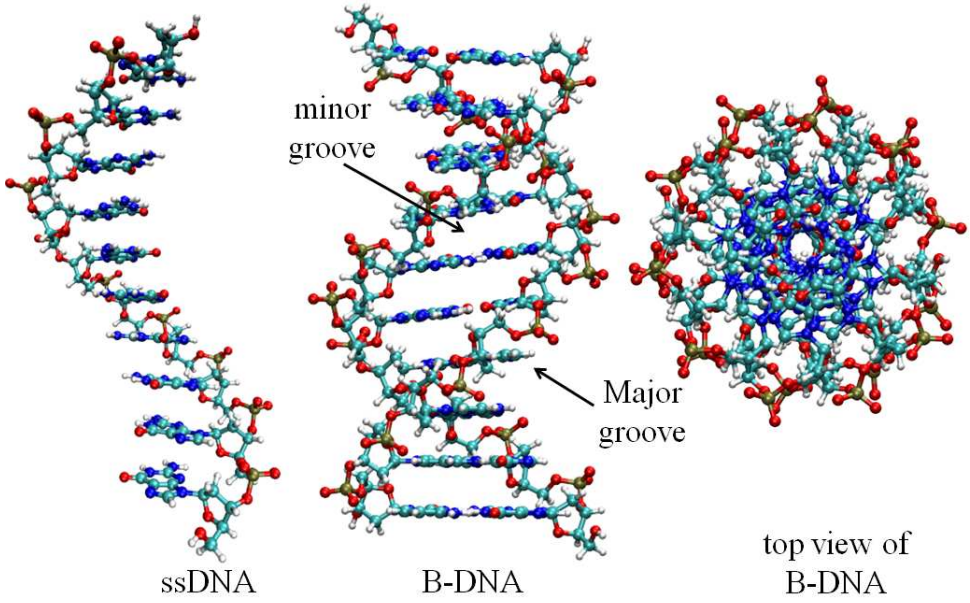

Figure 1.3: Schematic diagram of single-stranded DNA (ssDNA) and duplex DNA.)

Chargaff [15]. Nucleobase 'A' selectively forms hydrogen bonds (H-bonds) with the nucleobase 'T' *via* two H-bonds and the nucleobase 'G' selectively forms H-bonds with the nucleobase 'C' *via* three H-bonds (see Fig. 1.2). [12] These types of nucleobase pairs are known as Watson-Crick base pairs. The unique feature of the Watson-Crick base pairing is that the distances between the C1′ atoms of sugars on opposite strands are essentially the same. [16]

Any sequence of artificial base pairs with minimal structural distortion can be incorporated into a DNA double helix. There are also several H-bonded base pairs, determined by X-ray crystallographic studies in non-canonical DNA structures, which have been investigated in details. [17–19]

Under physiological condition, DNA forms a right-handed double helical structure, where two DNA strands (chains) wind around an axis. The hydrophilic backbone of alternating deoxyribose and phosphate groups are

on the outside of the double helix, while nucleobases (A, T, G and C) are stacked inside the double helix. Each nucleobase of one strand is paired in the same plane with it's Watson-Crick complementary nucleobase on the other strand. Thus, the two DNA strands that form the double helical structure have a complementary nucleobase sequence. The Watson-Crick base pairs in a DNA double helix structure align parallel to each other, with the planes of the base pairs being perpendicular to the helical axis. Under physiological conditions, DNA adopts the B-DNA conformation. The B-conformation of DNA is characterized by an average helical twist of about 36° and thus the completion of one full helix turn is in every 10 base pairs. The helix radius is found to be approximately 10 $\mathring{A}$ and the pitch is at around 3.4 $\mathring{A}$. [20]

The strand backbones (sugars and phosphates) are closer together on one side of a DNA double helix compared to the other side. The major groove occurs where the backbones are far apart and the minor groove occurs on the other side of the double helix. The grooves arise because of the antiparallel arrangement of the two backbone strands. Both the grooves run continuously along the entire length of the DNA double helix. The major groove is about 22 $\mathring{A}$ wide and the minor groove is $\sim$12 $\mathring{A}$ wide. [20] It is clear from their width that the nucleobases are more accessible in the major groove.

Double-stranded DNA can adopt many different conformations. [21] However, only the A-DNA, B-DNA, and Z-DNA conformations are found in organisms (see Fig. 1.4). The A-DNA form is a wider right-handed helical with a shallow and wide minor groove and a narrower and deeper major groove. It occurs under non-physiological conditions in dehydrated samples of DNA. On the other hand, Z-DNA is left-handed and often compared against B-DNA

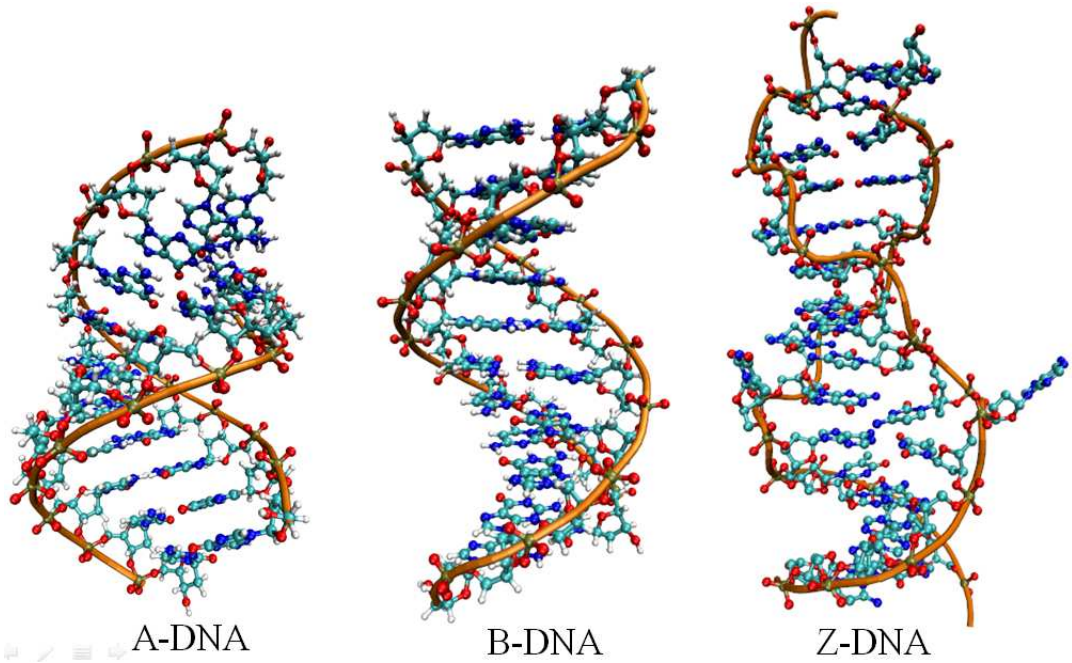

Figure 1.4: The three different conformations of duplex DNA (A-DNA, B-DNA and Z-DNA).

Table 1.1: Average structural parameters of three different DNA conformations.

Geometrical Parameters	A-DNA	B-DNA	Z-DNA
Helix type	right-handed	right-handed	left-handed
Repeating unit	1 bp	1 bp	2 bp
Rotation per bp	32.7^o	35.9^o	30^o
No. of bp per turn	11	10.5	12
Rise per bp along axis	2.3 $\mathring{A}$	3.32 $\mathring{A}$	3.8 $\mathring{A}$
Diameter	23 $\mathring{A}$	20 $\mathring{A}$	18 $\mathring{A}$

in order to illustrate the major differences. The major and minor grooves of Z-DNA show little difference in width. Also, the formation of Z-DNA structure is generally unfavorable. [22] The structural characteristics of the three DNA conformations are tabulated in Table 1.1. [23–25]

1.4 Modified DNA and RNA

A wide variety of modifications can be incorporated into an oligonucleotide (DNA, RNA) during the time of synthesis. [26] This is done using a modified solid support (CPG) for 3′-modifications or a specialized phosphoramidite reagent for internal and 5′-modifications. [27] Post-synthetic chemical modifications also can be done to an oligonucleotide. But, this results in lower yields than modifications introduced during synthesis. There are various applications of these modified oligonucleotide, starting from bio-medical applications to advanced nano-biotechnology.

Natural nucleic acid residues do not show fluorescence emission in UV-visible region. Whereas, there are some analogues (artificially synthesized) which show fluorescence emission in the UV-visible region. [28] The key criterion for the designing of fluorescence active nucleic acid residue is to minimize structural and functional perturbations of the oligonucleotides (DNA, RNA). For example, Shin *et al.* [29] have reported thieno-modified analogue of RNA nucleosides and these analogues RNA nucleotides show fluorescence emission in UV-visible region. Fusion of additional aromatic rings onto the pyrimidine and purine extend the conjugation of natural nucleobases. Though, most of these size-expanded nucleobases retain their WC H-bonding face

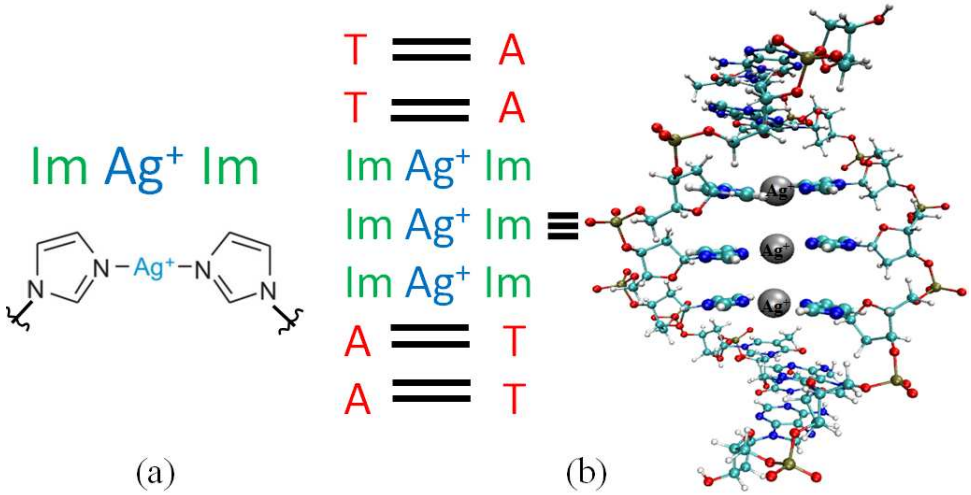

Figure 1.5: Schematic diagram of silver metal-mediated base pair (a) and Ag^+ incorporated duplex DNA (b).

but their large surface area could structurally perturb the resulting oligonucleotides. The extended conjugation typically results red-shifted absorption bands compared with upon incorporation into oligonucleotides and can show fluorescence emission. The fluorescent nucleosides have found numerous applications and remain very useful due to their high quantum efficiency. Hernandez *et al.* [30] have reported fluorescent size-extended modified RNA nucleosides by fusing additional benzene rings onto the pyrimidine and purine nuclei.

Also the Watson-Crick hydrogen bonding between natural DNA base pairs can be replaced by metal-coordination bonding. This gives a new class of modified DNA. This approach leads to completely different and alternative base pairs consisting of both inorganic and organic species. These type of modified base pairs are called metal-mediated base pairs (Fig. 1.5). The metal-mediated base pairs can stabilize duplex DNA duplex and selective

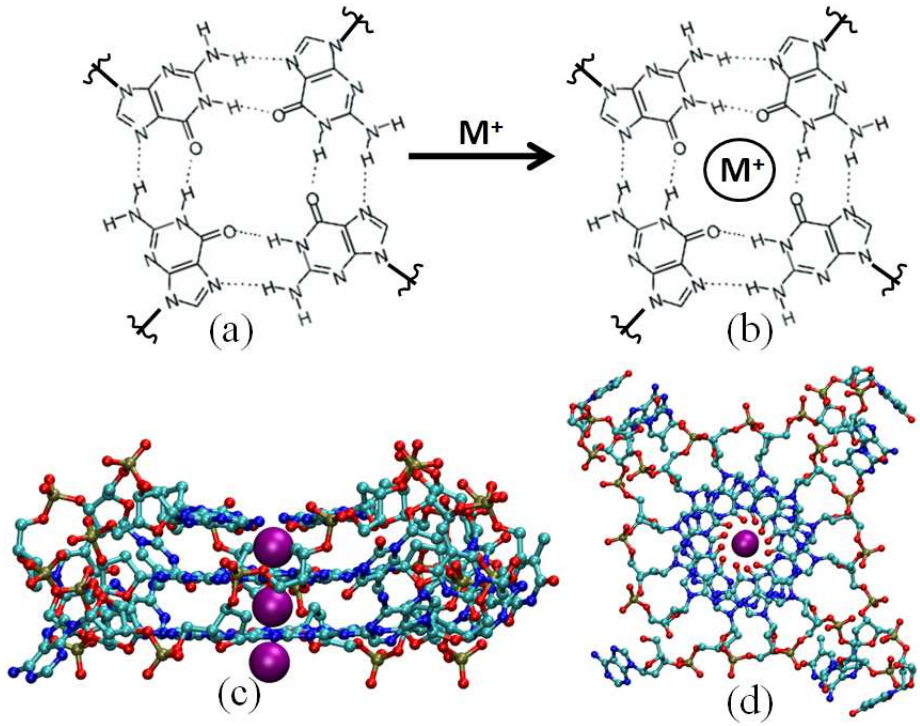

Figure 1.6: Schematic structure of G-tetrad (a) and in presence of metal ion (M^+) (b). Side (c) and top (d) view of G-quadruplex (PDB ID: 1KF1) in presence of K^+.

metal ions can be aligned inside the DNA skeleton by varying the artificial nucleobases (ligand) of different functionalities. [5, 31, 32] From melting-temperature studies, it was found that the metal-DNA duplexes can be more stable in comparison to their corresponding natural DNA duplexes. [31] Site-specific alignment of magnetic and non-magnetic ions at different positions in the same DNA scaffold can be done which could have high potential application as low-dimensional magnetic arrays. [33]

1.5 Nucleic Acid Quadruplex

Apart from the ssDNA and dsDNA structures, which have been discussed above, a number of secondary structures of DNA are known to be present in organisms, which regulate various catalytic biological processes. These nucleic acid structures include triplexes, hairpin loops, internal loops, junctions, i-motif and G-quadruplexes and many other structures. [34–36] Among these, G-quadruplex structures are important because of their potential functions not only for *in vivo*, but also for *in vitro* applications. In G-quadruplex, four guanines are held in a plane by Hoogsteen hydrogen-bonds (H-bonds) to each other that causes the formation of a cyclic structure with a central cavity (see Fig. 1.6). Each guanine comes from one strand and hence, the quadruplex formation leads to a four stranded structure. Also the guanine planes are stabilized by non-polar interaction between the stacked tetrads and the electrostatic interaction involving monovalent cations (*e.g.*, K^+, Na^+) sandwiched between two quartets which reduce the repulsion between the aromatic oxygen atoms in neighboring guanines. [7, 37–39] There are different types of quadruplex polymorphisms. [40–42] These include different strand orientations (parallel and antiparallel), molecularity (tetramolecular, bimolecular and unimolecular), glycosidic conformations (syn and anti). Also the polymorphism depends on the loops topologies (lateral, diagonal, V-shaped and double chain reversal loops). The folding topology of a quadruplex depends on the sequence of the oligonucleotide and the presence of alkali metal ions (K^+, Na^+ etc.). It can regulate gene expression and has an important role in several aspects of metabolism, such as transcription termination, splicing and

translations. [43–47] It has recently received great interest because of possible targets for cancer therapy. [48] In addition, synthetic G-quadruplexes are used as drugs for treating cancer [49–52], prevention of thrombosis [53] and inhibition of HIV replication. [54] Also, the drugs that bind specifically to quadruplex DNAs can be used for the treatment of a variety of pathological conditions including cancer. [55] In time of cell division, the length of telomere decreases in normal somatic cells. In contrast to normal cells, most of the human tumor cells have functional telomerase which elongates the telomere. [34] G-quadruplex DNA inhibits telomerase activity and hence controls the rate of cell division.

1.6 Theoretical Models and Methods

In this section different theoretical models and methods, used in this thesis are described briefly. We use either electronic structure methods or classical molecular dynamics (MD) techniques depending on the properties of interest for studying nucleic acid or modified nucleic acid structures.

1.6.1 Quantum Mechanical Calculations

Quantum mechanics provides a mathematical description of any system to describe their properties in accurate way. There are many phenomenon, *viz.*, wave-particle duality (electron can be considered as a wave as well as a particle), uncertainty (that two conjugate quantities can not be determined with 100% accuracy) etc. which have put all the microscopically accurate description of seemingly impossible phenomena into reality today. It is possible to

determine the ground state electronic structure and various properties associated with it for both the molecular as well as extended class of systems using quantum mechanical calculations. The molecular wave functions obtained from quantum mechanical calculations can be used to study a range of physicochemical properties, *viz.*, dipole and higher multipole moments, polarizability, vibrational spectra, absorption and emission spectra, etc. with a great accuracy and well corroborative with the experimental findings.

In quantum mechanics, particles are described by wave functions ($\Psi_i(\mathbf{r}$, t), i=1, 2, ..., N), where, $\Psi_i^*\Psi_i$ gives the probability density of finding the i-th particle at position $\mathbf{r}$ at time t and N is the total number of particles. The foundation of the theory of electronic structure of matter is the non-relativistic Schrödinger equation for the many-electron wave function. If $\hat{H}$ is the total energy operator (Hamiltonian) of a system of total wave function Ψ_{tot}, then the time-independent Schrödinger equation is:

$$\hat{H}\Psi_{tot} = E\Psi_{tot} \tag{1.1}$$

In practice, the wave functions of an interacting many electron systems is not known a priori. To solve the Schrödinger equation, one starts with a initial guess wave function, which is usually considered to be as the linear combination of the basis functions($\{\chi_i\}$). Then the wave functions are solved self-consistently with each iterations.

$$\Psi_i = \sum_{j=1}^{N} c_{ij}\chi_j \tag{1.2}$$

For a system of N electrons (fermions) the total wavefunction (Ψ_{tot}) must follow anti-symmetry requirements and consequently the Pauli exclusion principle. Therefore, Ψ_{tot} can be described in terms of Slater determinants. If $\{\Psi_i(\mathbf{r})\}$ are the one electron spin-orbitals, for an N-electron system, a Slater determinant is defined as,

$$\Psi_{tot}(\mathbf{r}_1, \mathbf{r}_2, ..., \mathbf{r}_N) = \frac{1}{\sqrt{N!}} \begin{vmatrix} \Psi_1(\mathbf{r}_1) & \Psi_2(\mathbf{r}_1) & ... & \Psi_N(\mathbf{r}_1) \\ \vdots & \vdots & \ddots & \vdots \\ \Psi_1(\mathbf{r}_N) & \Psi_2(\mathbf{r}_N) & ... & \Psi_N(\mathbf{r}_N) \end{vmatrix} \tag{1.3}$$

Every system consists of a number of nuclei and electrons. For a system with N_e number of electrons and N_n number of nuclei, the total Hamiltonian ($\hat{H}$) can be written as:

$$\begin{aligned} \hat{H} = &- \sum_{i=1}^{N_e} \frac{\hbar^2}{2m} \nabla_i^2 - \sum_{I=1}^{N_n} \frac{\hbar^2}{2M_I} \nabla_I^2 - \sum_{i=1}^{N_e} \sum_{I=1}^{N_n} \frac{Z_I e^2}{|\mathbf{r}_i - \mathbf{R}_I|} \\ &+ \sum_{i=1}^{N_e-1} \sum_{j>i}^{N_e} \frac{e^2}{|\mathbf{r}_i - \mathbf{r}_j|} + \sum_{I=1}^{N_n-1} \sum_{J>I}^{N_n} \frac{Z_I Z_J e^2}{|\mathbf{R}_I - \mathbf{R}_J|} \end{aligned} \tag{1.4}$$

where, m is the mass of an electron and M_I is the mass of I-th nucleus. The Laplacian operators, ∇_i^2 and ∇_I^2 represent the second order differentiation with respect to the coordinates of the i-th electron and the I-th nucleus, respectively. e is the charge of an electron and Z_I is the atomic number of the I-th nucleus. $\mathbf{r}_i$ and $\mathbf{R}_I$ represent the spatial coordinates of i-th electron and I-th nucleus, respectively. The first two terms in the equation 1.4 are the kinetic energy operators of electrons and nuclei, respectively. The third

term represents the Coulomb attraction between electrons and nuclei. The fourth and fifth terms represent the Coulomb repulsion between the electrons and between the nuclei, respectively.

Born-Oppenheimer Approximation

In Born-Oppenheimer approximation, the wavefunction of a system can be divided into its electronic and nuclear components. This is because of the heavy mass of nuclei and hence the motion of massive nucleus can be neglected. As a consequence, the nuclear skeleton can be considered to be frozen with respect to the electronic motion. Therefore, the kinetic energy for the nuclei can be neglected and the Coulomb repulsion among the nuclei can be considered as a constant. This approximation is called *Born-Oppenheimer approximation* which considers the movement of electrons in the static nuclei potential. With this approximation, the wave function of the system can be written as,

$$\Psi_{tot}(\mathbf{r}_i, \mathbf{R}_I) = \chi(\mathbf{r}_i, \mathbf{R}_I)\psi(\mathbf{R}_I) \tag{1.5}$$

where, $\chi(\mathbf{r}_i, \mathbf{R}_I)$ is the electronic part of the wave function, $\Psi_{tot}(\mathbf{r}_i, \mathbf{R}_I)$ and $\psi(\mathbf{R}_I)$ is the nuclear part of that. Then the electronic Schrödinger equation turns out to be:

$$\left[-\frac{\hbar^2}{2m}\sum_{i=1}^{N_e}\nabla_i^2 - \sum_{i=1}^{N_e}\sum_{I=1}^{N_n}\frac{Z_I e^2}{|\mathbf{r}_i - \mathbf{R}_I|} + \sum_{i=1}^{N_e-1}\sum_{j>i}^{N_e}\frac{e^2}{|\mathbf{r}_i - \mathbf{r}_j|}\right]\chi(\mathbf{r}_i, \mathbf{R}_I) = E_e(\mathbf{R}_I)\chi(\mathbf{r}_i, \mathbf{R}_I) \tag{1.6}$$

while, the Schrödinger equation for the nuclear part become is the remaining

terms:

$$\left[-\sum_{I=1}^{N_n}\frac{\hbar^2}{2M_I}\nabla_I^2+\sum_{I=1}^{N_n-1}\sum_{J>I}^{N_n}\frac{Z_I Z_J e^2}{|\mathbf{R}_I-\mathbf{R}_J|}+E_e(\mathbf{R}_I)\right]\psi(\mathbf{R}_I)=E\psi(\mathbf{R}_I) \quad (1.7)$$

However, in case of nuclear vibrations, the consideration of Born-Oppenheimer approximation breaks down because of unavoidable nuclear motion. Therefore, calculation of vibrational and rotational spectroscopy need explicit consideration of nuclear motion, or to an approximation using equation 1.7.

1.6.2 Heisenberg Model

The exchange interaction, a quantum mechanical effect, is interaction between identical particles. The exchange interaction between magnetic sites in terms of their spin moments, $\vec{S_i}$ and $\vec{S_j}$ for i-th and j-th sites, respectively, can be described using Heisenberg Exchange Hamiltonian.

$$H=-\sum_{i,j(j>i)}J_{ij}\vec{S_i}\cdot\vec{S_j} \quad (1.8)$$

where, the sum is over the spin vectors which are interacting and J_{ij} is the exchange coupling between the i-th and j-th sites. Sign of J describe the type of interaction (ferromagnetic or antiferromagnetic). For ferromagnetic interaction the value of J is positive and for antiferromagnetic interaction, the value of J is negative. For a linear chain of N equivalent sites with nearest neighbor interaction, Heisenberg Exchange Hamiltonian can be written as,

$$H=-J\sum_{i=1}^{N-1}\sum_{j>i}^{N}\vec{S_i}\cdot\vec{S_j} \quad (1.9)$$

However, note that, Heisenberg Exchange Hamiltonian considers magnetic centers which are strictly localized in orbitals (*e.g.*, 3d orbitals).

1.6.3 Density Functional Theory

Density functional theory (DFT) is a quantum mechanical modeling method used in physics and chemistry for treating an inhomogeneous system of interacting electrons. It has been proved to be highly efficient and successful method to investigate the electronic structure of many-body systems, in particular atoms, molecules and the condensed phases showing satisfactory agreement with the experimental observations.

Within DFT, the Hamiltonian ($\hat{H}$) of an N electron system in the presence of an external field, $V_{ext}(\mathbf{r})$, including the field induced by the nuclei is given by,

$$\hat{H} = \hat{T} + \hat{U} + \hat{V}_{ext} = -\frac{\hbar^2}{2m}\sum_{i=1}^{N}{\nabla_i}^2 + \sum_{i=1}^{N-1}\sum_{j>i}^{N}\frac{e^2}{|\mathbf{r}_i - \mathbf{r}_j|} + \hat{V}_{ext}(\mathbf{r}) \quad (1.10)$$

DFT is based on the fact that the ground state electronic wave function, $\Psi_0(\mathbf{r}_1, \mathbf{r}_2, ..., \mathbf{r}_N)$, can be entirely described only by its electron density $\rho_0(\mathbf{r})$, as stated by the Hohenberg-Kohn theorem [56–58]. It is based on a variational principle stating that the ground state electronic density minimizes the energy functional.

- The external potential, V_{ext} is uniquely determined by the corresponding ground state electronic density. It can be stated in other way as

well: the external potential, V_{ext}, determines exactly the electron density $\rho(\mathbf{r})$. Furthermore, the ground state expectation value of any observable is a unique functional of the ground state electron density.

- The variational principle is also valid for the electron density. The total energy is minimal for the ground state density, $\rho_0(\mathbf{r})$, of the system.

$$\rho(\mathbf{r}) = N \int d\mathbf{r}_2 d\mathbf{r}_3 d\mathbf{r}_4 ... d\mathbf{r}_N \Psi(\mathbf{r}, \mathbf{r}_2, ..., \mathbf{r}_N)^* \Psi(\mathbf{r}, \mathbf{r}_2, ..., \mathbf{r}_N) \tag{1.11}$$

In reverse manner, for a given ground state density, $\rho_0(\mathbf{r})$, it is possible to calculate the ground state wavefunction, $\Psi_0(\mathbf{r}_1, \mathbf{r}_2, ..., \mathbf{r}_N)$, *i.e.*, $\Psi_0(\mathbf{r}_1, \mathbf{r}_2, ..., \mathbf{r}_N)$ is an unique functional of $\rho_0(\mathbf{r})$. [56]

$$\Psi_0(\mathbf{r}) = \Psi_0[\rho_0(\mathbf{r})] \tag{1.12}$$

Now, the expectation value of an observable ($\hat{A}$) in it's ground state, is also the function of ρ_0.

$$A[\rho_0] = \langle \Psi_0[\rho_0] | \hat{A} | \Psi_0[\rho_0] \rangle \tag{1.13}$$

And hence, the ground state energy(E_0) is also a functional of ρ_0.

$$E_0 = E[\rho_0] = \langle \Psi_0[\rho_0] | \hat{T} + \hat{U} + \hat{V}_{ext} | \Psi_0[\rho_0] \rangle \tag{1.14}$$

Here the external potential, $\langle\Psi_0[\rho_0]|\hat{V}_{ext}|\Psi_0[\rho_0]\rangle$, can be written as,

$$V_{ext} = V_{ext}[\rho_0] = \int \hat{V}_{ext}(\mathbf{r})\rho_0(\mathbf{r})d\mathbf{r} \tag{1.15}$$

More generally, the expectation values of $\hat{T}$, $\hat{U}$ and $\hat{V}_{ext}$ can be written explicitly in terms of density $\rho(\mathbf{r})$.

$$T[\rho] = \langle\Psi[\rho]|\hat{T}|\Psi[\rho]\rangle \tag{1.16}$$

$$U[\rho] = \langle\Psi[\rho]|\hat{U}|\Psi[\rho]\rangle \tag{1.17}$$

$$V_{ext}[\rho] = \langle\Psi[\rho]|\hat{V}_{ext}|\Psi[\rho]\rangle \tag{1.18}$$

$T[\rho]$ and $U[\rho]$ are called universal functionals. $V[\rho]_{ext}$ depends on the systems under study and hence, it is a non-universal functional of electron density, $\rho_0(\mathbf{r})$. Then the ground state density can be calculated after the minimization of the energy function, $E[\rho]$, with respect to $\rho(\mathbf{r})$. Thus, all other ground-state observable can be calculated from $\rho_0(\mathbf{r})$. Lagrangian method of undetermined multipliers can be used to minimize the energy functional $E[\rho]$. Energy functional can be considered such that it doesn't have any explicit electron-electron interaction energy term,

$$E_s[\rho] = \langle\Psi_s[\rho]|\hat{T} + \hat{V}_s|\Psi_s[\rho]\rangle \tag{1.19}$$

$\hat{V}_s$ is an effective potential in which particles are moving so that $\rho_s(\mathbf{r}) = \rho(\mathbf{r})$. Thus, the Kohn-Sham equations of this auxiliary non-interacting system is

defined as,

$$\left[-\frac{\hbar^2}{2m}\nabla_i^2 + \hat{V}_s\right]\phi_i(\mathbf{r}) = \epsilon_i\phi_i(\mathbf{r}) \tag{1.20}$$

$\{\phi_i(\mathbf{r})\}$ are the Kohn-Sham orbitals and reproduce the density of the original many-body system.

$$\rho(\mathbf{r}) = \rho_s(\mathbf{r}) = \sum_{i=1}^{N} |\phi_i(\mathbf{r})|^2 \tag{1.21}$$

The effective single-particle potential (V_s) can be written in detail:

$$V_s(\mathbf{r}) = V_{ext}(\mathbf{r}) + \int \frac{\rho_s(\mathbf{r}')}{|\mathbf{r}-\mathbf{r}'|}d\mathbf{r}' + V_{xc}(\rho_s(\mathbf{r})) \tag{1.22}$$

The total energy of the system can be written as:

$$E[\rho(\mathbf{r})] = T_s[\rho(\mathbf{r})] + \frac{1}{2}\int \frac{\rho(\mathbf{r})\rho(\mathbf{r}')}{|\mathbf{r}_i - \mathbf{r}_i'|}d\mathbf{r}d\mathbf{r}' + E_{xc}[\rho(\mathbf{r})] + \int \rho(\mathbf{r})V_{ext}(\mathbf{r})d\mathbf{r} \tag{1.23}$$

where, $T_s[\rho(\mathbf{r})] = \frac{\hbar^2}{2m}\sum_{i=1}^{N}\int \phi_i^*(\mathbf{r})\nabla^2\phi_i(\mathbf{r})d\mathbf{r}$ and $V_{xc} = \frac{\delta E_{xc}[\rho(\mathbf{r})]}{\delta\rho(\mathbf{r})}$. The V_{xc} is called exchange-correlation potential. Since the potential V_{xc} is not known exactly, it has to be approximated. The problem of solving the Kohn-Sham equation is done in a self-consistent way. First, an initial guess for $\rho(\mathbf{r})$ is considered and then the corresponding V_s is calculated. After that, $\{\phi_i(\mathbf{r})\}$ can be calculated by solving the Kohn-Sham equations. From these $\{\phi_i(\mathbf{r})\}$, one can calculate a new density and start the process all over again. This procedure is then continued until a convergence is reached.

Exchange and Correlation Functionals

There are a variety of formalism for Exchange and Correlation energy functionals. Some of the popularly used ones are discussed below.

- **Local Density Approximation (LDA)**:

  The most simplest approximation to the exchange-correlation energy functional, $E_{xc}[\rho(\mathbf{r})]$, is the Local Density Approximation (LDA) [59] which is defined as:

$$E_{xc}^{LDA}[\rho] = \int d\mathbf{r}\epsilon_{xc}(\rho(\mathbf{r})) \cdot \rho(\mathbf{r}) \tag{1.24}$$

  where $\epsilon_{xc}(\rho(\mathbf{r}))$ is the exchange and correlation energy per electron of the homogeneous electron gas with density $\rho(\mathbf{r})$. In this approach, it is considered that the electronic density, $\rho(\mathbf{r})$, is a smooth and homogeneous function in space. Then, any region in space can be treated as a homogeneous electron gas. For spin polarized calculation, the generalization of the LDA is called local spin-density approximation (LSDA) which is defined as,

$$E_{xc}^{LSDA}[\rho_\uparrow, \rho_\downarrow] = \int d\mathbf{r}\epsilon_{xc}(\rho_\uparrow, \rho_\downarrow) \cdot \rho(\mathbf{r}) \tag{1.25}$$

- **Generalized Gradient Approximation (GGA)**:

  It is an extended and improved version of LDA functional to inhomogeneous systems. In case of LDA approximation, the exchange-correlation energy for electron gas is uniform at every point in the system. In general, for non-uniform charge densities, the exchange-correlation energy

can deviate significantly from the uniform result. This deviation can be expressed in terms of the gradient and higher spatial derivatives of the total charge density. In case of GGA approximation, the local exchange and correlation energy depends not only on the local electron densities but also on their gradients. Therefore, the GGA has proved to be an improvement over LDA for systems where the charge density is slowly varying. There are a variety of formalism for GGA approximation. [60–66]. The exchange and correlation energy is defined as,

$$E_{xc}^{GGA}[\rho, \vec{\bigtriangledown}\rho] = \int d\mathbf{r}\epsilon_{xc}(\rho, \vec{\bigtriangledown}\rho) \cdot \rho(\mathbf{r}) \tag{1.26}$$

while, for spin polarized systems the the exchange and correlation energy is defined as,

$$E_{xc}^{GSGA}[\rho_\uparrow, \rho_\downarrow, \vec{\bigtriangledown}\rho_\uparrow, \vec{\bigtriangledown}\rho_\downarrow] = \int d\mathbf{r}\epsilon_{xc}(\rho_\uparrow, \rho_\downarrow, \vec{\bigtriangledown}\rho_\uparrow, \vec{\bigtriangledown}\rho_\downarrow) \cdot \rho(\mathbf{r}) \tag{1.27}$$

- **Hybrid Functionals**:

  In these type of approximations the exchange and correlation energy includes a mixture of Hartree-Fock exchange with exchange and correlation from other sources. One of the most commonly used hybrid functional is B3LYP, which stands for Becke, 3-parameter, Lee-Yang-Parr. [67]

- **Long range corrected functionals**:

  The non-Coulomb part of exchange functionals typically dies off very rapidly and becomes less accurate at large distances. Therefore, it

is not accurate for modeling processes such as electron excitations to higher energy orbitals. Various types of formalisms have been adopted to handle the systems with significant dispersive interactions. CAM-B3LYP [68] and ωb97xd [69] are the most commonly used long range corrected functionals.

Pseudopotentials and Numerical Orbitals

In computational physics or chemistry, pseudopotential is used as an approximation for the simplified description of complex systems. Pseudopotential approximation is used for (a) reduction of basis set size, (b) reduction of effective number of electrons for explicit consideration and (c) inclusion of relativistic and other effects. Generally it is known that, the core electrons do not participate in chemical bonding and are unaffected by changes in their chemical environment. Therefore, it is a good approximation to consider that all the core electrons of an atom are frozen and an effective external potential experienced only by valence electrons in the atom. The pseudopotentials are obtained by constructing smoother wave functions in which the oscillations of the valence wave function in the core region are removed [70,71]. The pseudo wave function and all electron wave function becomes well comparable with each other beyond a particular value of radial distance, which is chosen to be outside of the last node in the all electron wave function; this is called the cutoff radius r_c. If we can use the same pseudopotential to describe different chemical environments, the pseudopotential is termed as transferable. A good pseudopotential needs to fulfill the following conditions:

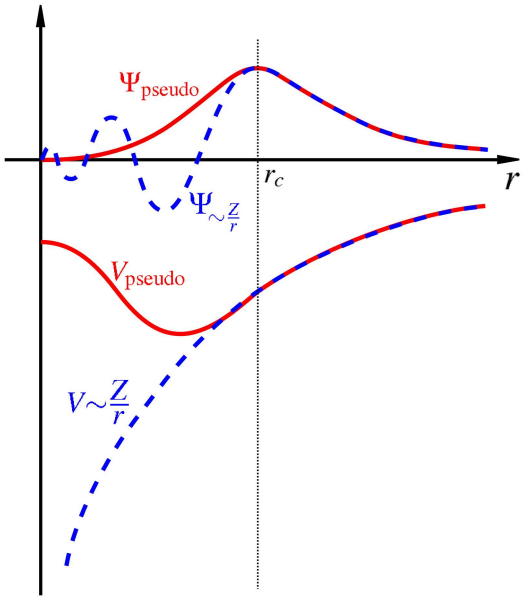

Figure 1.7: Comparison of a wave function in the Coulomb potential of the nucleus (blue) to the one in the pseudopotential (red). [1] The real and the pseudo wave function and potentials match above a certain cutoff radius r_c.

- The lowest pseudo wave function generated by the pseudopotential generalization method should not contain any nodes.

- The normalized atomic radial pseudo wave function with an angular momentum l should be equal to the normalized radial all electron (AE) wave function outside a given cut-off radius r_c (Fig. 1.7):

$$R_i^{PP}(r) = R_i^{AE}(r) \ (r > r_c) \tag{1.28}$$

- Norm conservation: The charge inside of r_c has to be the same for both wave functions,

$$\int_0^{r_c} |R_i^{PP}(r)|^2 r^2 dr = \int_0^{r_c} |R_i^{AE}(r)|^2 r^2 dr \tag{1.29}$$

- The eigenvalues of both wave functions should be the same.

There are many packages for the self-consistent calculations of electronic structure using Hartree-Fock, post Hartree-Fock and DFT methods. Some of these packages which have been used to study atoms, molecules or nanomaterials are Gaussian [72], General Atomic and Molecular Electronic Structure System (GAMESS) [73] and Amsterdam Density Functional (ADF) [74] etc. However, since these packages use atom centered basis functions, one cannot handle larger systems. A combination of atom centered basis functions with pseudopotentials make an ideal choice for studying large systems. This has been implemented in the Spanish Initiative for Electronic Simulations with Thousands of Atoms (SIESTA) package [75], making it

an ideal choice for studying realistic systems of large sizes. Other than these, one may adopt Carr-Parrinello Molecular Dynamics (CPMD) [76] and Self-Consistent-Charge Density-Functional Tight-Binding (SCC-DFTB) [77] methods to study electronic structure and properties for larger systems. However, projector augmented wave method (PAW) is implemented in Vienna Ab-initio Simulation Package (VASP) [78] and for plane wave basis set one may use Quantum ESPRESSO. [79]

1.6.4 Classical Molecular Dynamics

Modeling of the complex and large systems using the solution of time-dependent Schrödinger equation is a difficult task, and only a few atoms can be handled at the *ab inito* level. Again, macroscopic properties of a system are always ensemble averages over a representative statistical ensemble for both equilibrium and non-equilibrium states. Therefore, the knowledge of a energy minimized single structure is not sufficient. In order to calculate macroscopic properties of a system, it is required to generate a representative ensemble at a given temperature and/or pressure. There are two methods which are mostly used for the generation of a representative equilibrium ensemble: (a) Monte Carlo simulations and (b) Molecular Dynamics (MD) simulations. Monte Carlo simulations do not require the computation of forces and hence they are more simpler than the MD simulations. Also, Monte Carlo simulations do not yield significantly better statistics than MD simulations in a given amount of computer time. Again, MD simulations are most appropriate for the generation of non-equilibrium ensembles for the analysis of

dynamic events. Therefore, MD is the more universal technique within an affordable computational cost. Although, MD simulation may fail if a starting configuration is very far from equilibrium, however, in such cases special techniques have to be adopted.

In MD simulations, one uses a conservative force field that is a function of the positions of nuclei only and the electronic motions are not considered. The electrons always remain in their ground state and adjust their dynamics instantly with the change in the atomic positions (Born-Oppenheimer approximation). Solving the Newtonian equations of motion for all the nuclei (or atoms) within a system is the basic foundation of the classical MD simulations. The Newtonian equations of motion for a system of N interacting atoms are expressed as:

$$\mathbf{F}_i = m_i \frac{\partial^2 \mathbf{r}_i}{\partial t^2} \qquad i = 1, 2, ..., N \tag{1.30}$$

where, m_i is the mass of the i-th nucleus and t denotes the time. The forces, $\mathbf{F}_i (i = 1, ..., N)$ are the negative gradients of the potential energy function $U(\mathbf{r}_1, \mathbf{r}_2, ..., \mathbf{r}_N)$:

$$\mathbf{F}_i = -\vec{\bigtriangledown}_i U(\mathbf{r}_1, \mathbf{r}_2, ..., \mathbf{r}_N) \qquad i = 1, 2, ..., N \tag{1.31}$$

These equations (eqn. 1.30 and eqn. 1.31) are solved simultaneously in small time steps (Δt). The system is evolved for some time to achieve the equilibrium at constant temperature and pressure. The coordinates are written to an output file at regular intervals of time which will eventually generate

the trajectory of the system. Then from the equilibrium trajectory, required macroscopic properties can be calculated.

A MD simulation requires the definition of a potential function by which the particles in the simulation will interact. This potential energy function can be approximated and described in terms of some parameters which are known as force field. There are several integration methods for the integration of eqn. 1.30. The temperature and pressure can be kept constant at a required value by means of a temperature and pressure coupling method. We use Ewald summation method for the treatment of long range electrostatics part of the potential functions. Here we have briefly discussed about force field, the integration methods of the equation of motions, different temperature coupling methods (thermostat), different pressure coupling methods (barostat) and finally Ewald summation method.

Force Fields

The potential function, U, mentioned above, consists of a summation of (i) bonded forces associated with chemical bonds, bond angles, bond dihedrals and (ii) non-bonded forces associated with van der Waals forces and electrostatic charges.

$$U = U_{bonded} + U_{non-bonded} \tag{1.32}$$

(i) The contribution to the bonded inter-atomic potential (U_{bonded}) is given as:

$$U_{bonded} = \sum_{bonds} K_r(r - r_0)^2 + \sum_{angles} K_\theta(\theta - \theta_0)^2 + \sum_{improper} K_\omega(\omega - \omega_0)^2 + \sum_{dihedrals} K_\phi(1 + \cos(n\phi - \phi_0)) \quad (1.33)$$

where, bond, angle and improper interactions are described by harmonic potentials based on Hooke's law. A periodic function is used for the description of potential due to dihedral angles.

(ii) The non-bonded interactions ($U_{non-bonded}$) are decomposed into two parts: electrostatic Coulomb potential, $U_{Coulomb}$, and a combination of van der Waals attractive and Pauli repulsion part. The latter part is defined usually by Lennard-Jones (LJ) potential, U_{LJ}. Thus, the non-bonded interactions are expressed as:

$$U_{non-bonded} = U_{Coulomb} + U_{LJ} \quad (1.34)$$

$$U_{Coulomb} = \sum_{i,j(j>i)} \frac{1}{4\pi\epsilon_0\epsilon_r} \frac{q_i q_j}{r_{ij}} \quad (1.35)$$

$$U_{LJ} = \sum_{i,j(j>i)} 4\epsilon_{ij} \left(\left(\frac{\sigma_{ij}}{r_{ij}} \right)^{12} - \left(\frac{\sigma_{ij}}{r_{ij}} \right)^{6} \right) \quad (1.36)$$

where, ϵ_0 and ϵ_r are the dielectric constant in vacuum and the relative dielectric constant of medium (for water, 78), respectively. ϵ_{ij} is the depth

of the LJ potential well, σ_{ij} is the finite distance at which the inter-particle potential is zero and r_{ij} is the distance between the i-th and j-th particles.

All the parameters in Eqn. 1.33, Eqn. 1.35 and Eqn. 1.36 are required for a MD simulations of a given system. These parameters are obtained by fitting against detailed electronic structure method calculations (quantum mechanical calculation) or from the comparison with measured experimental physical properties such as elastic constants, lattice parameters and spectroscopic measurements. These parameters differ from system to system. There are different force fields, designed for different purposes. Among them AMBER (Assisted Model Building and Energy Refinement) [80], CHARMM (Chemistry at HARvard Molecular Mechanics) [81–83] and GROMOS (GROningen MOlecular Simulation) [84, 85] force fields are commonly used for molecular dynamics of macromolecules, by many researchers.

Integration Algorithms

Molecular dynamics simulation starts with given molecular positions, velocities, and other dynamical informations at time, t. The attempt is to obtain the positions, velocities etc. at later time $t + \Delta t$, to a sufficient degree of accuracy. The entire trajectory can be obtained in this way through the accumulation of data at different times. Computation of the trajectory requires solving of 3N second order differential equation (Eqn. 1.30) in each time step, where N is the number of particles in the system. Finite difference approach is a standard method for solution of ordinary differential equations (Eqn. 1.30 and Eqn. 1.31). There are many different algorithms which fall into the category of general finite difference algorithm. The most widely used

method of integrating the equation of motion is Verlet algorithm [86]. In this method, the equation for updating the position of i-th particle is given by:

$$\mathbf{r}_i(t + \Delta t) = 2\mathbf{r}_i(t) - \mathbf{r}_i(t - \Delta t) + \Delta t^2 \mathbf{a}_i(t) \tag{1.37}$$

where, $\mathbf{r}_i(t)$ and $\mathbf{a}_i(t)$ are the position and acceleration of i-th particle at time t, respectively and $\mathbf{r}_i(t - \Delta t)$ is the position of the i-th particle at time $t - \Delta t$. The Eqn. 1.37 appears after the addition of equations obtained by Taylor expansion about $\mathbf{r}_i(t)$:

$$\mathbf{r}_i(t + \Delta t) = \mathbf{r}_i(t) + \Delta t \mathbf{v}_i(t) + (1/2)\Delta t^2 \mathbf{a}_i(t) + ... \tag{1.38}$$

$$\mathbf{r}_i(t - \Delta t) = \mathbf{r}_i(t) - \Delta t \mathbf{v}_i(t) + (1/2)\Delta t^2 \mathbf{a}_i(t) - ... \tag{1.39}$$

where $\mathbf{v}_i(t)$ is the velocity of the i-th particle at time t. The velocities are important to compute the kinetic energy of the system and not needed to compute the trajectories. The velocity of i-th particle at time t can be calculated from the equation:

$$\mathbf{v}_i(t) = \frac{\mathbf{r}_i(t + \Delta t) - \mathbf{r}_i(t - \Delta t)}{2\Delta t} \tag{1.40}$$

The leap-frog algorithm is equivalent to the Verlet algorithm and updates both positions and velocities at time t:

$$\mathbf{r}_i(t + \Delta t) = \mathbf{r}_i(t) + \Delta t \mathbf{v}_i(t + \frac{\Delta t}{2}) \tag{1.41}$$

$$\mathbf{v}_i(t + \frac{\Delta t}{2}) = \mathbf{v}_i(t - \frac{\Delta t}{2}) + \Delta t \mathbf{a}_i(t) \tag{1.42}$$

The accuracy of the algorithm is up to third order and follow the time-reversibility. The MD simulations without any couplings to heat and pressure baths result in NVE ensemble (constant particles, volume and total energy) which is also known as the micro-canonical ensemble. On the other hand, coupling to a heat bath gives the NVT ensemble, *i.e.*, the canonical ensemble, in which the temperature is conserved and coupling to both heat and pressure bath gives NPT ensemble, in which both pressure and temperature are conserved. The realization of NPT ensemble appears to be most relevant to the laboratory conditions.

Temperature Coupling

In MD simulations, temperature can be kept around an average value, T_0, by coupling the system to an external heat bath of temperature, T_0. There are different methods which have been proposed for temperature coupling. The popular methods include the Berendsen thermostat, velocity rescaling, the Andersen thermostat, the Nosé-Hoover thermostat, Nosé-Hoover chains and Langevin dynamics. Here, we briefly describe the (i) Berendsen thermostat, (ii) velocity rescaling and (iii) the Nosé-Hoover thermostat.

(i) **Berendsen thermostat**:

In case of Berendsen thermostat [87], the system is weakly coupled to a heat bath with some reference temperature. The system temperature (T) deviates exponentially from the reference temperature (T_0). If the

time constant of the temperature coupling is τ_T, then

$$\frac{dT}{dt} = \frac{T_0 - T}{\tau_T} \tag{1.43}$$

And the velocity scaling factor, λ, is calculated from the equation:

$$\lambda = \sqrt{1 + \frac{\Delta t}{\tau_T}\left(\frac{T_0 - T}{T}\right)} \tag{1.44}$$

The Berendsen thermostat does not generate a correct canonical ensemble (especially for small systems), as it suppresses the kinetic energy fluctuations of the system. However, for a large system, this scheme is widely used.

(ii) **Velocity-rescaling thermostat**:

In the simplest formulation of velocity-rescaling method, the velocities of all the particles is multiplied by a factor α, calculated by enforcing the total kinetic energy K to be equal to the average kinetic energy ($\bar{K}$) at the reference temperature (T_0). $\bar{K}$ at the reference temperature (T_0) is defined as $\bar{K} = k_B T_0 N_f/2$, where, N_f is the number of degrees of freedom and k_B is the Boltzmann constant. The rescaling factor α for the velocities is obtained as:

$$\alpha = \sqrt{\frac{\bar{K}}{K}} \tag{1.45}$$

In case of velocity-rescaling method proposed by Bussi *et al.* [88], instead of forcing the K to be exactly equal to $\bar{K}$, K_t is chosen with

a stochastic procedure aimed at obtaining the desired ensemble. The rescaling factor α for the velocities becomes,

$$\alpha = \sqrt{\frac{K_t}{K}} \tag{1.46}$$

where, K_t is drawn from the canonical equilibrium distribution:

$$P(K_t)dK_t \propto K_t^{(N_f/2-1)} e^{-K_t/k_B T_0} dK_t \tag{1.47}$$

where, $P(K_t)dK_t$ is the probability of getting K_t with in K_t and $K_t + dK_t$.

(iii) **Nosé-Hoover thermostat**:

For Nosé-Hoover thermostat [89, 90], a heat bath is introduced in the Hamiltonian with an extra degree of freedom, s.

$$H = \sum_i \frac{{p_i}^2}{2m_i s^2} + \sum_{i,j(j>i)} U(\mathbf{r}_i - \mathbf{r}_j) + \frac{{p_s}^2}{2Q} + g k_B T ln(s) \tag{1.48}$$

where, g is the number of independent momentum degrees of freedom of the system and Q (fictitious mass) is a parameter that should be chosen carefully. p_s is the conjugate momentum of s. Then the Lagrangian equation of motion can be written as:

$$\frac{\partial^2 \mathbf{r}_i}{\partial t^2} = \frac{\mathbf{F}_i}{m_i} - \gamma \mathbf{r}_i \quad i = 1, 2, ..., N \tag{1.49}$$

$$\frac{\partial \gamma}{\partial t} = -\frac{k_B(g-1)}{Q} T \left(\frac{g}{g-1} \frac{T_0}{T} - 1 \right) \tag{1.50}$$

where, $\gamma = \frac{1}{s}\frac{\partial s}{\partial t}$.

Pressure Coupling

Similar to the temperature coupling, sometimes it is also important to simulate a system at constant pressure. The pressure of a system can be kept around a particular value (p_0) by coupling the system with a pressure bath (barostat). Among several methods, Berendsen [87] and Parrinello-Rahman [91] pressure coupling schemes are important. Constant pressure is achieved by rescaling the coordinates of the particles and the dimensions of the simulation box. In the Berendsen method, the system is weakly coupled to an external bath. Similar to the temperature coupling, an extra term is added to the equations of motion that effects towards pressure change:

$$\frac{dp}{dt} = \frac{p_0 - p}{\tau_p} \tag{1.51}$$

where, τ_p is the time constant for the coupling. The proportional scaling constant (μ) for coordinates and box length is formulated as,

$$\mu = \left[1 - \frac{\Delta t}{\tau_p}(p_0 - p)\right]^{1/3} \tag{1.52}$$

Periodic Boundary Conditions and Long Range Electrostatics

Periodic Boundary Conditions (PBC) are a set of boundary conditions that are often used to simulate a large system to avoid the edge effects. In PBC, atoms that leave a box, enter the adjacent box on the opposite side with same velocity. And thus, the number of particles is always conserved and so

also their linear momentum.

Since non-bonded van der Waals interaction decays very fast with distance (*e.g.*, LJ interaction decays with distance as $\frac{1}{r^6}$), cut-off is used to reduce the computational cost. But, for the Coulomb interaction, the potential is inversely proportional to the distance. Therefore, the consideration of cut-off in case of Coulomb interaction is not a good idea. With PBC, the electrostatic potential energy of a system with N number of particles and with their periodic images is described as:

$$V_{Coulomb} = \frac{1}{8\pi\epsilon_0\epsilon_r} \sum_{n_x} \sum_{n_y} \sum_{n_z{}^*} \sum_{i}^{N} \sum_{j}^{N} \frac{q_i q_j}{r_{ij,\overrightarrow{n}}} \tag{1.53}$$

where $\overrightarrow{n}(= (n_x, n_y, n_z))$ is the box vector and $\mathrm{r}_{ij,\overrightarrow{n}}$ is the real distance between the particle i and the particle j. Note, the '*' in the summation indicates that, the terms with $i = j$ are discarded if $\overrightarrow{n} = \overrightarrow{0}$. However, the above sum converges very slowly. Ewald [92] introduced the idea of subdividing the slowly-converging sum into two fast-converging sums plus a constant term:

$$V_{Coulomb} = V_{Coulomb}^{direct} + V_{Coulomb}^{reciprocal} + V_{Coulomb}^{0} \tag{1.54}$$

Calculation of the reciprocal sum is computationally expensive and hardly affordable for the large systems. However, the Particle-Mesh Ewald (PME) method [93,94] improves the difficulty of calculating the reciprocal term and it is widely used for the treatment of long-range electrostatic interactions.

Steered Molecular Dynamics (SMD)

Steered Molecular Dynamics (SMD) accelerates conformational changes in systems through the application of external forces by pulling it along a desired degrees of freedom. Generally, SMD is used to study the folding/unfolding kinetics of biomolecular systems. There are two typical protocols of SMD:

(i) one in which pulling velocity is held constant and

(ii) another case where, applied force is kept constant.

Typically, a part of the system (*e.g.*, an atom or a group of atoms in a protein) is restrained by a harmonic potential and the forces are then applied to some other part of the system at either through a constant velocity or keeping a constant force.

Free Energy Calculation

Here, we discuss two methods for the calculation of change in free energy:

(i) **Thermodynamic Integration** [95]:

Consider two systems, 'A' and 'B' with enthalpies H_A and H_B, respectively. Now consider a new potential energy function defined as:

$$H(\lambda) = (1 - \lambda)H_A + \lambda H_B \tag{1.55}$$

where, λ is a coupling parameter with a value between 0 and 1. Hence, the energy of the system is a function of λ. Thus the system is 'A' for $\lambda = 0$ and the system is 'B' for $\lambda = 1$. The partition function of the

system can be written as:

$$Q(\lambda) = \sum_{s} exp[-H_s(\lambda)/k_B T] \tag{1.56}$$

where, $H_s(\lambda)$ is the potential energy of state s in the ensemble. And the free energy of the system is defined as:

$$G(\lambda) = -k_B T \ln Q(\lambda) \tag{1.57}$$

Then the change in free energy for the system to be transferred from 'A' to 'B' can be written as:

$$\begin{aligned} \Delta G(A \rightarrow B) \quad &= \int_0^1 d\lambda \frac{\partial G(\lambda)}{\partial \lambda} \\ &= -\int_0^1 d\lambda \frac{k_B T}{Q} \frac{\partial Q}{\partial \lambda} \\ &= \int_0^1 d\lambda \frac{k_B T}{Q} \sum_{s} \frac{1}{k_B T} \exp[-H_s(\lambda)/k_B T] \frac{\partial H(\lambda)}{\partial \lambda} \\ &= \int_0^1 d\lambda \left\langle \frac{\partial H(\lambda)}{\partial \lambda} \right\rangle_{\lambda} \end{aligned} \tag{1.58}$$

Thus the change in free energy ($\Delta G(A \rightarrow B)$) between 'A' and 'B' can be calculated from the integral of the ensemble average of the change in enthalpy with λ

(ii) **Umbrella Sampling** [96]:

Umbrella sampling can be used to move a system along the desired reaction coordinate by varying, *e.g.*, the forces, distances, and angles manipulated in the simulation. A bias potential (an additional energy

term) is applied to the system to ensure efficient sampling along the reaction coordinate. Through umbrella sampling, all of the system's configurations (both high-energy and low-energy) can be sampled adequately. Then, for each configuration, the free energy is calculated as the Potential of Mean Force (PMF). After the simulations, the free energy curves are combined with a particular techniques. The most popular method of computing PMF is through the Weighted Histogram Analysis Method (WHAM).

1.7 Softwares and Hardwares used

All the DFT calculations reported in this thesis were carried out using Gaussian [72], and SIESTA [75] packages. Classical molecular dynamics simulations were carried out using GROMACS-4.0.7 [97] package. Xmgrace [98] and gnuplot [99] packages were used for plotting. Visualizations and graphical analyses were done using GaussView [100], Xcrysden [101] and VMD [102] visualization softwares. Many of the results were analyzed using home developed codes. The work reported in this thesis required expensive computational calculations which were performed on dedicated clusters as well as resources available in central facilities at Center for Computational Materials Science (CCMS), JNCASR.

1.8 Outline of Thesis

In this thesis, we have studied the structural, energetics, optical and magnetic properties of few DNA and modified DNA systems. Majority of the works in this thesis have been carried out using Density Functional Theory (DFT) and Molecular Dynamics (MD) simulations. The thesis is divided into six chapters.

In this chapter, we have briefly discussed the systems that we have studied in this thesis. Overviews of different computational methodologies used in the subsequent chapters, *viz.*, DFT, MD and Heisenberg models are discussed.

In the next chapter, we investigate the structure, energetics, bonding aspects and optical properties of two different analogues of RNA nucleosides (thieno modified and size-expanded nucleosides). We have compared these results against the findings obtained for the natural and both the modified nucleosides, as well as with the available experimental data.

In the third chapter, we study the structures, energetics, electronic, and optical properties of a duplex DNA, containing metal-mediated base pairs. There are three imidazole (Im) units linked through metal (Im-M-Im, M = metal) and four flanking A:T base pairs (two on each side) in a DNA duplex. We examined the role of the metal ions for the formation of the metal-mediated base pairing in the DNA duplex.

In the fourth chapter, we consider DNA duplex, modified with either hydroxyperidone (H) or bis-(salicylaldehyde)-ethylenediamine (S-en) metalated bases with a variety of transition metal ions and look into the structures, energetics, magnetic and optical properties. The magnetic interactions and

the exchange coupling constants (J) are calculated considering Heisenberg Hamiltonian.

In the fifth chapter, we study the formation of a few atoms metal (Silver and Gold) clusters in presence of ssDNA in aqueous media at neutral pH. These few atoms metal clusters have high applicability in bio-systems as fluorescent sensors. MD simulation is used to study the encapsulation of the few atoms metal cluster by different ssDNA and DFT is used to explain their optical properties.

In the sixth (last) chapter, we explore the kinetics and folding pathway of Human Telomeric G-quadruplex. We study the folding kinetics of single human telomeric G-quadruplexes in presence of different alkali metal ions (Na^+ and K^+) using steered molecular dynamics simulation.

Chapter 2

Structural, Electronic and Photophysical Properties of Analogous RNA Nucleosides*

2.1 Introduction

The interaction between UV-visible radiation and the amino acids, nucleic acids or their constituents are important to study due to their importance in implications for life. [103] However, natural amino acid and nucleic acid residues do not show fluorescence emission, hence, long chain protein and nucleic acids act as fluorescence inactive materials. Interestingly, a long chain polymer of amino acids or nucleic acids can be synthesized with natural as

*Works reported in this chapter are published in: (a) P. K. Samanta, A. K. Manna, and S. K. Pati, J. Phys. Chem. B **116**, 7618-7626 (2012). Reprinted (adapted) with permission from American Chemical Society (b) P. K. Samanta and S. K. Pati, New J. Chem. **37**, 3640-3646 (2013). Reproduced by permission of The Royal Society of Chemistry (RSC) on behalf of the Centre National de la Recherche Scientifique (CNRS) and the RSC.

well as artificial residues with the help of recent advancement of biotechnology, [104, 105] which helps to introduce a new property to a protein or a nucleic acid chain. Therefore, modified amino acid and nucleic acid residues, having fluorescence activity in UV-visible region are very much important for improved biological and biomedical applications. [28, 106–108] Several theoretical and experimental studies have been reported in the literature on natural as well as modified base pair of the nucleosides (or nucleobases) which include various metal-modified Watson-Crick (WC) base pairs [109–114] and artificial base pairs [115–122], analogues of natural nucleosides. These motivate scientists to explore new analogues of nucleosides in order to explore their structural stability, electrical conductivity, optical and magnetic properties. [31, 123]

The key criterion for the design of fluorescence active nucleic acid residue is to minimize structural and functional perturbations. [28, 124] Therefore, it is important to design the emissive nucleoside analogues which show strong structural resemblance with their natural analogues. Natural ribonucleic acid (RNA) consists of four types of nucleosides: Adenine (A), Uracil (U), Guanine (G) and Cytosine (C). Shin *et al.* synthesized four isomorphic analogues of natural RNA nucleic nucleosides, thieno-modified RNA nucleosides; *viz.*, thA, thU, thG and thC (see Fig. 2.1) and reported their photophysical properties. [29] Another way of modification can be done by extending the conjugation of natural nucleobases by inserting additional aromatic rings onto the pyrimidine and purine moiety. [125–129] Zgierski *et al.* have reported the incorporation of trimethylene ring to eliminate the internal conversion of C and U nucleobases. Because of the extra conjugation, this class of

modified nucleosides show red-shift in their absorption spectra, compared to their natural analogues. There is an increase in the fluoresce life time of 5,6-trimethylenecytosine (TMC) and 5,6-trimethyleneuracil (TMU) compared to their natural analogues, C and U, respectively. [130] The sizes of the WC base pairs increase due to the additional aromatic rings. Hernandez *et al.* synthesized size-expanded modified RNA nucleosides by fusing additional benzene ring onto the pyrimidine and purine nuclei; *viz.*, ^{x}A, ^{x}U, ^{x}G and ^{x}C (see Fig. 2.1) and reported their excitation and emission properties. [30] In fact, this additional benzene ring increases the size of the WC base pairs by $\sim$4.8 $\mathring{A}$.

Motivated by the experimental work of Shin *et al.* [29] and Hernandez *et al.* [30], we have explored the structural, energetics, and photophysical properties of these modified ribo-nucleosides (thA, thU, thG, thC, ^{x}A, ^{x}U, ^{x}G, and ^{x}C) using *ab initio* Density Functional Theoretical (DFT) calculation. We have studied the structures and the propensity of the WC base pair formation in between two complementary nucleosides of natural, thieno-modified and size-expanded nucleosides. We also have looked into the formation of WC like base pair between a modified nucleoside and its complementary natural nucleosides. The photophysical properties of the modified nucleosides are calculated and found reasonably in good agreement with the experimentally reported results. In this study, we have provided a microscopic origin of the low-energy absorption peaks and emission peaks.

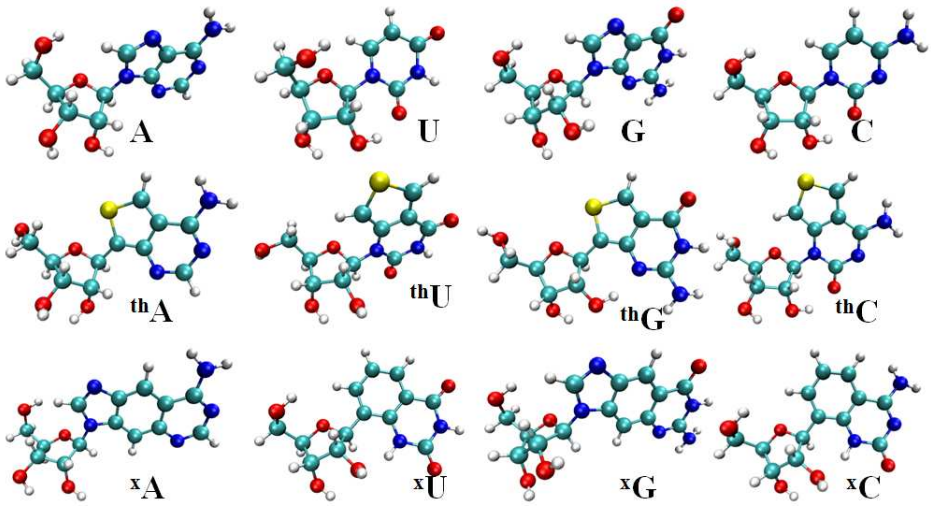

Figure 2.1: Optimized structures of natural RNA nucleosides, their thieno-analogues (thieno[3,4-d] pyrimidine nucleosides) and sized-expanded RNA nucleosides. Atom color code: blue (N), cyan (C), white (H), red (O), and yellow (S).

2.2 Computational Methods

The geometry of various RNA nucleosides and their modified analogues (thA, thU, thG, thC, ^{x}A, ^{x}U, ^{x}G, and ^{x}C) were optimized using DFT, and their optical spectra were calculated using time-dependent DFT (TD-DFT) methods as implemented in the Gaussian 09 program package [72]. All the calculations were performed using B3LYP [64, 131, 132] hybrid exchange and correlation energy functional, with 6-31++G(d, p) basis set for all atoms. To study the H-bonded WC base pair, we model the system by replacing sugar moiety with methyl group of each nucleosides. For the H-bonded WC base pairs, we also have invoked M06-2X [133] and ωB97XD [69, 134] exchange and correlation energy functional in order to take into account the weak non-covalent interactions, such as H-bonding and van der Waals interactions. Note that, the

structure and energy of the H-bonded nucleobase pairs are strongly dependent on the level of calculations. The DFT and TD-DFT calculations were performed both in gas phase and with water surrounding, using polarized continuum model (PCM) [135] to include the solvent (water) effect. After geometry optimization, frequency calculations were done to remove any vibrational unstable mode and also to calculate zero-point energy (ZPE). The convergence criterion for the self-consistent-field (SCF) was set to 'Tight', and the 'UltraFine' grid was used for numerical integration in DFT, as implemented in Gaussian 09 sets of code. Excited state geometry for all the nucleosides were optimized using TD-DFT method. Then the emission spectra were calculated using optimized first excited state (S_1) geometry of each nucleosides.

2.3 Results and Discussion

2.3.1 Structural and energetics analysis of the WC base pairs

First, we focus our attention on the nature of the H-bonding (WC base pairing) pattern in thieno-nucleobases and the size-expanded nucleobases. We then compare the results against their natural analogues. In WC base pairs of natural nucleobases, A and U are connected by two H-bonds (N-H$\cdots$N + N-H$\cdots$O) while G and C are connected by three H-bonds (N-H$\cdots$N + 2N-H$\cdots$O). In order to model the H-bonding pattern in these nucleosides, the sugar part of each nucleoside is replaced by methyl group which does not

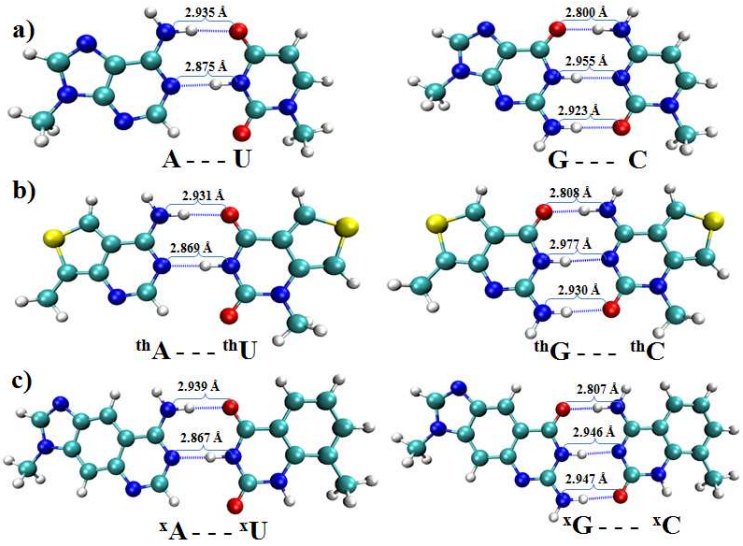

Figure 2.2: H-bonding between A:U, G:C (a), thA:thU, thG:thC (b) and ^{x}A:^{x}U, ^{x}G:^{x}C (c). Atom color code: blue (N), cyan (C), white (H), red (O), and yellow (S).

impose major structural changes in nucleobases. This has been successfully used in previous studies concerning the base pairing of nucleobases. [109,111, 136–138] Thieno-nucleobases and size-modified nucleobases also form WC base pair as found for natural nucleobases. The fully relaxed structures of all nucleosides and WC base pairs formed by both natural as well as modified nucleobase analogues are shown in the Fig. 2.1 and Fig. 2.2, respectively.

We have found that the overall distance between H-bond donor and acceptor is slightly decreased for A:U base pair, while there is an increment in H-bond distance for G:C pair upon thieno modification. However, for the size-expanded nucleobase pairs, the H-bond distance remain almost same as in natural WC base pair. The distance values for the WC pair are shown in the Fig. 2.2. The small changes in the H-bonding distance are associated with the changes in N-H bond length in individual nucleobases present in the

WC base pair. This is because of the difference in partial charge distributions in these different types of nucleobases. The strength of H-bonding interactions between the WC base pairs of modified nucleobases are compared with their natural analogues. The stabilization energy (ΔE_{stab}) due to WC base pairing of these nucleobases is calculated using the following equation:

$$\Delta E_{stab} = E_{(A:U/G:C)} - E_{(A/G)} - E_{(U/C)} \tag{2.1}$$

where, $E_{(A:U/G:C)}$ and $E_{(A/U/G/C)}$ are the optimized energy of WC base pair A:U (or G:C) and is the optimized energy of individual nucleobases (A/G/U/C), respectively. The calculated stabilization energies of thA:thU (^{x}A:^{x}U) and thG:thC (^{x}G:^{x}C) are -12.80 kcal mol^{-1} (-12.64 kcal mol^{-1}) and -23.99 kcal mol^{-1} (-24.64 kcal mol^{-1}), respectively, obtained with B3LYP/6-31++g(d, p) level of calculations (see Table 2.1). Whereas, the stabilization energies of A:U and G:C are -12.88 kcal mol^{-1} and -25.98 kcal mol^{-1}, respectively. Our results are consistent with the previously reported theoretical results for the natural nucleobases [133]. We have found that the stabilization energy due to the WC base pair formation between thieno-nucleobases or size-expanded nucleobases is comparable with the WC base pair formation of the natural nucleobases. Note that, although there is a very small increase in ΔE_{stab} (less stable), ∼0.08 kcal mol^{-1} (∼0.24 kcal mol^{-1}) for thA:thU (^{x}A:^{x}U) compared to natural A:U, we find ∼2 kcal mol^{-1} (1.5 kcal mol^{-1}) increase in stabilization energy while going from thG:thC (^{x}G:^{x}C) to G:C with the later one showing greater extent of stabilization. These results show that the modified

nucleobases can also form similar kind of WC base pairing as the natural nucleobases. Blas *et al.* have reported the formation of WC base pairing of size-expanded nucleobases with complementary natural nucleobases as well as with complementary size-expanded nucleobases using classical molecular dynamics simulations. [139] Experimentally, the formation of WC base pairing of size-expanded nucleobases with the complementary natural nucleobase have been reported. [140, 141] To test the reliability of the employed B3LYP exchange and correlation functional for the calculation of the stability energy because of WC base pair formation for these H-bonded nucleobases, we also have computed the stabilization energy using two different exchange correlation energy functional; *viz.*, M06-2X and ωB97XD with the same basis set, 6-31++g(d, p). Although ΔE_{stab} is found to be increased slightly, the overall trend in ΔE_{stab} energy remains same for these WC base pairs for both the modified and natural nucleobases. We have found small increase (3-5 kcal mol^{-1}) in ΔE_{stab} with respect to the usage of B3LYP functional. This is because of the incorporation of short and long range van der Waals interactions by these exchange correlation energy functional. We also have calculated the stabilization energy, ΔE_{stab}, corrected with basis set superposition error (BSSE) and zero point energy (ZPE) and tabulated in Table 2.1 for all exchange and correlation energy functional used in our study. The BSSE is calculated using counter-poise method. [142, 143] We find that there is a very small change in the stabilization energy, and the overall findings still remain same even after inclusion of BSSE and ZPE corrections. To find the H-bonding energy profile when the base pairs are modified by these

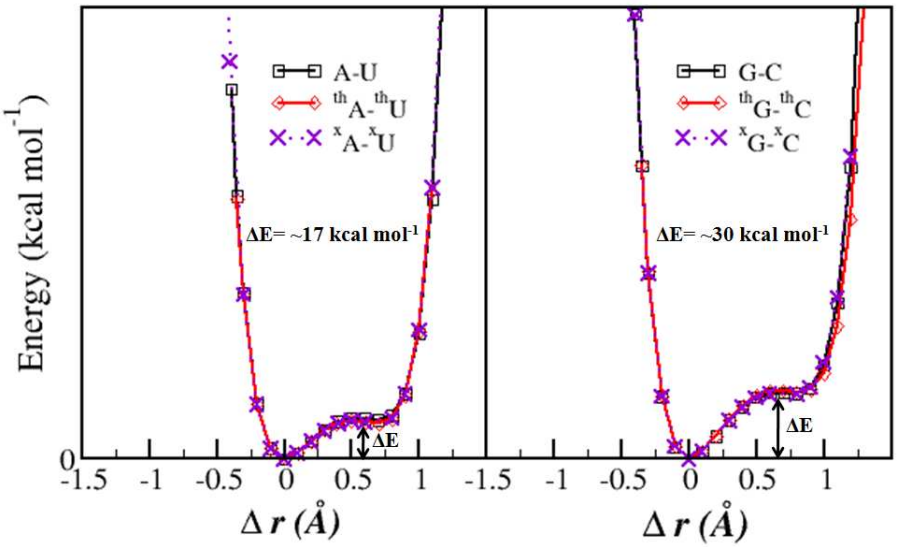

Figure 2.3: H-bonding potential profile for A:U, thA:thU, ^{x}A:^{x}U, G:C, thG:thC and ^{x}G:^{x}C.

present nucleobases, we calculate H-bonding energy profile with varying distance between H-atom and H-donor/acceptor atom of individual nucleobases. Earlier studies have shown that the conventional H-bonding energy profile in WC base pairs formation shows a double-well potential with the bridged hydrogen (H) atom, forming a transitional state between two minimal energy states, D-H$\cdots$A and D$\cdots$H-A, where, D and A are the donor and acceptor, respectively. [144]

For the quantitative estimation of the H-bonding profiles in the case of both the modified as well as natural nucleobases pairs, we plot the H-bonding energy profiles for the N-H$\cdots$N bond for thA:thU (^{x}A:^{x}U) and thG:thC (^{x}G:^{x}C) and compare the same with the results obtained for A:U and G:C (shown in Fig. 2.3). The nature of the double-well H-bonding energy profile; *i.e.*, characteristic two energy minima, for the natural WC base pairs remain same after thieno modification and after size-expanding. As shown in Fig. 2.3, we

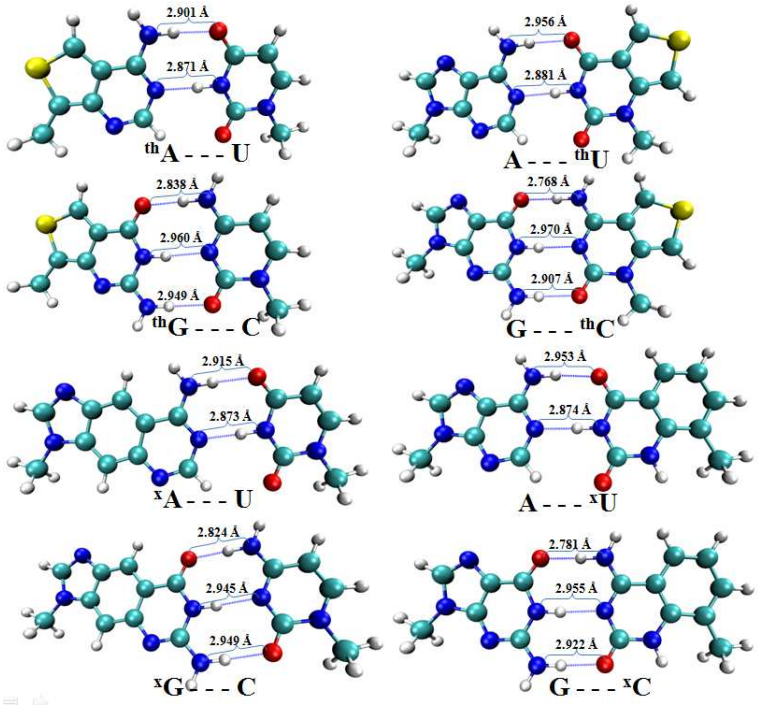

Figure 2.4: Watson-Crick like base pairing between the thieno-nucleosides and size-expanded nucleosides with their natural complementary nucleoside. Atom color code: blue (N), cyan (C), white (H), red (O), and yellow (S).

find that the two energy minima are separated by ∼17 kcal mol^{-1} and ∼30 kcal mol^{-1} for A:U/thA:thU/^{x}A:^{x}U and G:C/thG:thC/^{x}G:^{x}C pairs, respectively. These results suggest that both the modified analogues base pairs can form WC base pairing to form duplex DNA/RNA through the stable WC H-bonding interaction as found for the natural nucleobases. [137, 145]

It is also interesting to investigate whether a thieno-modified nucleobases or a size-expanded nucleobases can form WC base pairs with its complementary natural nucleobases. WC base pairing between the thieno-nucleosides and size-expanded nucleosides with their natural complementary nucleoside

Table 2.1: H-bonding stabilization energy (ΔE_{stab} in kcal mol^{-1}) and its Basis Set Superposition Error (BSSE) and zero-point-energy (ZPE) corrected values with different exchange and correlation energy functionals.

Energy	Nucleosides	B3LYP	M06-2X	ωB97XD
ΔE_{stab}	A:U	-12.88	-15.25	-16.48
	thA:thU	-12.80	-15.16	-16.48
	thA:U	-13.58	-15.97	-17.35
	A:thU	-12.27	-14.68	-15.81
	^{x}A:^{x}U	-12.64	-14.84	-16.19
	^{x}A:U	-13.07	-15.35	-16.81
	A:^{x}U	-12.53	-14.92	-16.05
	G:C	-25.98	-28.40	-30.47
	thG:thC	-23.99	-26.25	-28.40
	thG:C	-23.58	-25.93	-27.82
	G:thC	-26.56	-28.98	-31.31
	^{x}G:^{x}C	-24.64	-26.94	-29.03
	^{x}G:C	-24.39	-26.77	-28.55
	G:^{x}C	-26.32	-28.70	-30.94
ΔE_{stab}+BSSE	A:U	-12.17	-14.46	-15.76
	thA:thU	-12.10	-14.37	-15.77
	thA:U	-12.86	-15.17	-16.62
	A:thU	-11.59	-13.91	-15.10
	^{x}A:^{x}U	-11.89	-14.00	-15.43
	^{x}A:U	-12.35	-14.54	-16.08
	A:^{x}U	-11.80	-14.09	-15.30
	G:C	-24.99	-27.33	-30.47
	thG:thC	-23.01	-24.39	-27.42
	thG:C	-22.62	-24.90	-26.86
	G:thC	-25.56	-27.90	-30.31
	^{x}G:^{x}C	-23.64	-25.86	-28.03
	^{x}G:C	-23.42	-25.79	-27.55
	G:^{x}C	-25.33	-27.62	-29.95
ΔE_{stab}+BSSE+ZPE	A:U	-10.91	-13.50	-14.60
	thA:thU	-11.24	-13.53	-14.60
	thA:U	-11.95	-14.39	-15.49
	A:thU	-10.38	-13.00	-14.25
	^{x}A:^{x}U	-11.22	-13.49	-14.79
	^{x}A:U	-11.53	-13.75	-15.27
	A:^{x}U	-10.59	-13.22	-14.32
	G:C	-23.38	-26.11	-28.87
	thG:thC	-21.60	-23.30	-25.77
	thG:C	-21.11	-23.38	-25.35
	G:thC	-24.01	-27.12	-28.60
	^{x}G:^{x}C	-22.43	-25.24	-26.15
	^{x}G:C	-21.91	-24.59	-26.07
	G:^{x}C	-23.96	-26.85	-28.46

are shown in Fig. 2.4 and their stabilization energy due to the WC base pairs formation are provided in Table 2.1. This stability energy is well comparable with the stabilization energy due to WC base pair formation of natural nucleobases. These results suggest the WC base pairing between the thieno-nucleosides and size-expanded nucleosides with their natural complementary nucleosides.

2.3.2 Optical Absorption and Emission

The optical properties of thieno and size-expanded nucleosides are calculated using TDDFT formalism both in gas phase and in the presence of implicit solvent (water). The calculated absorption and emission spectra are shown in Fig. 2.5. Absorption spectra are calculated using the optimized geometry in ground state (S_0) and the emission spectra are calculated using the optimized geometry in first excited state (S_1). We have observed the lowest energy absorption peaks at 345.09 nm, 304.47 nm, 338.92 nm, and 322.22 nm for thA, thU, thG, and thC, respectively, in water. These peaks are also in good agreement with the experimentally observed absorption peaks at 341 nm, 304 nm, 321 nm, and 320 nm for thA, thU, thG, and thC, respectively, in aqueous solvent. [29] For size-expanded nucleosides, we find the lowest energy absorption peaks at 327.45 nm, 297.95 nm, 327.80 nm, and 311.21 nm for ^{x}A, ^{x}U, ^{x}G, and ^{x}C, respectively, in water. These peaks are in good agreement with the experimentally observed absorption peaks at 331 nm, 311 nm, 326 nm, and 322 nm for ^{x}A, ^{x}U, ^{x}G, and ^{x}C, respectively. [30] It is worthy to note that the natural RNA nucleosides show the lowest energy absorption peaks

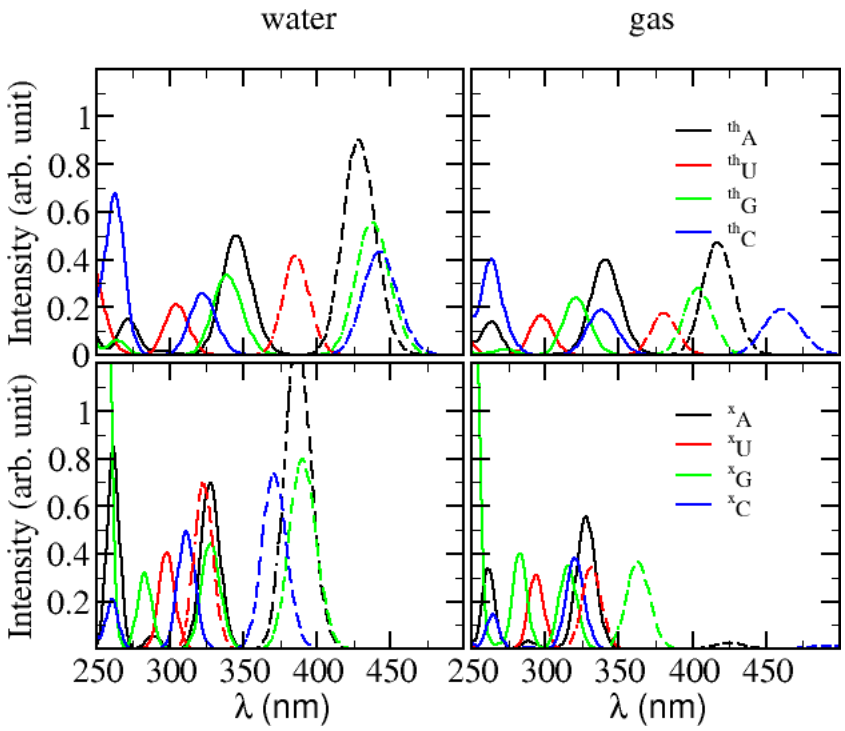

Figure 2.5: Calculated absorption (solid line) and emission (dash line) spectra of modified A (black), modified U (red), modified G (green) and modified C (blue) in both water solvent (left) and gas phase (right).

below 300 nm. The lowest energy excitations and corresponding oscillator strength for all the systems considered in our study are given in the Table 2.2. The calculated absorption spectra in water follow the same qualitative trend as found in experiment. This shows the important role of solvent in these studies.

We have analyzed the relevant frontier molecular orbitals (FMOs) of the thieno and size-expanded nucleosides to understand the origin of the lowest energy absorption peak. The highest occupied molecular orbital (HOMO) and lowest unoccupied molecular orbital (LUMO) are shown in the Fig. 2.6.

Table 2.2: HOMO-LUMO gap (ΔE_{HL}) and lowest excitation energies and corresponding Oscillator Strengths (Os. Str.) of the thieno-nucleosides and size-expanded nucleosides. Experimentally the excitation energies are reported for thieno-nucleosides in water and for size-expanded nucleosides in methanol solvent.

Systems	Gas (water) phase	Excitation Energy and Os. Str.				
	ΔE_{HL}	Calculated				Expt.
		gas		water		
	eV	eV	Os. Str.	eV	Os. Str.	eV
thA	3.99 (4.02)	3.64	0.160	3.59	0.200	3.64
thU	4.71 (4.64)	4.17	0.066	4.07	0.085	4.08
thG	4.35 (4.17)	3.86	0.096	3.66	0.134	3.86
thC	4.17 (4.40)	3.66	0.075	3.85	0.103	3.87
^{x}A	4.17 (4.22)	3.78	0.156	3.79	0.195	3.75
^{x}U	4.86 (4.81)	4.22	0.087	4.16	0.114	3.99
^{x}G	4.43 (4.30)	3.93	0.098	3.78	0.124	3.80
^{x}C	4.48 (4.61)	3.87	0.106	3.98	0.139	3.85

For both the cases, HOMOs and LUMOs are mainly localized on the nucleobase part of the nucleosides. In case of natural nucleosides, LUMOs are the π-orbitals while HOMOs have σ-character for the pyrimidines. [137, 146] Whereas, in the case of thieno-nucleosides and size-expanded nucleosides, the HOMOs and LUMOs are made up of the π-orbitals. Lowest energy (highest wavelength, λ_{max}) transitions for thieno nucleosides and size-expanded nucleosides correspond to the HOMO-LUMO transitions (π-π^*). Our calculated HOMO-LUMO energy gaps for size-expanded nucleobases have the same trend as those from different level DFT calculations in gas phase. [119, 147] The computed HOMO-LUMO energy gap decreases in presence of water and hence, the λ_{max} is higher in water compared to the same in gas phase.

Emission spectra was calculated for all the modified nucleosides and compared with the experimentally observed emission spectra (see Table 2.3). We

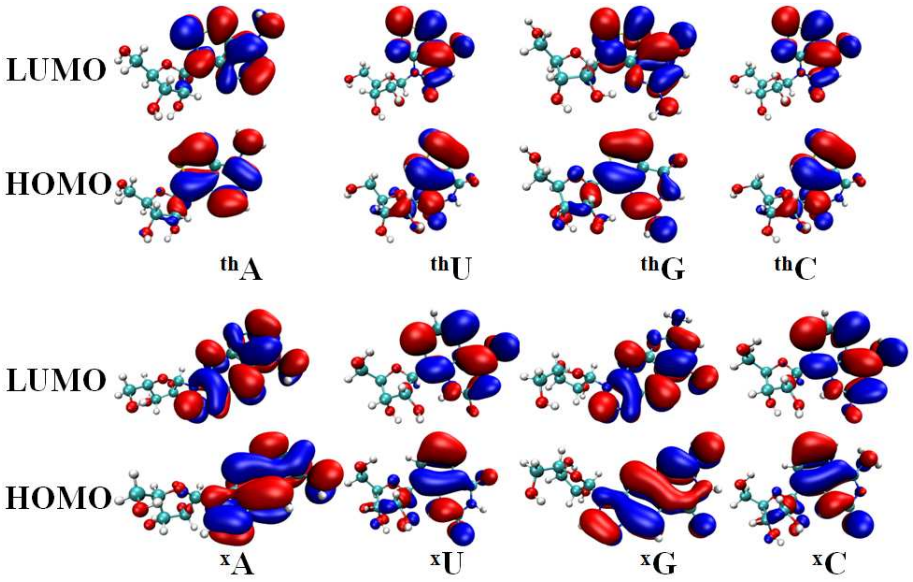

Figure 2.6: Calculated highest occupied molecular orbital (HOMO) and lowest unoccupied molecular orbital (LUMO) of thieno-nucleosides and size-expanded nucleosides (in water).

have found the emission peaks at 428.49 nm, 385.73 nm, 437.73 nm, and 442.75 nm for thA, thU, thG, and thC, respectively, in water. Our calculated emission peaks for thieno-nucleosides compare quantitatively with the previously theoretically [148] reported values and are in good agreement with the experimentally [29] observed emission peaks at 420 nm, 409 nm, 453 nm, and 429 nm for thA, thU, thG, and thC, respectively, in aqueous solvent. The out-of-plane deformation of six-membered ring in case of natural nucleosides plays the important role for the ultrafast internal conversion of photoexcited nucleobases and the additional ring eliminates the femtosecond internal conversion of the nucleobases. [130] Therefore, it is expected that the size-expanded nucleobases will show the emission properties. We find the emission peaks at 386.88 nm, 322.86 nm, 390.17 nm, and 370.91 nm for

Table 2.3: Emission peaks of the thieno-nucleosides and size-expanded nucleosides.

Nucleoside	Calculated				Experiment
	gas		water		
	eV	Os. Str.	eV	Os. Str.	eV
thA	2.97	0.132	2.89	0.254	2.95
thU	3.26	0.049	3.21	0.116	3.03
thG	3.07	0.079	2.83	0.156	2.74
thC	2.69	0.053	2.80	0.121	2.89
^{x}A	2.92	0.007	3.20	0.365	3.32
^{x}U	3.74	0.096	3.84	0.197	3.36
^{x}G	3.42	0.103	3.12	0.224	3.02
^{x}C	2.52	0.004	3.34	0.216	3.27

^{x}A, ^{x}U, ^{x}G, and ^{x}C, respectively, in water. These peaks are in good agreement with the experimentally observed absorption peaks at 373 nm, 369 nm, 411 nm, and 379 nm for ^{x}A, ^{x}U, ^{x}G, and ^{x}C, respectively. [30] It is worthy to note that the natural RNA nucleosides are fluorescence inactive because of excited states of the nucleobases return nonradiatively to the ground state (S_0). [149] The emission energy and the corresponding oscillator strength for all the systems considered here are given in the Table 2.3.

Additionally, we have calculated the infrared spectra for all the WC base pairs of natural and for both the modified nucleobases. We have mainly focussed on the stretching frequency of the N-H bonds involved in the WC H-bonds formations between complementary nucleobase pairs. The calculated N-H bond stretching frequency values are given in the Table 2.4. For the case of A:U pair, the N-H bond stretching frequencies are in the range of 3400 $\pm$ 50 cm^{-1} and 2950 $\pm$ 50 cm^{-1} for N-H$\cdots$O and N-H$\cdots$N H-bonds, respectively for all the nucleobases. Whereas, for the case of G:C pair, the

Table 2.4: Calculated Normal Mode Vibrational Frequencies (in cm^{-1}) for N-H Bond Stretching Directly Involved in Watson-Crick Base Pairing.

Systems	N-H$\cdots$O	N-H$\cdots$N	O$\cdots$H-N
A:U	3404.30	2970.89	-
thA:thU	3386.81	2943.77	-
thA:U	3355.18	2949.43	-
A:thU	3433.84	2983.64	-
^{x}A:^{x}U	3404.77	2945.18	-
^{x}A:U	3377.23	2953.35	-
A:^{x}U	3429.13	2970.35	-
G:C	3390.73	3219.35	3150.57
thG:thC	3423.15	3236.82	3165.29
thG:C	3424.80	3246.33	3246.33
G:thC	3390.14	3221.76	3083.75
^{x}G:^{x}C	3418.54	3216.65	3216.65
^{x}G:C	3419.75	3221.83	3221.83
G:^{x}C	3389.69	3218.62	3105.80

N-H stretching frequencies are in the range of 3400 $\pm$ 50 cm^{-1}, 3225 $\pm$ 25 cm^{-1} and 3150 $\pm$ 150 cm^{-1} for N-H$\cdots$O, N-H$\cdots$N and O$\cdots$H-N H-bonds, respectively for all the nucleobases. Our calculated N-H bond stretching frequency values of WC pairs of natural nucleobases compares fairly well with experimental results and a few earlier studies. [115, 150, 151] We have found that the changes in N-H stretching frequencies are consistent with the changes in bond lengths due to the formation of WC H-bonds.

2.4 Conclusions

In summary, we have shown that the thieno-nucleobase and size-expanded nucleobases form similar H-bonded WC base pair as found for natural nucleobases using various levels of DFT calculations. We have found the similar

structural and bonding pattern and comparable H-bonding stability energy among various WC base pairs in case of natural as well as in both the modified nucleobases. Also, we have shown that both thieno-nucleobases and size-expanded nucleobases can form WC base pair with their natural complementary nucleobases. Thieno-nucleosides and size-expanded nucleosides absorb light at lower energy (> 300 nm) corresponding to the π-π^* transition in comparison to their natural analogues. Natural nucleosides do not show fluorescence emission whereas both thieno-nucleosides and size-expanded nucleosides show fluorescence emission in UV-visible region. The lowest energy absorption and emission peak values follow the same trend with the HOMO-LUMO gaps. The calculated absorption spectra in water follow the same trend as found experimentally. This results show the important role of solvent in these systems. Therefore, we believe that our results have demonstrated the various aspects of WC base pairs formed by the natural, thieno and size-expanded nucleobases present in RNA and have provided a microscopic understanding of the experimentally observed optical properties of the thieno and size-expanded nucleosides, together with the natural nucleosides.

Chapter 3

Structural, Electronic and Optical Properties of Metallo Base Pairs in Duplex DNA*

3.1 Introduction

Deoxyribonucleic acid (DNA) is considered as the blue print of life as it relates to the long-term storage of hereditary information by arranging thousands of bases in a unique sequencing manner in almost all living organism (animals, plants, fungi, bacteria etc.). [152–154] The hydrogen-bond (H-bond) mediated Watson-Crick (WC) complementary base pairing; *i.e.*, A:T (two H-bonds) and G:C (three H-bonds) and π-π stacking interactions, phosphate

*Work reported in this chapter is published in: P. K. Samanta, A. K. Manna, and S. K. Pati, Chem. Asian J. **7**, 2718-2728 (2012). Reproduced with permission from John Wiley and Sons.

and sugar as its backbone together with water at its surroundings are believed to be responsible for the overall stability of any duplex DNA present in our biological systems. [155, 156] Moreover, artificial base pairs and metal modified base pairs can be inserted into the duplex DNA in order to enhance the structural stability and to have exotic functionality for technological applications. [157,158] Various synthetic strategies for artificial DNA have been established and developed since last few decades. [159] Currently, an automated DNA synthesizer can routinely make oligomers in the order of 100 nucleotides possessing pre-designed base sequences. Automated DNA synthesizers are useful not only for the natural nucleotides, but also for the artificial building blocks. [5] When the H-bonded WC base pairs are replaced by metal-ligand interactions inside the DNA duplex, it is termed as metal-mediated base pairs. Certain metal ions can be coordinated either by a pair of hetero-atom present in natural nucleobases or by specially designed ligands which are placed opposite to each other to form a natural or artificial base pair in a DNA duplex. [31] The incorporation of transition metals in DNA duplex can be used to create molecules that have potential applications in nanotechnology and molecular electronics. [160–162] A synthetic strategy was first proposed by Tanaka and Shinoya in 1999, involving the replacement of the natural nucleobases by ligands those have a higher affinity for metal ions than the natural nucleobases. [163] Given that the ligands are aromatic and the geometry of the metal-ligand complex is planar, the complexes can participate in π-stacking interaction within adjacent artificial nucleobase pairs. This strategy allows the incorporation of metal ions at specific positions in a nucleic acid duplex [5, 31, 160], as well as the creation of arrays of metal ions

within a duplex [32, 33, 164–166], triplex [166–168] and tetraplex [169, 170] DNA. Note that, DNA triplex and tetraplex structures are stabilized by both the standard WC and Hoogsteen hydrogen bonding interactions. These results suggest that artificial metallo-DNA is one of the most powerful ways to assemble metal ions in a programmable manner, especially for metal complexes with square-planar or linear coordination geometries, in accordance with their constitutional similarity to natural base pairs. Experimentally, the incorporation of metal ions into DNA duplex architecture has been recently achieved by two different ways: (a) replacement of the imino proton with divalent metal ions [111,171,172] and (b) incorporation of metal ion *via* a metallo-ligand base pair [32,33,165,167,173–175].

Numerous ligands have been introduced into DNA, RNA, LNA, PNA and GNA oligomers and a variety of metal ions have been put into the ligand-modified duplexes formed by these oligomers. [5, 31, 160, 176–180] Circular dichroism (CD) studies predict that the metals modified DNA retains the structure of B-DNA (the most common structural form of duplex DNA in living organisms, in which the double helix twists in a right-helical direction) and is stable compared to the unmodified DNA. [165, 174] This is useful to transform DNA into a conductive material that would make a significant contribution to the development of the vibrant field of DNA-based molecular electronics. [181–187] Conductivity measurements, comparing the conduction properties of the dry B-DNA and Zn^{2+} incorporated DNA (Zn^{2+}-DNA), show that B-DNA is semiconducting whereas Zn^{2+}-DNA is conducting. [188] The combination of DNA and functional metals can introduce significant advantage from both the metals and the DNA structure points of view, thus

representing an important step for their potential applications in various devices [183–185, 189], nanomagnets [163, 190], molecular spintronics [165, 190], information processing [191] or as catalysts in a chemical reaction [192, 193]. With the rapid experimental progress in synthesizing various metal-DNA (M-DNA) complex and their growing importance in DNA-based molecular electronics, it is worth to unambiguously characterize the electrical properties of these complexes. Brancolini *et al.* have reported the enhancement of π-stacking interaction and induction of metallic conductivity in case of M-DNA complex using density functional theory (DFT). [109, 112, 194, 195] Theoretical studies have been able to explain the formation of magnetic array of metal ions within a DNA scaffold [123] and some of the M-DNA have also been predicted to be half-metallic [196].

In this chapter, we have presented first-principles DFT calculation on metallo-DNA complex consisting of metal mediated base pairs modified duplex DNA. It is noteworthy to mention that the present DNA model is based on the experimental work by Johannsen *et al.* [197], where three consecutive Ag^+-mediated Im base pairs (Im-Ag^+-Im) are present inside a poly (A:T) double helix (Ag^+-DNA, see in Fig. 3.1). Experimental study considers a self-complementary sequence with three consecutive artificial imidazole nucleobase (Im) in the centre of the single DNA strand. This helps DNA to adopt the hairpin shaped duplex structure which transforms to a stable DNA duplex in presence of Ag^+ ions. We study the role of metal ions (diamagnetic Ag^+ and magnetic Cu^{2+}) in stabilizing these duplex DNA complexes. We also focus on the role of the counter ions (Na^+) and coordinated water molecules on the stability of this duplex form of M-DNA. Furthermore, we

analyze the electronic structure and optical properties in details to understand the low-energy properties of these M-DNA complexes.

3.2 Computational Methods

We used first-principles DFT calculations as implemented in Gaussian 09 suite of programs [72] for the geometry optimization as well as for the single point energy calculations for nucleobases and base pairs including metal mediated base pairs. Time dependent DFT (TD-DFT) was used to calculate the absorption properties for the metal mediated imidazole base pair, Im-M-Im. We employed hybrid B3LYP [64, 131, 132] exchange and correlation energy functional and 6-31+g(d, p) basis sets for all the atoms except for Ag and Cu atoms, for which LANL2DZ basis set [198–200] was used. We also have done the calculation with higher basis set (MWB28 [201]) for Ag atom for verifying the dependency of binding strength on the basis set size. After each geometry optimization, frequency calculations were performed to ensure the energy minimum structures. The natural population analysis (NPA) [202] was used for population analysis of charges. The convergence criterion of SCF is set to 'Tight' and the 'Ultra-Fine' grid was used for numerical integration in DFT calculation as implemented in Gaussian 09. Additionally, DFT package SIESTA [75] was utilized for the calculations of large systems of M-DNA complexes. Note that, all the M-DNA complexes contain more than 450 number of atoms, which were studied using pseudopotential based DFT approach, as available in SIESTA code. Troullier-Martins norm-conserving pseudopotentials in Kleinman-Bylander (KB) form have been used together

with Perdew, Burke, and Ernzerhof (PBE) exchange-correlation energy functional within Generalized Gradient Approximation (GGA). [60] A double-ζ basis set with the polarization (DZP) [203] was included for all atoms together with a real-space mesh cut-off of 300 Ry. All calculations had been performed in a $40\mathring{A} \times 50\mathring{A} \times 40\mathring{A}$ super cells, which was large enough for interactions between the neighboring fragments to be negligible. Atomic relaxations in all of the calculations were performed until the forces on the atoms were not larger than 0.04 eV $\mathring{A}^{-1}$. The reliability of DFT method employed in this study has already been tested for similar kind of systems. [196, 204–207]

We considered a duplex DNA (M-DNA) fragment consisting of seven base pairs, where the central three base pairings occur *via* Ag^{+}/Cu^{2+} (Im-Ag^{+}/Cu^{2+}-Im) along with the four terminal A:T WC base pairs (See Fig. 3.1). The initial structures are constructed from the Protein Data Bank [208] (PDB ID: 2K68 and 2KE8). In order to neutralize the negatively charged DNA phosphate backbone, we follow two different strategies: (i) protonating phosphate groups (H-passivation) [209–216] and (ii) adding sodium (Na^{+}) counter ion, equidistant ($\sim 2.2\mathring{A}$) from two phosphate oxygens [217–220] and compare the results.

3.3 Results and Discussion

3.3.1 Structure and Stability

From the experimental observation, it was found that Im modified DNA oligonucleotide form stable hairpin structure (PDB ID: 2K68) in absence of

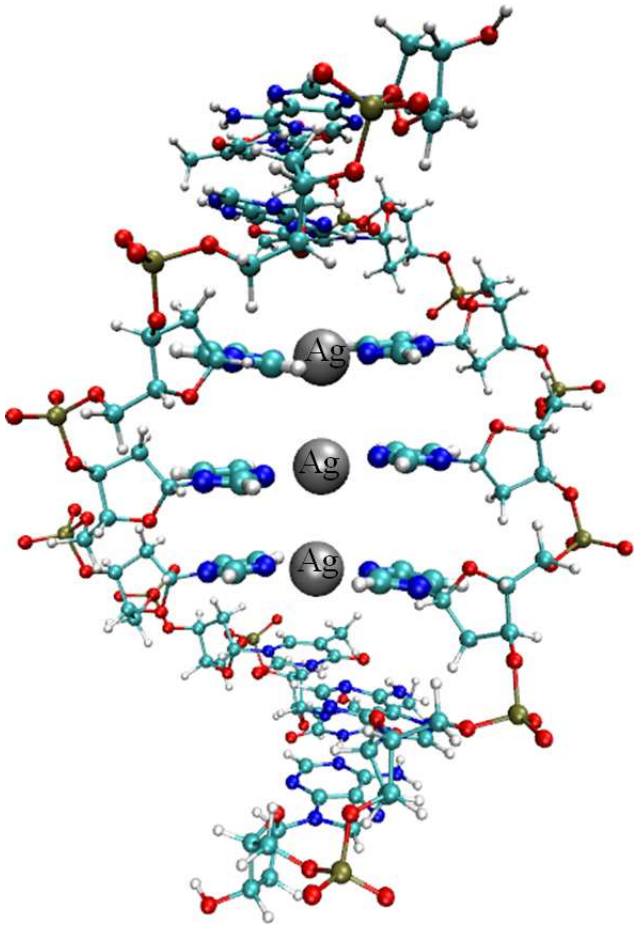

Figure 3.1: Duplex structure of Im-Ag^{+}-Im modified DNA (Ag^{+}-DNA).

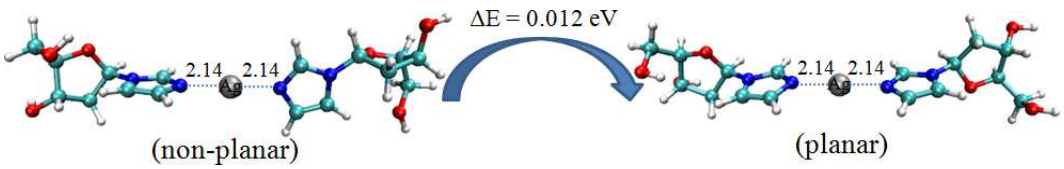

Figure 3.2: Optimized structure of non-planar and planar Im-Ag^{+}-Im unit. Important bond distances (N-Ag) are written in unit of $\mathring{A}$.

Ag^+ ions, which is stabilized through strong $A:T$ WC hydrogen bonding (H-bonding) and π-π stacking interactions in between adjacent base pairs. Additions of Ag^+ ions make the system stabilized in duplex form (PDB ID: 2KE8). It clearly proves that the Ag^+ ion has significant role in stabilizing the duplex structure. Before we discuss the structural stability, electronic structure and optical properties in details for Im-Ag^+-Im modified duplex DNA (Ag^+-DNA), initially here we look at the structural stability of the Ag^+ linked Im-base pairs, *i.e.*, only Im-Ag^+-Im unit. The optimized structures of Im-Ag^+-Im are shown in Fig. 3.2. It is clear from the Fig. 3.2 that the Ag^+ ion is flanked between two Im units *via* N atoms. The equilibrium distance between the Ag^+ and N atom of Im-base is $\sim 2.14\mathring{A}$ in both the planar and non-planar structures. The dihedral angle of $\sim 85^\circ$ between two Im planes for the non-planar geometry results in $\sim$0.277 kcal mol^{-1} extra stability compared to the planar form of Im-Ag^+-Im. Thermal and molecular vibrations can overcome this low-energy barrier to achieve the planar structure. The planar form of Im-Ag^+-Im base pair may also be achieved through $\pi-\pi$ stacking interactions between the adjacent base stacks in a modified duplex DNA. Moreover, in both cases, the effective positive charge on the Ag atom is 0.7 e which indicates 0.3 e charge (electron) transfer from Im bases to the Ag^+. The extent of charge transfer clearly indicates the electrostatic interactions between Ag^+ and Im bases. The charge transfer also induces local redistribution of charges in Im moieties, causing induced dipole-dipole interactions. In order to explain the stability of metal mediated Im base-pairs, we calculate the binding energy of Im-Ag^+-Im complex. The

binding energy (E_b) is defined as,

$$E_b = E_{[Im-Ag^+-Im]} - \left[2E_{[Im]} + E_{[Ag^+]}\right] \tag{3.1}$$

where, $E_{[Im-Ag^+-Im]}$, $E_{[Im]}$ and $E_{[Ag^+]}$ are the total optimized energies of Im-Ag^+-Im, imidazole(Im) and Ag^+, respectively. The calculated binding energy of -99.14 kcal mol^{-1} (-98.68 kcal mol^{-1}) for planar (non-planar) Im-Ag^+-Im explains their stability. Note that, although both planar and non-planar structures of Im-Ag^+-Im unit have comparable binding energy values, non-planar structure is slightly more stable. We have found slightly larger binding strength (lower binding energy, -106.32 kcal mol^{-1}) with MWB28 basis set than the values calculated using LANL2DZ basis sets (-99.14 kcal mol^{-1}).

To estimate the stability of the Im-Ag^+-Im modified duplex DNA complex (Ag^+-DNA, Fig. 3.1), we have calculated binding energy ($E_b{}^c$) using the following equation:

$$E_b{}^c = \frac{1}{3}\left[E_{[Ag^+-DNA]} - 2E_{[DNA_hp]} - 3E_{[Ag^+]}\right] \tag{3.2}$$

where, $E_{[Ag^+-DNA]}$ and $E_{[DNA_hp]}$ are the energies of Ag^+-DNA, DNA-hairpin, respectively. The superscript 'c' is used to differentiate the binding/displacement energy of M-DNA complexes from the corresponding values for Im-M-Im base-pairs. Note that, higher the negative binding energy, greater is the stabilization. All the energies are provided in Table 3.1. From the calculated binding energy values, we have found that the complex is more stable in

presence of Na^+ counter ions in comparison to the results obtained for the H-passivated phosphate groups. The difference in E_b between these two cases is only $\sim$18.68 kcal mol^{-1} per Ag^+, indicating the strong structural stability of Ag^+-DNA complexes irrespective of the nature of counter ions. We also analyze the effect of water coordination to the Na^+ ions closer to the phosphate groups. For this, we added two explicit water molecules for each Na^+, which fulfil the Na^+ effective coordination number as four [221], and calculate the binding energy. Note that, Na^+ in bulk water shows four coordination numbers if one considers only the first solvation shell [221]. We find that the inclusion of coordinated water molecules has very little effect on the electronic and optical properties. We also focus to calculate the displacement energy ($E_d{}^c$) for Ag^+-DNA complex which is defined as follows:

$$E_d{}^c = \frac{1}{3}\left[E_{[Ag^+-DNA]} - E_{[DNA]} - 3E_{[Ag^+]}\right] \tag{3.3}$$

where, $E_{[Ag^+-DNA]}$ and $E_{[DNA]}$ are the total energy of Ag^+-DNA and DNA scaffold without chelating Ag^+ ions, respectively. Negative of displacement energy is the energy required to remove the metal ions from the DNA scaffold. We find similar trends in E_d values as obtained for the calculated binding energies. Furthermore, to understand the effect of water solvation on the structural stability, we also calculate the $E_b{}^c$ and $E_d{}^c$ in presence of explicit water molecules. We only relax the position of Na^+ ions and coordinated water molecules in this complex to find the energetics. As given in Table 3.1, although we find very similar $E_b{}^c$ and $E_d{}^c$ values, $E_b{}^c$ is significantly increased

(almost double the values obtained without water) because of the water coordination. The increase in $E_d{}^c$ can be accounted for the contribution of the Na^+ ion solvation energy to the calculated total binding energy.

However, it is to be noted that for both the energetics calculations (binding and displacement energies), we have only considered the bare Ag^+ ions. But, for a practical situation in solution phase calculations, the Ag^+ ions are scarcely to be present as bare free ions. Instead, the Ag^+ ions are more likely to be solvated by the solvent molecules; in present case, by the water molecules. Consequently, in order to form the Ag^+-DNA complex, one has to overcome the relevant solvation energy associated with the Ag^+ ions. Thus, we consider calculating the solvation energy of Ag^+ in bulk water. For this, we have considered 32 water molecules and one Ag^+ ion within a cubic box of 10 $\mathring{A}$ dimensions for the DFT calculations. The initial geometrical configurations of whole systems is modelled using genbox utility in GROMACS molecular dynamics package [97]. We have performed a variable cell geometry optimization and calculated the solvation energy using the methods as discussed above. The solvation energy is found to be -135.83 kcal mol^{-1} for Ag^+ immersed in water, which agrees well with the results reported by Leung *et al.* [222]. Also, note that, the bulk water density for the ion free model system is calculated to be 1.22 g cc^{-1} which slightly greater than the room temperature bulk water density. However, the addition of Ag^+ ion slightly increases the water density from 1.22 g cc^{-1} to 1.23 g cc^{-1}, which is negligibly small to be considered for the present energetics study.

We also calculate the amount of charge transfer from Im to the Ag^+ in Ag^+-DNA complex under different phosphate environments as discussed

above. We find that the amount of average charge (electrons) transfer from Im to Ag^+ is $\sim$0.80 e, which essentially reduces the effective positive charge on Ag^+ ions from 1.0 e to 0.2 e. This clearly indicates the importance of electrostatic interactions on the stabilization of the Ag^+-DNA complex. Also, note that, the average distance of separation between two consecutive Ag^+ ions present in modified DNA is 3.94 $\mathring{A}$, whereas the usual inter-planar separation between two consecutive base-pairs is reported to be $\sim$3.40$\mathring{A}$ [223]. Therefore, we conclude that the increased helical rise is due to the larger electrostatic repulsion between the Ag^+ ions which dominates over the interactions arising from the small size of the Im moiety compared to the natural nucleobase pair, AT, present in the modified duplex DNA as reported in the experimental work by Johannsen *et al.* [197]. To understand the distribution of the transferred charges over the associated Im ligands, we consider calculating the difference in charge density for Ag^+-DNA complex under different phosphate neutralization conditions. The charge density difference ($\Delta\rho$) is defined as,

$$\Delta\rho = \rho_{[Ag^+-DNA]} - \left[\rho_{[DNA]} - \rho_{[3Ag^+]}\right] \tag{3.4}$$

where, $\rho_{[Ag^+-DNA]}$, $\rho_{[DNA]}$ and $\rho_{[3Ag^+]}$ are the charge density of Ag^+-DNA, modified DNA without the Ag^+ and three bare Ag^+, respectively. We plot the difference in charge density in Fig. 3.3. We find that the electron transfer occurs mainly from Im ligand to positively charged Ag^+ ions.

To compare and contrast the structural stability of Ag^+-DNA complex

Table 3.1: The binding energy ($E_b{}^c$) and displacement energy ($E_d{}^c$) per Ag and average electron transfer (ET) from imidazole to Ag^+. *-Ve* sign indicates electron transfer from Ag to the ligand. Basis set superposition corrected displacement energies are given within bracket.

Systems	$E_b{}^c$ (kcal mol^{-1})	$E_d{}^c$(kcal mol^{-1})	ET (e)
Ag^+-DNA (H passivated)	-176.64	-202.70 (-168.11)	0.80
Ag^+-DNA (Na^+)	-195.32	-235.91 (-192.79)	0.81
Ag^+-DNA (Na^+ + water)	-402.41	-231.30 (-196.25)	0.82
$Ag(0)$-DNA (H passivated)	-70.57	-73.33 (-11.76)	-0.12
$Ag(0)$-DNA (Na^+)	-91.32	-84.17 (-37.82)	-0.14

with that of $Ag(0)$-DNA comprising of neutral Ag, we have considered calculating the $E_b{}^c$ and $E_d{}^c$ values for the later complex as well. We fix the geometry of the $Ag(0)$-DNA complex to that of Ag^+-DNA structure for an energetics comparisons. We find that both the binding and displacement energies are significantly destabilized in comparison to the Ag^+-DNA, highlighting the importance of Ag^+ ions in stabilizing the duplex DNA. We also find a very small amount of electron transfer from Ag to Im bases indicative of less significant electrostatic interactions. However, we have also performed full structural relaxations for the $Ag(0)$-DNA complex for mimicking a realistic situation. We find that neither the Im-$Ag(0)$-Im unit nor the $Ag(0)$-DNA complex is stable *via* Im-$Ag(0)$-Im bonding interactions. During the full geometry optimization, the $Ag(0)$-DNA complex is significantly deformed from its parent Ag^+-DNA structure and instead, all the three consecutive Ag atoms started forming a cluster due to the strong cohesive energy among them. Our results show that Ag^+ is necessary in stabilizing the Im modified duplex DNA, corroborating with the experimental findings.

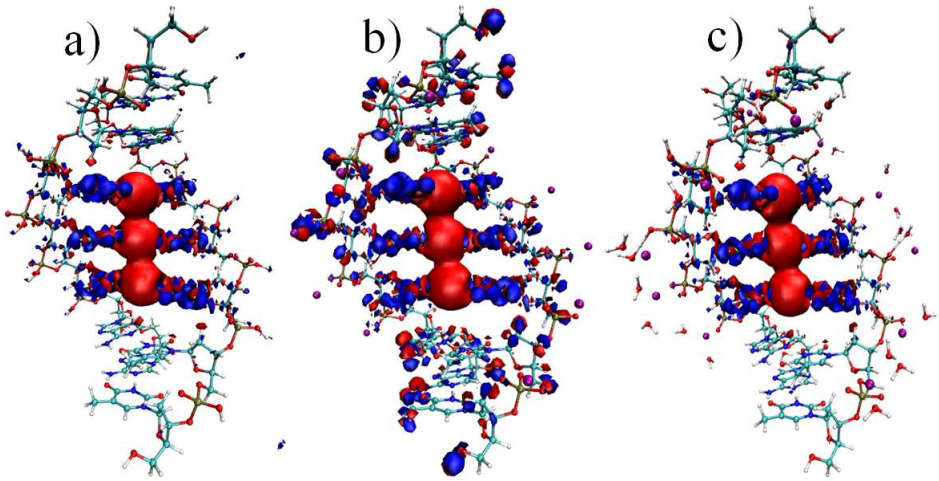

Figure 3.3: Difference in charge density distribution ($\Delta\rho$) plot of (a) hydrogen passivated Ag^+-DNA, (b) Na^+ counter ion added Ag^+-DNA and (c) Na^+ counter ion and water added Ag^+-DNA. The red and blue colors indicate gain and loss in electron density, respectively. The above results show that electron transfer occurs from imidazole base to positively charged silver atoms.

3.3.2 Electronic Structure

Now we focus on the electronic structure of the Ag^+-DNA complexes. In Fig. 3.4, we plot the total electronic density of states (DOS) as well as site projected density of states (pDOS) to better understand the changes in DNA electronic properties in details. As shown in Fig. 3.4, the highest occupied molecular orbital (HOMO) is mainly localized on natural A:T base pair whereas lowest unoccupied molecular orbital (LUMO) is mainly localized on Im bases and slightly on the Ag^+ flanked between two Im bases. We also find that the HOMO-LUMO gap for H-passivated Ag^+-DNA is 0.88 eV whereas the same for Na^+ added Ag^+-DNA is 1.30 eV, which is further increased to 1.43 eV by the presence of explicit water coordination. Note that, in natural duplex B-DNA, the HOMO-LUMO gap value varies from

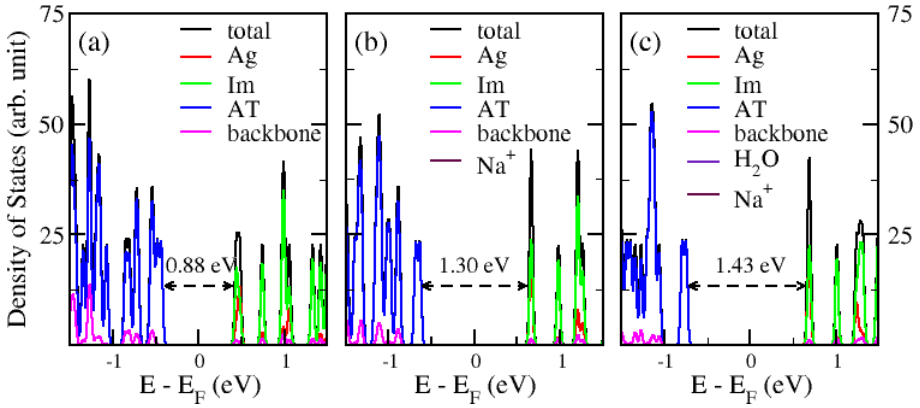

Figure 3.4: Electronic DOS plots of (a) H-passivated Ag^+-DNA, (b) Na^+ counter ion added Ag^+-DNA and (c) Na^+ counter ions and 24 water molecules added Ag^+-DNA.

$\sim$0.5 eV to $\sim$6.0 eV, depending on the nature of base sequences and on the length of DNA. [224, 225] In the present study, we find HOMO-LUMO gap values ranging from 0.88 eV to 1.43 eV obtained for different types of phosphate neutralizations. The increase in HOMO-LUMO gap values in presence of Na^+ and coordinated water than H-passivated Ag^+-DNA is due to the stabilization of HOMO and destabilization of LUMO levels, which are essentially governed by the electrostatic interactions. As can be seen from the Fig. 3.4, the contribution of sugar phosphate backbone, Na^+ ions and coordinated water to the electronic DOS is very small near to Fermi energy (E_F), demonstrating the fact that the low-energy physics does not change much due to the different types of phosphate neutralization and presence of water coordination.

We also analyze the frontier molecular orbital (FMO) of Ag^+-DNA and present them in Fig. 3.5 for three different cases as discussed above. As shown

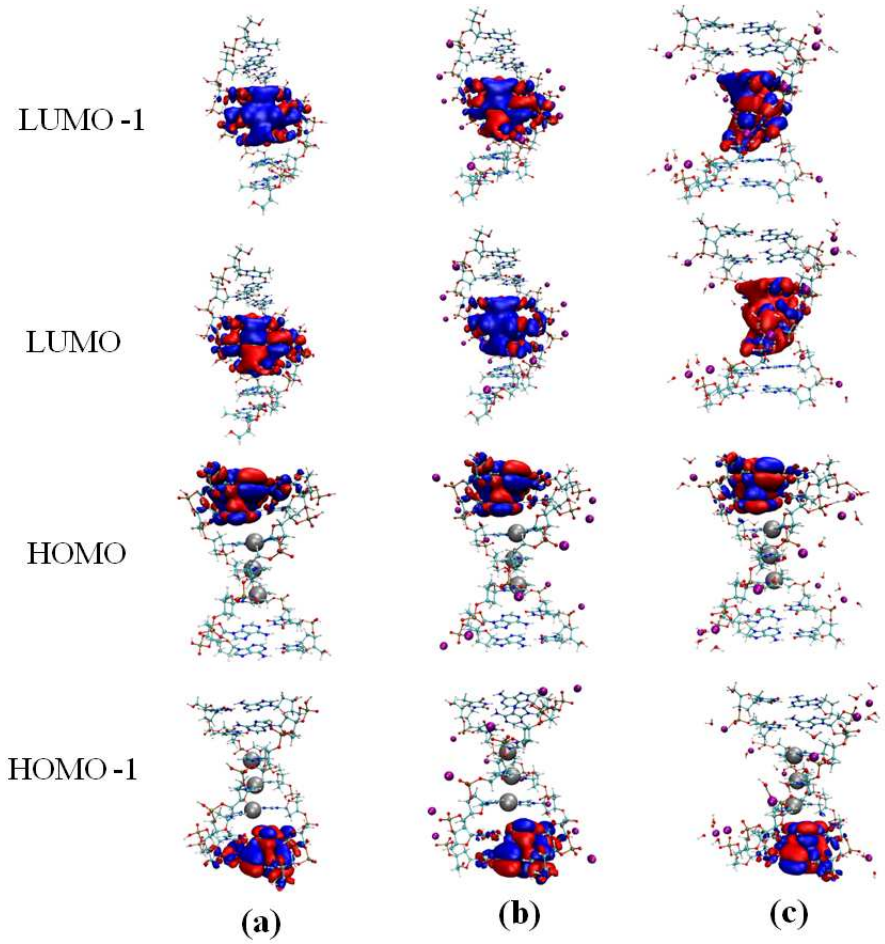

Figure 3.5: Frontier molecular orbital (FMO)diagram of (a) H-passivated to phosphate group, (b) Na^+ counter ions added and (c) Na^+ counter ions and 24 water molecules added to Ag^+-DNA.

in Fig. 3.5, the HOMO-1 and HOMO are primarily localized on the natural A:T nucleobase pairs whereas LUMO and LUMO+1 are mainly localized on imidazole units and coordinated Ag^+ ions between them. Moreover, neither the nature of phosphate neutralization nor the presence of explicit water molecules affect the overall structure of these FMO distributions, again highlighting the negligible effects of different types of phosphate neutralization and presence of water molecules to the changes in electronic structure. However, the complete localization of HOMO-1, HOMO on the A:T base pairs and localization of LUMO, LUMO+1 on Im-Ag^+-Im units indicate that there is a possibility of charge transfer induced optical absorption from occupied to unoccupied molecular orbitals in the low-energy absorption spectrum of modified Ag^+-DNA.

3.3.3 Optical Absorption

To probe whether the metal mediated base pairing can affect the optical properties, we consider calculating the optical absorption of Ag^+-DNA complex. Absorption coefficients are calculated from the imaginary part of dielectric constant. The calculations are performed using the simplest approach based on the dipolar transition matrix element between different Kohn-Sham eigenfunctions of the self-consistent Hamiltonian. [226–228] Recent reports have proved the effectiveness of this method for the optical calculations in larger molecular complexes. [114, 229]

It was shown that the natural duplex DNA shows optical absorption peaks above 3.0 eV because of the nucleobase π-π^* orbital transition. [205]

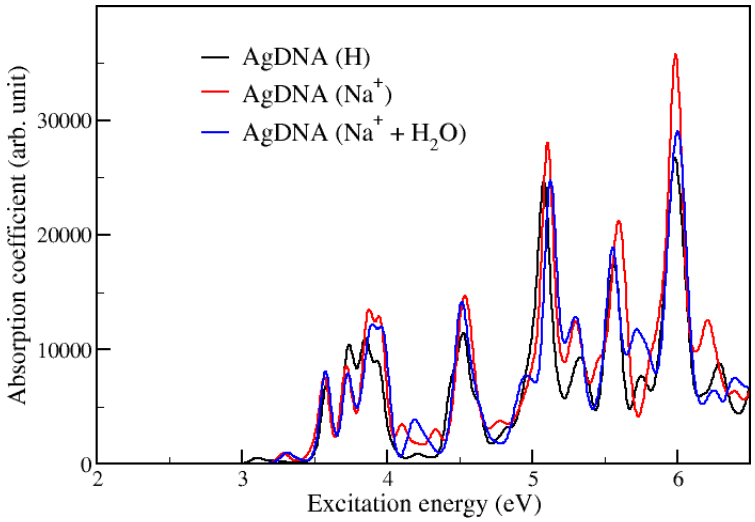

Figure 3.6: Optical absorption for H-passivated to phosphate group, Na^+ counter ions added and Na^+ counter ions and 24 water molecules added to Ag^+-DNA.

In the present study, as shown in Fig. 3.6, we also find low-energy peaks arise only above 3.0 eV in the absorption spectrum of Ag^+-DNA. Moreover, we also find that the nature of phosphate neutralization and the presence of water coordination do not have any significant effect on the overall shape of the calculated optical absorption of the complex. Also note that, the Ag^+-DNA consists of three different types of nucleobases: natural A, T and artificial Im. To understand the origin of optical absorption peaks at low-energy region, we consider analyzing the optical spectrum of three different fragments; *viz.*, (Im-Ag^+-Im), (Im-Ag^+-Im)-($A:T$) and ($A:T$) (see in Fig. 3.7(a)). We calculate the optical absorption using TD-DFT formalism as implemented in Gaussian 09 software code [72]. Our results show that the Im-Ag^+-Im fragment doesn't show any allowed electronic transition below $\sim$5.0 eV whereas, (Im-Ag^+-Im)-($A:T$) and ($A:T$) show optical absorption

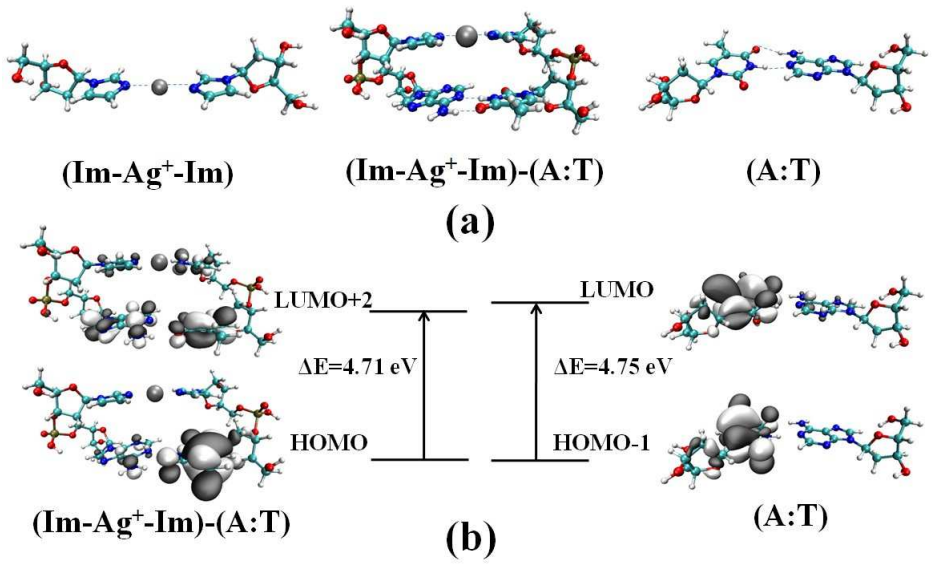

Figure 3.7: (a) Fragments considered for TD-DFT calculation and (b) molecular orbitals plot for the fragment $(Im\text{-}Ag^{+}\text{-}Im)$-$(A:T)$ and $(A:T)$.

at 4.71 eV and 4.75 eV, respectively.

In Fig. 3.7(b), we plot the relevant molecular orbitals (MOs) mainly responsible for the low-energy optical absorption peaks of these fragments. We find that these MOs are primarily localized on the A:T unit of the two fragments considered, reflecting the π-π^* orbital transition solely governing the low-energy absorption. A closer look at the relevant MOs of the fragments considered reveal that the low-energy absorption peaks are due to the π-π^* electronic transitions in T of A:T base pairs. Additionally, from the $pDOS$ analysis, we find that the energy-gap between the occupied and unoccupied MOs localized on A:T is of the order of 3.0 eV which turns out to be the optical gap calculated for the Ag^{+}-DNA complex. This clearly demonstrates that the low-energy optical absorption is mainly governed by the $\pi - \pi^*$ electronic transition in A:T base pairs present in Ag^{+}-DNA, as was found for

the natural B-DNA [205].

Here, we would like to emphasize that in this study, only a few water molecules have been considered near to the Na^+ counter ions which are placed close to the phosphate groups in studying the energetics and opto-electronic properties of Ag^+-DNA complex. In fact, consideration of explicit bulk water extremely increases the computational cost, which is impossible to study within a limited computational resource. We have considered two water molecules adjacent to each Na^+ ion, which fulfil the Na^+ effective co-ordination number as 4: two phosphate oxygen atoms and two oxygen atoms from the two nearby water molecules coordinate to the Na^+ [221]. However, we believe that our model system consisting of a few water molecules have provided the qualitative pictures in understanding the system behaviors in presence of explicit water solvent.

3.3.4 A proposed model system: Im-$Cu(OH)_2$-Im modified duplex DNA (Cu^{2+}-DNA)

So far, we have focused our study on the experimentally synthesized Ag^+-DNA, which is a non-magnetic material because of the fully filled 4d-orbitals of Ag^+ ion, and hence, has limited electronic applications. For the perspective of broad device applications, it is worth to include spin degrees of freedom along with electronic charges for both the electronic and spintronics device integration. Recent studies have also demonstrated the importance of transition metals (Cu, Mn) inclusion within DNA which shows promising half-metallic behaviors for spintronics device applications, and they also

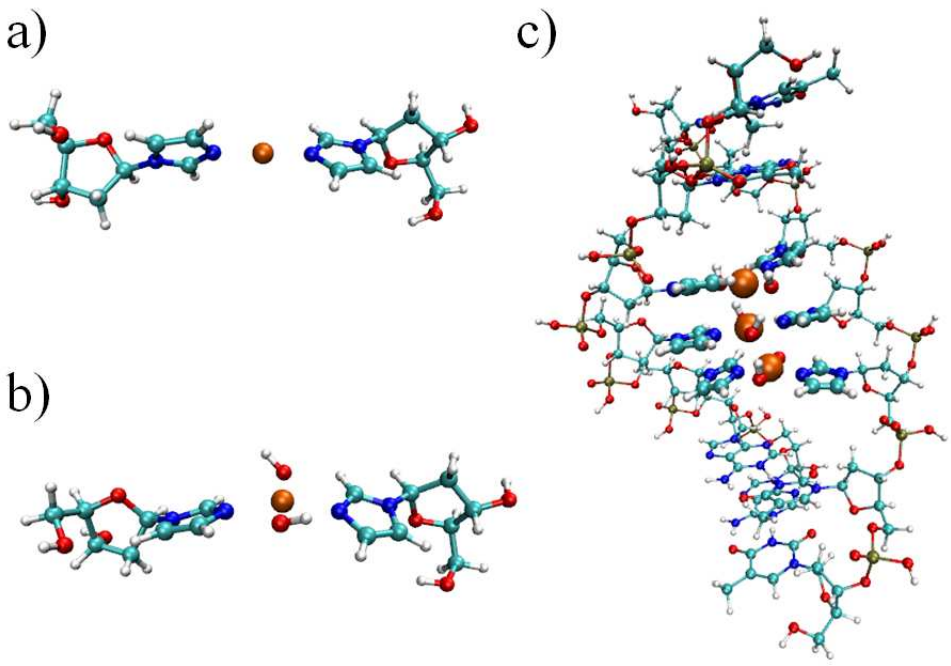

Figure 3.8: Optimized structure of (a) Im-Cu^{2+}-Im, (b) Im-$Cu(OH)_2$-Im and (c) Im-Cu^{2+}-Im modified DNA (Cu^{2+}-DNA).

exhibits low-energy peaks in the calculated optical excitations due to the spin-spin interactions. [123, 230] Herein, we have considered Cu^{2+} ions in place of Ag^{+} ions in Im modified duplex DNA to study the electronic structure. We have also focused on the preferred magnetic interactions and its impact on the changes in optical properties of the Cu^{2+}-DNA.

First, we analyze the structure and stability of Im-Cu^{2+}-Im unit. To compare and contrast the stability of the isolated Im-Cu^{2+}-Im and Im-$Cu(OH)_2$-Im with the Im-Ag^{+}-Im, we considered full structural optimization using B3LYP hybrid exchange and correlation functional with LANL2DZ basis set for Cu and 6-31+g(d, p) basis set for all other atoms employing Gaussian 09 program. The optimized geometry of Im-Cu^{2+}-Im is shown in Fig. 3.8(a). Our results show that the Im-Cu^{2+}-Im unit is highly stable

when compared with the Im-Ag^{+}-Im. As given in Table 3.2, the calculated binding energy of Im-Cu^{2+}-Im is -357.21 kcal mol^{-1} while it is only -98.93 kcal mol^{-1} for Im-Ag^{+}-Im, indicating almost three fold extra stability for the Im-Cu^{2+}-Im complex. This extra stability comes from the greater extent of orbital hybridization and larger extent of charge transfer (ca. 1.36 e) driven electrostatic stabilization because of the presence of the Cu^{2+} ions. The Im-Cu^{2+}-Im unit exhibits 1μ_B magnetic moment which is mainly localized on Cu^{2+} ions. Furthermore, to include the possibility of OH- coordination to the highly positive charged Cu^{2+} in solution, we consider two OH- directly bonded to it, making a four coordinated Cu^{2+} complex. Note that, introduction of two OH- results in charge neutral structure. The fully relaxed geometry of this unit is shown in Fig. 3.8(b). Analysis of the structure and calculated binding energy reveals that the Im-$Cu(OH)_2$-Im form stable complex, and also exhibit 1μ_B magnetic moment (see Table 3.2). Our results show that the stability of this complex is significantly reduced because of the presence of coordinated OH- groups which hinder the extent of charge transfer from Im to Cu^{2+}. We have found relatively smaller electron transfer (0.67 e) from two Im units to Cu^{2+} in Im-$Cu(OH)_2$-Im than the electron transfer (1.36 e) for Im-Cu^{2+}-Im complex, resulting in reduced electrostatic stabilization.

Additionally, we have also considered the formation of an aqua complex, Im-$Cu^{2+}(H_2O)_2$-Im, and have found that this structure is highly stable in comparison to the hydroxide complex, Im-$Cu(OH)_2$-Im. The calculated binding energy for Im-$Cu^{2+}(H_2O)_2$-Im is found to be -396.87 kcal mol^{-1} while the binding energy for the Im-$Cu(OH)_2$-Im complex is only -24.67

kcal mol^{-1}. The larger extent of binding energy for aqua complex is due to the presence of positive charge on the central Cu^{2+} ions, where the charges are completely neutralized in case of hydroxide complex, the Im-$Cu(OH)_2$-Im. Moreover, we find a greater extent of ligand to metal charge transfer for the aqua complex than hydroxide complex. Furthermore, we have also considered the possibility for the existence of this aqua Im-$Cu^{2+}(H_2O)_2$-Im units in the Cu^{2+} modified model duplex DNA under study. We find that the presence of aqua complex enhances the duplex DNA stability through greater electrostatic interactions. The calculated binding energy for the Im-$Cu^{2+}(H_2O)_2$-Im modified duplex DNA is found to be -426.62 kcal mol^{-1}, whereas the binding energy is only -238.91 kcal mol^{-1} for the Im-$Cu(OH)_2$-Im modified DNA duplex (Cu^{2+}-DNA).

Next, we discuss the stability of Cu^{2+}-DNA duplex (see Fig. 3.8(c)). To begin with, we model the initial structure of Cu^{2+}-DNA as the optimized structure of Ag^{+}-DNA (see Fig. 3.1) where all three Ag^{+} ions are replaced by Cu^{2+} ions. We have considered H-passivation to neutralize the sugar-phosphate backbone as was done for the Ag^{+}-DNA complex, and six $OH-$ bonded to Cu^{2+} to make the overall system neutral. We fully relax the geometry using spin-polarized DFT calculations by considering both the ferromagnetic and anti-ferromagnetic spin configurations of the three consecutive magnetic Cu^{2+} ions, each of them possessing one unpaired electron. Similar to the Im-$Cu(OH)_2$-Im base-pairs, previous studies have shown that Cu-mediated hydroxyperidone and salen base-pairs also form duplex DNA [164, 165]. So, here it is important to compare the results obtained for Im-$Cu(OH)_2$-Im base-pairs with the similar base-pairs reported earlier.

The average distance between two consecutive Cu atoms is found to be 2.65 $\mathring{A}$ for the Im-$Cu(OH)_2$-Im modified DNA, Cu^{2+}-DNA. Whereas the average distance between the two Cu atoms are 3.22 $\mathring{A}$ and 3.75 $\mathring{A}$ for DNA containing Cu-mediated hydroxypyridone and salen base pairs, respectively. [123] To compare the energetics among different spin states of three magnetic Cu^{2+} ions present in Im modified DNA, we consider the energetics by making use of the three spins (z-component of the total spin, ${S_z}^t = 1/2$) at Cu^{2+} ions oriented parallel to each other, which we refer to the ferromagnetic arrangements. Contrary to this, we flip the spin of one of the three Cu^{2+} electrons and consider as initial spin configuration fro doublet state (which we refer to as antiferromagnetic arrangements) and calculate energy through DFT calculation using 'broken symmetry' approach, which essentially calculate energy of the doublet state with antisymmetric combinations of the spin flip configurations. Among these, the one with all the three consecutive spin aligned parallely is found to be minimum energy structure. Interestingly we find that the ferromagnetic state is preferred over anti-ferromagnetic state with only a marginal energy difference of 4.80 kcal mol^{-1}. Moreover, in the previous study, it was shown that the two Cu^{2+} ions interact ferromagnetically (anti-ferromagnetically) for the Cu-mediated hydroxypyridone (salen) base-pairs [123]. Interestingly, we also find weak ferromagnetic interactions between the Cu^{2+} ions in Im-$Cu(OH)_2$-Im and Im-$Cu^{2+}(H_2O)_2$-Im modified duplex DNA, as similar to the Cu-mediated hydroxypyridone containing duplex DNA. The high-spin ferromagnetic state is stabilized over low-spin state by only 4.80 kcal mol^{-1} and 0.036 kcal mol^{-1}, for the $-OH$ (hydroxyl)

and H_2O (water) coordination, respectively. Note that, there is oxygen bridging ligands for the stacked Cu^{2+}-hydroxypyridone, which are responsible for the ferromagnetic coupling as explained earlier [123]. To understand the origin of the ferromagnetic interactions, we analyze frontier molecular orbital (FMO) for these modified DNA systems considered in the present study. We find that singly occupied molecular orbitals, namely, SOMO and SOMO-1 (See Fig. 3.11) are mainly localized over Cu atoms and the main component of SOMO and SOMO-1 is found to be Cu $3dx^2$-y^2 orbitals, causing the ferromagnetic interactions. Moreover, in our model systems, there is oxygen bridging, which comes from the hydroxyl/water ($-OH/H_2O$) ligand attached to each Cu^{2+}. These bridging oxygen atoms are responsible for the observed ferromagnetic interactions among the magnetic centers. The calculated binding energy predict that the Cu^{2+} modified DNA is slightly more stable compared to Ag^+-DNA complex which may be due to the presence of greater electrostatic interactions and larger extent of orbital hybridization because of the presence of 3d transition metal, Cu orbitals. However, note that, this comparison is drawn based on the gas-phase DFT calculations, and we have not considered the explicit solvation effects of individual ions present in bulk water, which may differ depending on the nature of the ions. To address this, additionally, as discussed for the case of Ag^+ modified duplex DNA, we have also considered estimating the solvation energy for the Cu^{2+} in bulk water. The calculated solvation energy is found to be -518.40 kcal mol^{-1}, which compare fairly well with the previously reported results [231]. However, it is worth mentioning that the solvation energy calculated for Cu^{2+} is about 4 times lower than that obtained for the Ag^+ in

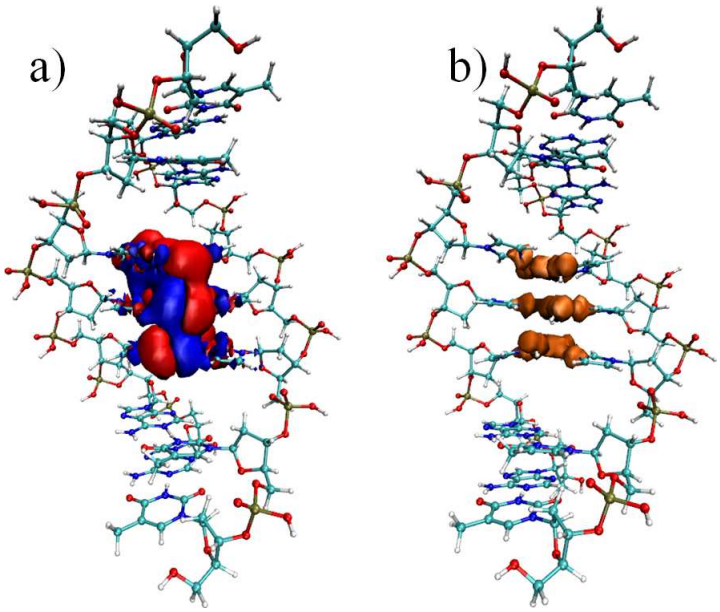

Figure 3.9: Difference in (a) charge density distribution and (b) spin density diagrams. The plots are shown using VMD visual tool with isovalue 0.01.

bulk water. Hence, although the gas-phase DFT calculations predict slightly larger stability for the Cu^{2+}-DNA complex than the Ag^{+}-DNA, the stability order would change when considering explicitly the solvation effects.

As given in Table 3.2, we find a significant amount of electron (1.55 e) transferred to Cu^{2+} from the associated ligands. Detailed population analysis shows that the Im moiety only contributes 0.79 e towards total transferred charge and a major contribution comes from the ligated $OH-$ groups. Interestingly, we find almost similar amount of electron transfer from Im to metal for both Ag^{+}-DNA and Cu^{2+}-DNA complexes, discarding the importance of the charge transfer induced electrostatic stabilization for the calculated extra stability. Thus, we ascribe the extra stability of the Cu^{2+}-DNA to the greater extent of orbital hybridization, but not to the Columbic stabilization because of the charge transfer. We plot the difference in charge density in

Table 3.2: Binding energy ($E_b/{E_b}^c$) and displacement energy ($E_d/{E_d}^c$) per metal atom, average electron transfer (ET) from ligand to each Cu^{2+}, and magnetic moment (μ_B). Basis set superposition corrected displacement energies are given within bracket.

Systems	${E_b}^c$ (kcal mol^{-1})	${E_b}^c$(kcal mol^{-1})	ET (e)	μ_B
Im-Cu^{2+}-Im	-357.21	-366.20 (-366.20)	1.36	1.00
Im-$Cu^{2+}(H_2O)_2$-Im	-396.87	-409.56 (-405.87)	1.48	1.00
Im-$Cu(OH)_2$-Im	-24.67	-38.51 (-38.28)	1.76	1.00
Cu^{2+}-DNA	-238.91	-81.40 (-26.06)	1.55	2.83

Fig. 3.9(a) which shows the spatial distribution of transferred charges for Cu^{2+}-DNA complex. As can be seen from this figure, the Cu^{2+} accumulates electrons while there is an electron density reduction for the associated ligands. We also plot the spin-density distribution in Fig. 3.9(b) which clearly shows that the total spin moment (ca. 2.83) is mainly localized on the three ferro-magnetically aligned Cu^{2+} ions with a small contribution on the adjacent ligands. Interestingly, in this study, we have found weak ferromagnetic interactions among the Cu^{2+} ions in Im-$Cu(OH)_2$-Im modified DNA duplex as discussed above.

To understand the electronic structure and its effect on the optical absorption properties of Cu^{2+}-DNA, we also calculate and plot the DOS and absorption spectra in Fig. 3.10. The calculated DOS reveals the signature of spin-polarization of the Cu^{2+}-DNA complex and reflects spin asymmetry. We find that the HOMO for the majority spin channel is mainly localized on the $Cu(OH)_2$ with less contribution from A:T and Im bases, whereas the LUMO for majority spin completely localized on A:T base pairs with a very small contribution from sugar-phosphate backbone. However, both the

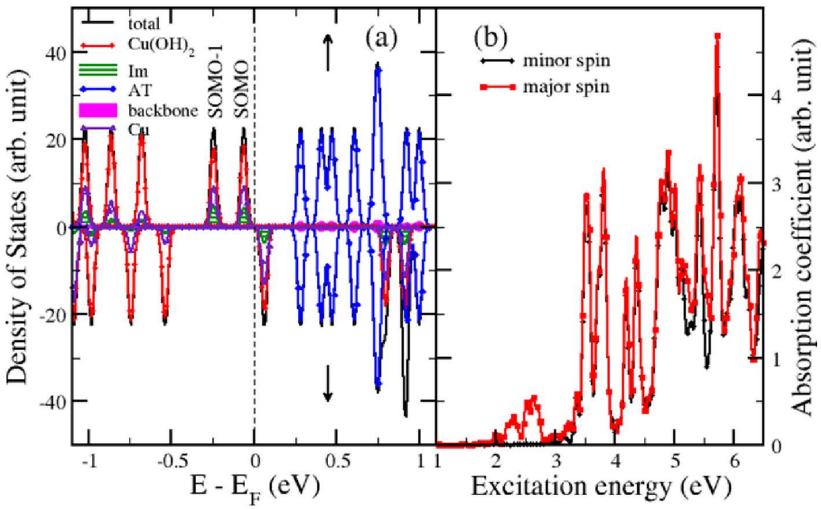

Figure 3.10: (a) DOS plot of Cu^{2+}-DNA complex and (b) optical absorption spectra of Cu^{2+}-DNA.

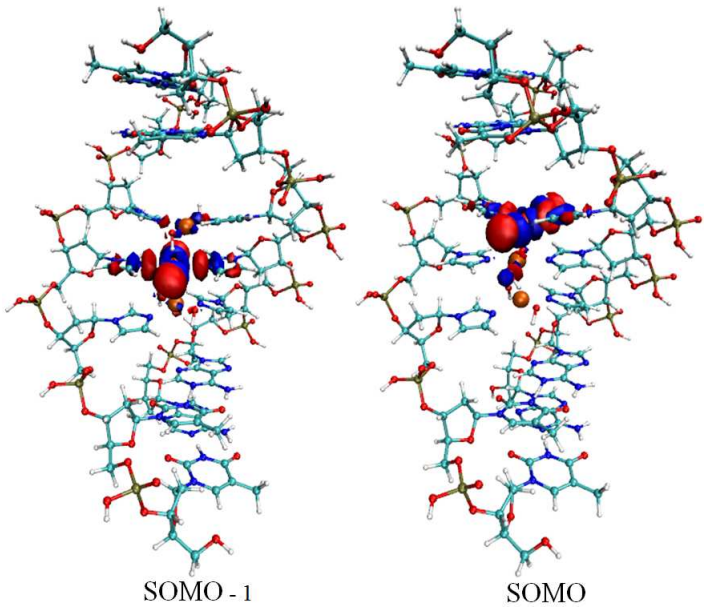

Figure 3.11: Single occupied molecular orbital (SOMO) of Cu^{2+}-DNA.

HOMO and LUMO for the minority spin channel mainly consist of $Cu(OH)_2$ with a marginal orbital contribution from A:T and Im bases. Furthermore, as shown in Fig. 3.10, the simulated optical absorption for Cu^{2+}-DNA shows low-energy peaks below 3.0 eV due to the spin-spin coupling, in sharp contrast to the absorption spectra obtained for Ag^{+}-DNA complex, where we find peaks only above 3.0 eV because of π-π^* orbital transitions from terminal A:T base pairs. Here, we would like to mention that the similar low-energy peaks for Cu and Mn incorporated DNA duplex was also demonstrated in previous studies, which was attributed to the spin-spin interactions as found in the present study. [123]

3.4 Conclusions

Using first-principles DFT calculations, we have shown that both Ag^{+} and Cu^{2+} can stabilize the duplex DNA by forming stable Im-Ag^{+}-Im/Im-Cu^{2+}-Im artificial base pairs with the greater extent of induced stabilization found for Cu^{2+}. We have found that both the charge transfer driven electrostatic stabilization and orbital hybridization are responsible in stabilizing the metal DNA complexes. We have also attributed the greater extent of stabilization for Cu^{2+}-DNA than Ag^{+}-DNA to the larger extent of orbital hybridization because of the presence of Cu 3d-orbitals. We have found that the presence of Na^{+} counter ions and water coordination has very marginal effect on the low-energy physics of these metal modified DNA duplexes. We have also found that the low-energy peaks in optical absorption arise mainly due to the π-π^* orbital transitions localized onto the terminal A:T base pairs for

Ag^{+}-DNA. On the other hand, the Cu^{2+}-DNA shows low-frequency optical absorption properties because of the spin-spin interactions. We have also observed strong spin polarization for the Cu^{2+}-DNA, suggesting its future potential applications in electronic devices.

Chapter 4

Magnetic Properties of a Variety of Transition Metal Incorporated DNA Double Helices*

4.1 Introduction

Deoxyribonucleic acid (DNA) is an efficient material to design complex nanostructures in a highly controlled manner due to its self-assembling properties. [232–234] The controlled alignment and self-assembly of atoms and molecules at the atomic scale can be achieved using DNA. The hydrogen-bonded (H-bonded) Watson-Crick base pairing can be replaced by metal-mediated base

*Work reported in this chapter is published in: P. K. Samanta and S. K. Pati, *Chem. Eur. J.* **20**, 1760-1764 (2014). Reproduced with permission from John Wiley and Sons.

pairing (MBP) in DNA to form metal-DNA (M-DNA) complexes. [235, 236] The metal ions within the double helical DNA scaffold can be aligned in a selective manner. [31] There have been several attempts to create an artificial MBP to form DNA duplex and selective metal ions can be incorporated inside the DNA duplex skeleton by varying the artificial nucleobases of different functionalities. [5, 31, 32]

Tanaka *et al.* reported the alignment of up to five Cu^{2+} ions within an M-DNA scaffold using hydroxypyridone MBP (H-MBP, Fig. 4.1a). [165] Both the experimental [165] study (Continuous-Wave Electron Paramagnetic Resonance (CW-EPR) spectra) and *ab initio* Density Functional Theory (DFT) calculation [123] provide the information about the ferromagnetic interactions between the Cu^{2+} centers and each Cu^{2+} ions are in a distorted square planer geometry. Later on, Clever *et al.* reported the alignment of up to ten Cu^{2+} ions within a M-DNA double helix using salicylaldehyde MBP (S-MBP) molecule in the presence of ethylenediamine (*en*, Fig. 4.1b). [164] Both experimental [190] study and theoretical *ab initio* calculations [123] showed the antiferromagnetic interactions among the Cu^{2+} ions centers. Liu *et al.* have recently been able to measure the conductance of M-DNA scaffold using H-MBP by varying different transition metal ions (*i.e.*, Cu^{2+}, Fe^{3+} and Ni^{2+}). [187] Therefore, it is possible to align different transition metal ions within an M-DNA scaffold using H-MBP and S-MBP to form low-dimensional magnetic arrays. Note that, some of the metal elements exists in +3 oxidation state within the DNA scaffold because of aerobic oxidation. [164, 237]

There are a few magnetic studies available for these systems. [123, 190]

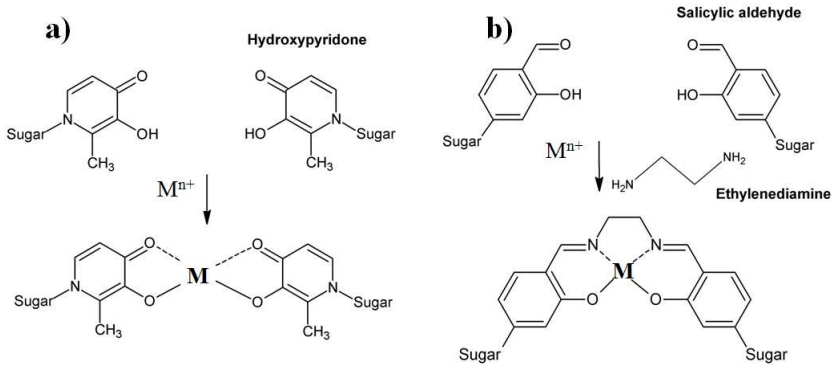

Figure 4.1: (a) hydroxyperidone MBP (H-MBP) and (b) salicylic aldehyde MBP in presence of ethylenediamine (S-en-MBP).

Also, due to the lack of crystallographic data, it is difficult to understand spatial arrangement of the magnetic ions and their overall structure and properties. Theoretical *ab initio* calculations can provide useful insights into the understanding of the magnetostructural properties of these systems. [123, 138,230] In this chapter, we have studied the spin polarized DFT calculations for the M-DNA systems, inclusive of the DNA backbone and the end base pairs. We have considered a variety of transition metal (Mn, Fe, Co, Ni and Cu) ions and studied the alignment of up to three metal ions chelated by H-MBPs and S-en-MBPs, within the modified DNA scaffolds. From our calculations, we find that the nature of the magnetic interactions is strongly dependent on the spatial arrangement of the MBPs.

4.2 Computational Methods

DFT package, SIESTA [75], was used for our calculations in gas phase. Troullier-Martins norm-conserving pseudo potentials in Kleinman-Bylander (KB) form was used together with Perdew, Burke, and Ernzerhof (PBE)

exchange-correlation energy functional within Generalized Gradient Approximation (GGA) [60]. A double-ζ basis set with polarization (DZP) [203] was included for all atoms together with a real-space mesh cut-off of 300 Ry. The conjugate gradient (CG) method was used for geometry optimization. Atomic relaxations in all of the calculations were performed until the forces on each atom were not larger than 0.04 eV $\mathring{A}^{-1}$. The DNA phosphate backbone was neutralized by protonating one of the oxygen of the phosphate groups, which does not alter the stability of the DNA duplex structure. [209] We have discussed this issue in *chapter 3*. We denote hydroxypyrido-incorporated DNA and bis(salicylaldehyde)ethylenediamine-incorporated DNA as nH-DNA and nS-en-DNA, respectively, where, n corresponds to the number of MBP aligned within the DNA helix. We considered two G:C base pairs at two ends of both nH-DNA and nS-en-DNA. The DFT calculations were carried out in supercells chosen such that the interactions between the neighboring fragments were negligible. The calculations had been performed in a supercell of volume $30\mathring{A} \times 30\mathring{A} \times 25\mathring{A}$, $30\mathring{A} \times 30\mathring{A} \times 30\mathring{A}$ and $30\mathring{A} \times 30\mathring{A} \times 40\mathring{A}$ for n=1, n=2 and n=3, respectively. The reliability of the DFT method employed in our study has well been tested for similar systems. [113, 123, 230]

For the calculation of nature of magnetic interactions, we have calculated exchange coupling constant (J) considering Heisenberg Exchange Hamiltonian,

$$H = -J \sum_{i>j} \vec{S_i} \cdot \vec{S_j} \tag{4.1}$$

where, $\vec{S_i}$ and $\vec{S_j}$ are the spin vectors at site i and j, respectively. Positive

Table 4.1: Spin Stabilization Energy (ΔE_s) and Exchange Coupling Constant (J).

Number of sites	$\vec{S}$	E_{hs}	E_{ls}	$\triangle E_s = E_{hs} - E_{ls}$
2	$S = \frac{5}{2}$	$-\frac{25}{4}J$	$\frac{35}{4}J$	-15J
	$S = 2$	$-4J$	$6J$	-10J
	$S = \frac{3}{2}$	$-\frac{9}{4}J$	$\frac{15}{4}J$	-6J
	$S = 1$	$-J$	$2J$	-3J
	$S = \frac{1}{2}$	$-\frac{1}{4}J$	$\frac{3}{4}J$	-J
3	$S = \frac{5}{2}$	$-\frac{25}{2}J$	$15J$	$-\frac{55}{2}J$
	$S = 2$	$-8J$	$10J$	$-18J$
	$S = \frac{3}{2}$	$-\frac{9}{2}J$	$6J$	$-\frac{21}{2}J$
	$S = 1$	$-2J$	$3J$	$-5J$
	$S = \frac{1}{2}$	$-\frac{1}{2}J$	J	$-\frac{3}{2}J$

(negative) value of J indicates the FM (AFM) interaction. For spin trimer systems, we calculate the J values using nearest neighbor interactions and broken-symmetry approach within SIESTA calculations. [123] The relation between the spin stabilization energy (ΔE_s) and J is given in Table 4.1 for different values of $\vec{S}$.

The optical conductivities for all the M-DNA systems were calculated to probe whether the spin-spin interactions can affect the transport behavior of the systems. The optical conductivity is given by the Kubo formula:

$$\sigma_{1,\mu}(\omega) = \pi \frac{e^2}{V} \frac{1 - e^{-\beta\hbar\omega}}{\omega} \sum_{n,m} \frac{e^{-\beta\epsilon_n}}{Z} \delta(\epsilon_n - \epsilon_m - \hbar\omega) |\langle n|j_\mu|m\rangle|^2 \qquad (4.2)$$

where, ϵ_n and $|n\rangle$ are the energies and eigenstates of the DFT Hamiltonian. V denotes the volume of the unit cell and j_μ is the μ-th component of current. This optical conductivity does not include time-dependent DFT or scissors

corrections. The optical conductivity was calculated along the strand direction of the M-DNAs.

4.3 Results and Discussion

We first discuss the stability of the M-DNA complexes with different transition metal (Mn, Fe, Co, Ni and Cu) ions. In the absence of metal ions, single-stranded oligonucletides with multiple MBP units can not form continuous base-paired duplex structures. [32, 164, 165, 197] From the melting temperature (T_m) analysis, it is found that the M-DNA (M=Cu) duplexes are more stable in comparison to their corresponding natural DNA duplex. Incorporation of a H-MBP (S-en-MBP) unit increased the T_m by 13 K (40 K). S-en-DNAs show high T_m due to the chelate effect of S-en-MBP ligand. To analyze the relative stability of the nH-DNA and nS-en-DNA, we have calculated the energy required to displace the metal ions from the M-DNA scaffold. The displacement energy (E_d) is defined as:

$$E_d = E_{[M-DNA]} + 2nE_{[H_2O]} - E_{[scs]} - nE_{[M(OH)_2]} \tag{4.3}$$

where, $E_{[M(OH)_2]}$, $E_{[sca]}$, $E_{[H_2O]}$ and $E_{[M-DNA]}$ are the energies of $M(OH)_2$, M-DNA scaffold, water and M-DNA, respectively and n is the number of metal ions in the M-DNA structure. The negative value of E_d indicates the stability of M-DNA structures. We found the increase in the magnitude of E_d with n for all the metal ions (M= Mn, Fe, Co, Ni and Cu, see Fig. 4.2). Thus, the stabilization energy upon the formation of MBP ($\sim$ 80 kcal mol^{-1})

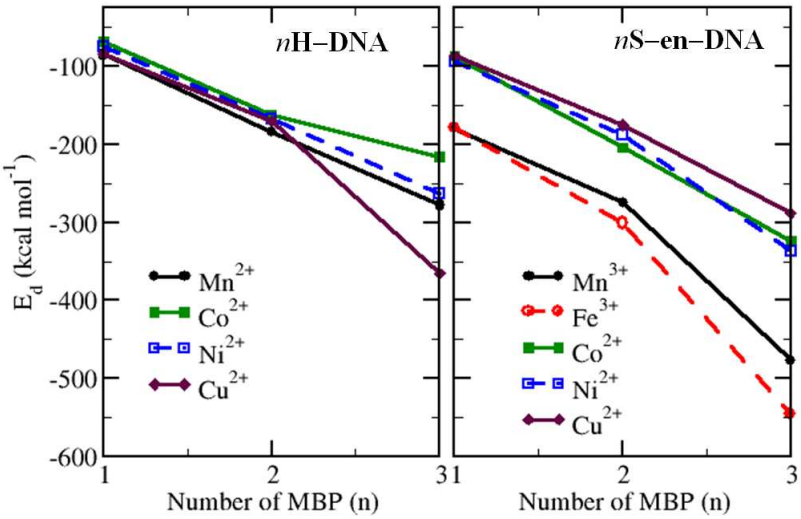

Figure 4.2: Displacement energy (E_d) for nH-DNA and nS-en-DNA with different metal (M) ions.

is greater than the stabilization energy upon the formation of H-bonded base pair (9-25 kcal mol^{-1}).

Then we have turned our attention towards the structural aspects of M-DNA complexes. Fe^{3+} interacts with hydroxyperidone containing oligonucleotides and form triple-stranded helices. [167] Since, here, we focus on the formation of metal incorporated double helices, we did not consider Fe^{3+} in case of nH-DNA systems. In the optimized structure of nH-DNA, metal ions are present in a distorted square planar arrangement. Again, Mn^{2+} is known to be oxidized to Mn^{3+} under aerobic conditions in case of nS-en-DNA. [164, 237] Hence, we have considered nS-en-DNA with Mn^{3+} and Fe^{3+} ions along with Co^{2+}, Ni^{2+} and Cu^{2+} ions in our study. The optimized structures of nS-en-DNA, with metal ions, Mn^{3+} and Cu^{2+}, are present in distorted square planar arrangement, however, Fe^{3+} and Ni^{2+} are present in quite perfect square planar arrangement (see Fig. 4.3, Fig. 4.4 and Fig. 4.5).

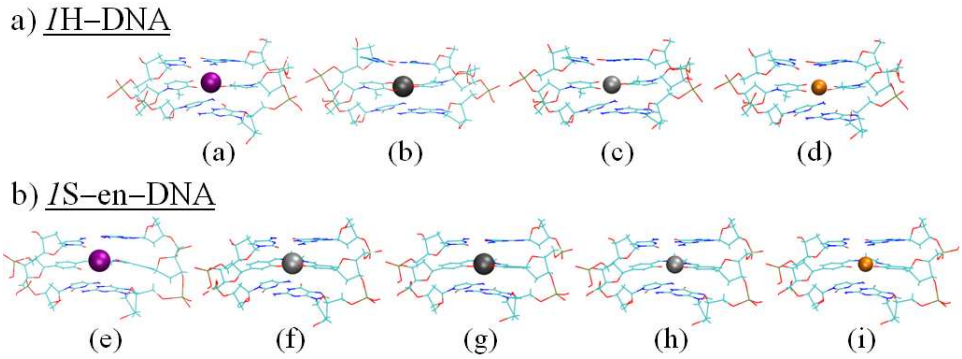

Figure 4.3: Optimized structure of 1H-DNA and 1S-en-DNA. 1H-DNA: (a) Mn^{2+}-DNA, (b) Co^{2+}-DNA, (c) Ni^{2+}-DNA, and (d) Cu^{2+}-DNA. 1S-en-DNA: (e) Mn^{3+}-DNA, (f) Fe^{3+}-DNA, (g) Co^{3+}-DNA, (h) Ni^{2+}-DNA and (i) Cu^{2+}-DNA.

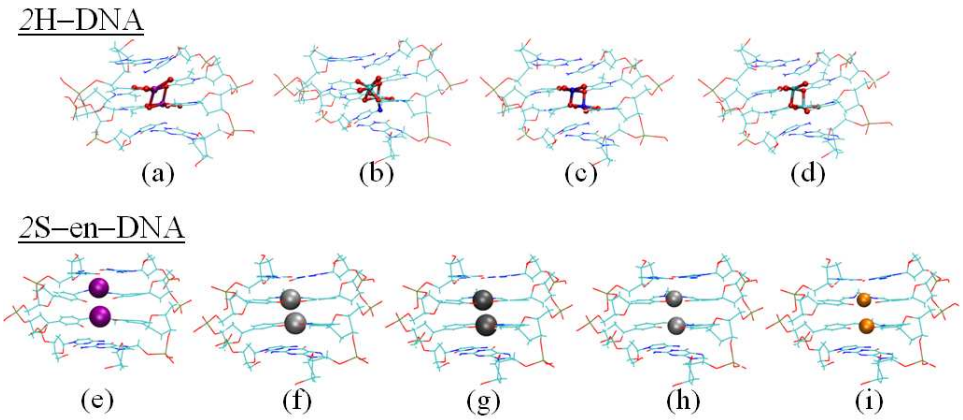

Figure 4.4: Optimized structure of 2H-DNA and 2S-en-DNA. 2H-DNA: (a) Mn^{2+}-DNA, (b) Co^{2+}-DNA, (c) Ni^{2+}-DNA, and (d) Cu^{2+}-DNA. 2S-en-DNA: (e) Mn^{3+}-DNA, (f) Fe^{3+}-DNA, (g) Co^{3+}-DNA, (h) Ni^{2+}-DNA and (i) Cu^{2+}-DNA.

The deviation from planarity is more for Co^{2+} incorporated nS-en-DNA. The M-M distances are higher for nS-en-DNA than nH-DNA (Table 4.2). For 2H-DNA and 3H-DNA complexes, each metal ion is coupled to its neighboring metal ion(s) *via* two bridging oxygen atoms, leading to the formation of an extended M-O network (Fig. 4.4). Similar structural arrangements are found for Co^{2+} in the optimized structures of 2S-en-DNA and 3S-en-DNA. We have found the distance between two consecutive metal ions are 3.60 $\mathring{A}$, 2.73 $\mathring{A}$, 3.50 $\mathring{A}$ and 3.24 $\mathring{A}$ for Mn^{2+}, Co^{2+}, Ni^{2+} and Cu^{2+} incorporated 2H-DNA, respectively. In fact, the distances between metal ions in case of 2S-en-DNA are 4.03 $\mathring{A}$, 3.28 $\mathring{A}$, 3.57 $\mathring{A}$, 3.81 $\mathring{A}$ and 3.24 $\mathring{A}$ for Mn^{3+}, Fe^{3+}, Co^{2+}, Ni^{2+} and Cu^{2+}, respectively. The metal-metal distances are lesser for nH-DNA than the corresponding distances for nS-en-DNA due to the extended M-O network in nH-DNA. We have found that while both H-MBP and S-en-MBP lead to the alignment of metal ions within the DNA scaffold, the alignment of metal ions in nH-DNA is facilitated by the formation of extended M-O network. On the other hand, the alignment of metal ions in nS-en-DNA is facilitated by the ordered stacking arrangement of S-en-MBP moieties. The Co-Co bond distances are lesser compared to other metal ions in H-DNA complexes. This is due to the octahedral geometry of Co^{2+} in H-DNA complex where, one of the two Co^{2+} ions is also connected to the two oxygen atoms of other H-MBP (Fig. 4.4b).

We now discuss the magnetic exchange interactions of these systems. To calculate the relative stability of spin states, we calculated the spin stabilization energy (ΔE_s) which is the difference between the highest spin (HS)

Table 4.2: Metal-metal distances (d1 and d2 in $\mathring{A}$) in nH-DNA and nS-en-DNA (n=2,3).

	Metal (M)-DNA	d1	d2	Coordination geometry
2H-DNA	Mn^{2+}-DNA	3.60	-	Tetrahedral
	Co^{2+}-DNA	2.73	-	Octahedral
	Ni^{2+}-DNA	3.05	-	Tetrahedral
	Cu^{2+}-DNA	3.24	-	Tetrahedral
3H-DNA	Mn^{2+}-DNA	3.58	3.55	Tetrahedral
	Co^{2+}-DNA	3.11	3.22	Octahedral
	Ni^{2+}-DNA	3.25	3.12	Tetrahedral
	Cu^{2+}-DNA	3.43	3.36	Tetrahedral
2S-en-DNA	Mn^{3+}-DNA	4.03	-	Planar
	Fe^{3+}-DNA	3.28	-	Planar
	Co^{3+}-DNA	3.57	-	$\sim$ Planar
	Ni^{2+}-DNA	3.81	-	Planar
	Cu^{2+}-DNA	3.79	-	Planar
3S-en-DNA	Mn^{3+}-DNA	3.98	4.05	Planar
	Fe^{3+}-DNA	3.38	3.39	Planar
	Co^{3+}-DNA	3.61	3.79	Not Planar
	Ni^{2+}-DNA	3.56	4.03	Planar
	Cu^{2+}-DNA	3.51	3.65	Planar

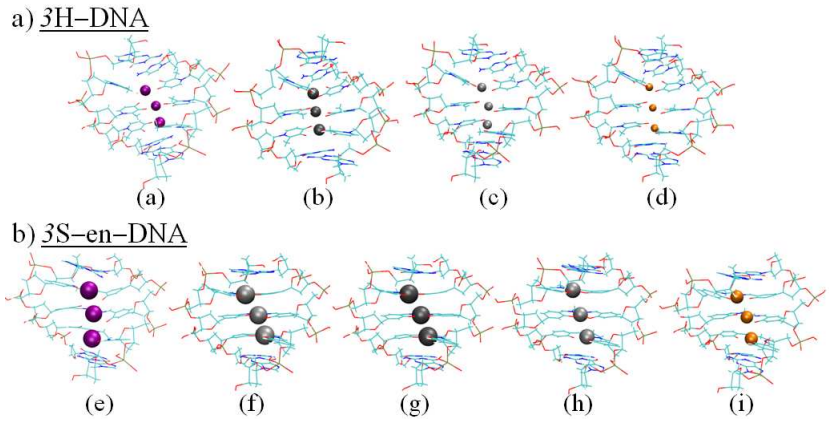

Figure 4.5: Optimized structure of 3H-DNA and 3S-en-DNA. 3H-DNA: (a) Mn^{2+}-DNA, (b) Co^{2+}-DNA, (c) Ni^{2+}-DNA, and (d) Cu^{2+}-DNA. 3S-en-DNA: (e) Mn^{3+}-DNA, (f) Fe^{3+}-DNA, (g) Co^{3+}-DNA, (h) Ni^{2+}-DNA and (i) Cu^{2+}-DNA.

and lowest spin (LS) states. The HS state is the state where all the transition metal's 3d orbital spins are aligned in parallel and LS state is the state where electronic spin of two nearest metal centers are aligned in anti-parallel arrangement. The ΔE_s are tabulated in Table 4.3 for nH-DNA and nS-en-DNA systems with different metal ions for $n = 1 - 3$. We found for all the systems, spin density is localized over metal ions and the coordinating atoms (nitrogen and/or oxygen) and not over sugar or phosphate backbone of the M-DNA complexes (Fig. 4.6). The ΔE_s gives the ferromagnetic (FM) or antiferromagnetic (AFM) interaction among the metal ions (see Table 4.3). We found that there are atomic high spin arrangements for all the metal ions (Mn^{2+} (S=5/2), Co^{2+} (S=3/2) and Ni^{2+} (S=1)) in 1H-DNA and for Mn^{3+} (S=2) and Fe^{3+} (S=5/2) in 1S-en-DNA. On the other hand, there are atomic low spin arrangements for Co^{2+} (S=1/2) and Ni^{2+} (S=0) in 1S-en-DNA. We first calculated the magnetic interaction for 2H-DNA and 2S-en-DNA which have two metal ions in their scaffolds. In case of 2H-DNA, all the metal ions show FM interactions. On the other hand, Mn^{3+}, Fe^{3+} and Cu^{2+} ions show AFM interactions in case of 2S-en-DNA. It is very interesting to note that, Ni^{2+} form square planar geometry with S-en-MBP with zero unpaired electrons and hence the total spin is zero for nS-en-DNA for all the values of n (Fig. 4.6h). We then turned our attention to the change in FM and AFM interactions with increase in the number of MBP. AFM interaction increases with increase in the number of MBP for Mn^{3+} and Fe^{3+} incorporated nS-en-DNA whereas, it is decreased with increase in the number of MBP for Cu^{2+} incorporated nS-en-DNA.

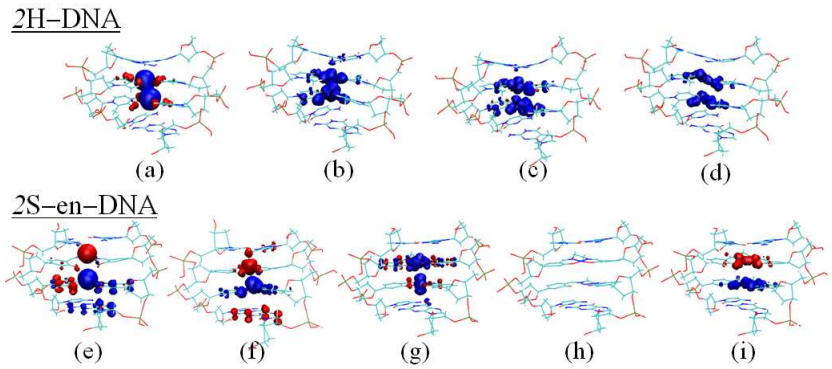

Figure 4.6: Spin density diagram of 2H-DNA and 2S-en-DNA. 2H-DNA: (a) Mn^{2+}-DNA, (b) Co^{2+}-DNA, (c) Ni^{2+}-DNA, and (d) Cu^{2+}-DNA. 2S-en-DNA: (e) Mn^{3+}-DNA, (f) Fe^{3+}-DNA, (g) Co^{3+}-DNA, (h) Ni^{2+}-DNA and (i) Cu^{2+}-DNA. Color code: Red and blue define two different spin densities.

For the quantitative calculation of FM or AFM interaction, we calculated exchange coupling constant (J) considering Heisenberg Hamiltonian. We found that for Mn^{2+} incorporated 2H-DNA, J is ferromagnetic with a magnitude of 4.91 cm^{-1} whereas, for Mn^{3+} incorporated 2S-en-DNA, the J is antiferromagnetic (-1.80 cm^{-1}). In case of 2H-DNA, Co^{2+} show FM interaction as indicated from their ΔE_s value (-12.316 meV). But, in case of 2S-en-DNA, Fe^{3+} show AFM interaction (J = -6.94 cm^{-1}) whereas, Co^{2+} show FM interaction (J = 42.14 cm^{-1}). Cu^{2+} shows FM interaction in nH-DNA and AFM interaction in nS-en-DNA, while Ni^{2+} incorporated nS-en-DNA show diamagnetic property. We thus found increase in FM interaction with increase in n for nH-DNA for all the metal ions and increase in AFM interaction with increase in n for nS-en-DNA for Mn^{3+} and Fe^{3+} (see Table 4.3).

The origin of different magnetic interactions in nH-DNA and nS-en-DNA for $n \geq 2$ arises because of their structural differences and can be explained using Goodenough-Kanamori rules and the orthogonality of the magnetic

Table 4.3: Exchange Coupling Constant (J) of different M-DNA Systems.

M-DNA		$\triangle E_s$ (meV)	J (cm^{-1})	Magnetic behavior
2H-DNA	Mn^{2+}	-9.138	4.91	FM
	Co^{2+}	-12.136	16.31	FM
	Ni^{2+}	-2.586	6.95	FM
	Cu^{2+}	-4.262	34.38	FM
3H-DNA	Mn^{2+}	-6.642	1.95	FM
	Co^{2+}	-15.527	11.93	FM
	Ni^{2+}	-17.568	28.34	FM
	Cu^{2+}	-8.393	45.13	FM
2S-en-DNA	Mn^{3+}	2.232	-1.80	AFM
	Fe^{3+}	12.901	-6.94	AFM
	Co^{2+}	-5.225	42.14	FM
	Ni^{2+}	0.00	0.00	Diamagnetic
	Cu^{2+}	1.691	-13.64	AFM
3S-en-DNA	Mn^{3+}	23.617	-10.58	AFM
	Fe^{3+}	51.505	-15.11	AFM
	Co^{2+}	-15.434	82.99	FM
	Ni^{2+}	0.00	0.00	Diamagnetic
	Cu^{2+}	-0.071	0.39	AFM

orbitals. [123, 238, 239] In 2S-en-DNA and 3S-en-DNA, more ordered pair wise stacked arrangement are found for metal-S-en-MBPs compare to metal-H-MBPs. Also, the metal-metal distances are larger in case of nS-en-DNA compared to the metal-metal distance in nH-DNA (Table 4.2). FM interactions can be explained using Heitler-London model. According to that model, the exchange coupling constant can be expressed as $J = K + 2\beta S_{ovl}$, where K is the two-electron exchange integral (positive) and β is the resonance coupling (negative) and S_{ovl} is the overlap integral. The first term (K) and second term ($2\beta S_{ovl}$) give the FM and AFM interactions, respectively. The second term vanishes when the two magnetic orbitals are orthogonal to each other leading to FM interactions. The near orthogonality of the intervening magnetic orbitals is brought about by the formation of the four-atom $\{M_2O_2\}$ convex quadrangle structure in case of nH-DNA by out of plane M-O interactions for all the metals in our study. Similarly, orthogonality of magnetic orbitals are found for Co^{2+} incorporated nS-en-DNA.

Nonzero contributions to the optical conductivity for natural DNA appear only above the 3 eV ($\pi - \pi^*$ transition). [205] Low energy excitations for the M-DNA system can be probed for the signature of spin-spin coupling. The low-energy optical conductivity of 2H-DNA and 2S-en-DNA are shown in the Fig. 4.7. There exist many low energy peaks for nH-DNA because of FM interactions. We found optical conductivity peak near 1.05 eV and 0.75 eV for 2H-DNA and 2S-en-DNA, respectively for all the metal ions. Intensity of the peak increases with an increase in the number of MBP.

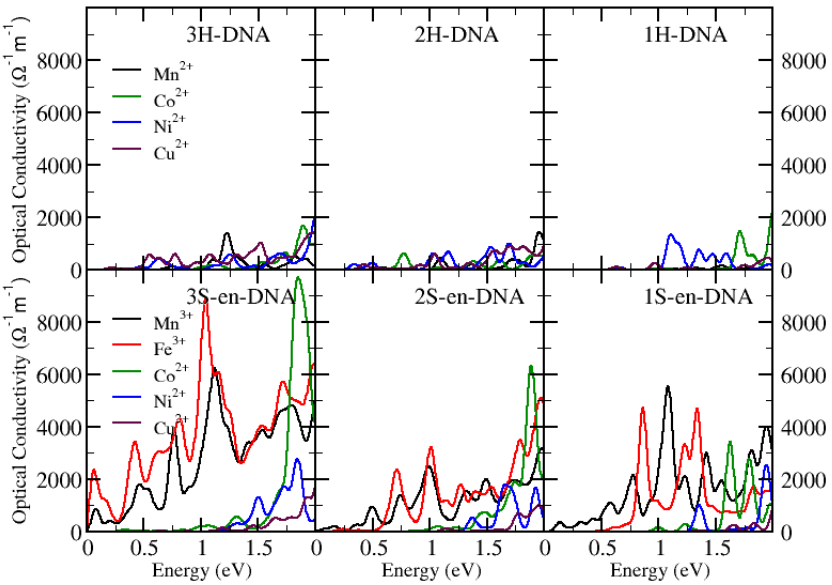

Figure 4.7: Optical conductivity diagram of nH-DNA and nS-en-DNA for n=1-3.

4.4 Conclusions

In summary, we have shown that the magnetic interaction in M-DNA complexes mainly depend on the conformational characteristics of the MBP. In case of 2H-DNA, all the metal ions interact ferromagnetically. The FM interaction increases with an increase in the number of metal ions in nH-DNA. On the other hand, Mn^{3+}, Fe^{3+} and Cu^{2+} ions show AFM interactions in 2S-en-DNA. The AFM interaction increases with increase in MBP for Mn^{3+} and Fe^{3+} incorporated nS-en-DNA and decreases with increase in MBP for Cu^{2+} incorporated nS-en-DNA. Ni^{2+} form square planar geometry in 1S-en-DNA with zero unpaired electrons. Optical conductivity can be used as a soft-probe technique for spin-spin interactions in M-DNA. Some of these M-DNA systems can be used for advanced device applications as low-dimensional magnetic arrays.

Chapter 5

Structural and Optical Properties of Single-stranded DNA encapsulated Silver/Gold clusters*

5.1 Introduction

Few atoms metal clusters (*e.g.*, Ag, Au, Pt) are important because of their photoluminescence, [240–244] single-molecule optoelectronics, [240,245] sensing, [246] chirality, [247–250] magnetism [251, 252] and bioassay [253–256] properties. Their smaller size, high photostability and non-toxicity make them highly appreciated fluorophore over mostly used organic fluorophores

*Work reported in this chapter is published in: P. K. Samanta, G. Periyasamy, A. K. Manna, and S. K. Pati, J. Mater. Chem. **22**, 6774 - 6781 (2012). Reproduced by permission of The Royal Society of Chemistry.

(*e.g.*, fluorescein isothiocyanate, acridine orange) [257] and semiconductor quantum dots (*e.g.*, CdSe, InAs) [243, 258]. These clusters can be prepared as nanocomposites by reduction of corresponding dissolved metal salts in the presence of dendrimer, [259,260] long chain polymer [261,262] or bio-polymers like deoxyribonucleic acid (DNA) [241, 263–271] scaffolds in aqueous media. The proper scaffold molecules are necessary to provide the stability of the metal clusters, to prevent the aggregation of metal atoms to form larger nanoparticles or to form bulk metal. Among these, DNA, a genetic material is more suitable scaffold, since it is easy to tune the structure and properties of metal clusters by varying nucleobase sequences. Both single-stranded DNA (ssDNA) and double-stranded DNA (dsDNA) have great potential application in fabrication and construction of nanostructures and nanodevices. [263, 272] The use of DNA (both ssDNA and dsDNA) to assemble metals or semiconducting particles have been extended to construct metallic nanowires [273] and metal clusters [241, 259, 260, 263–269] and programmed self-assembly [274, 275]. This work focusses on the highly biocompatible and non-photobleachable silver [276] and gold [277] clusters. Silver and gold nanoparticles show size-dependent plasmon absorption, when the sizes are less than their electron mean free path (52 nm for silver and 20 nm for gold) and greater than Fermi wavelength of electrons ($\sim$2 nm). [278–282] In fact, the nanoparticles with diameter less than 2 nm show molecule like properties of discrete energy state and size-dependent fluorescence properties. [242, 246, 283] Experimentally, the size and shape of silver and gold clusters are controlled by DNA sequences used for their formation. [263, 272] For example, thymine-rich oligonucleotides form only blue/green-emitting

and cytosine-rich oligonucleotides form red emitting silver clusters. [272] This makes DNA more important over other oligomer scaffolds. Again, ssDNA is more powerful to make metal clusters than dsDNA because of its flexibility. [263, 284, 285] Many experimental studies have been reported to understand the formation of silver and gold clusters and their fluorescence properties. [241, 259, 260, 263–269] In addition, experimentally their sizes are determined based on their fluorescence properties in UV-visible region. [240–242, 272, 286, 287] Hence, theoretical and computational investigations are necessary to understand the interaction between the various scaffold and nanoclusters. There exists a few theoretical studies on the interactions between the silver [288] and gold [194, 289] clusters and single or double nucleobase moieties using density functional theory (DFT). The adsorption of nucleobases, [290] ssDNA ($ssdA_{10}$, $ssdT_{10}$) [291] and dsDNA (hybrid sequences) [292] molecules on Au(111) surface have already been studied using molecular dynamics (MD) simulation. Lee *et al.* [293] have computationally studied the interaction between two gold nanoparticles *via* ssDNA (hybrid sequences) using MD simulations. However, to our knowledge, there is no theoretical study on the complete ssDNA (base, sugar and phosphate) and few atoms silver or gold metal clusters and their absorption properties.

In this chapter, we have studied the structure, energetics and free energies of Ag_{12} and Au_{12} clusters in presence of ssDNA scaffold of various nucleobase sequences (*i.e.*, $ssdA_{12}$, $ssdT_{12}$, $ssdG_{12}$ and $ssdC_{12}$) in aqueous media. The computed structures are validated by comparing their optical properties with the respective experimental results. The optical properties of silver (Ag_{12}) and gold (Au_{12}) clusters, ssDNA ($ssdA_{12}$, $ssdT_{12}$, $ssdG_{12}$ and $ssdC_{12}$) along

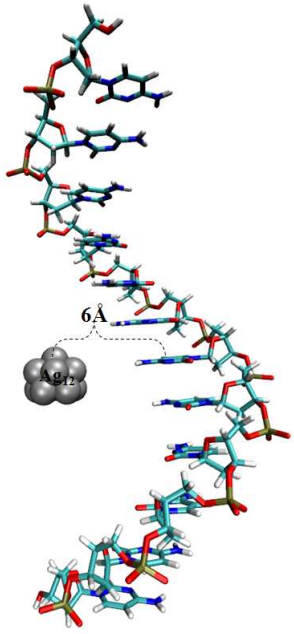

Figure 5.1: The initial configuration of Ag_{12}-$ssdC_{12}$ nanocomposites considered for MD simulations.

with their hybrids (Ag_{12}-ssDNAs and Au_{12}-ssDNAs) are calculated with the MD simulated structures alone.

5.2 Computational Methods

Nanocomposites of Ag_{12}/Au_{12} clusters and ssDNA scaffolds were considered in 1:1 ratio with 12 atoms of Ag/Au and 12 nucleobase ssDNA sequences ($ssdA_{12}$, $ssdT_{12}$, $ssdG_{12}$ and $ssdC_{12}$) for the present study. Initial conformers of 12 atom nanoclusters were created based on Sutton-Chen's transition metal clusters. [294] The four different ssDNA sequences were generated using nab (nucleic acid builder) module implemented in the AMBER11 Tools package. [295] The AMBER99 force-fields [296] were used to model ssDNA and

the neutral metal atoms are modelled as Lenard-Jones (LJ) particles. The LJ parameters were taken from literature for silver [297, 298] and gold [291] atoms. These parameters were already used to study growth of Ag film [297] and the interaction between Au(111) surface and ssDNA or dsDNA [291,292] which show the reliability of the parameters. The main point of our work is to find out the origin of optical properties of these clusters in presence of ssDNA scaffold. The transferable intermolecular potential three-point (TIP3P) model was considered for water solvent. [299, 300] The MD simulation was performed using the GROMACS-4.0.7 MD package [97] in an initial cubic water box of length 70 $\mathring{A}$ at room temperature (300 K) [88] and constant atmospheric pressure (1 bar) [87]. The simulation box contains 11260 TIP3P water molecules for all the MD simulations. The charges of the systems were neutralized using Na^+ as counter ions. Initially, the high energy contacts between the atoms in the initial conformations of Ag_{12}, Au_{12} and ssDNA sequences were removed by minimizing the energy using steepest decent method. Following that, NPT simulations were carried out using leap-frog algorithm for integrating Newton's equation of motion for 1.5 ns at constant temperature (300 K) and pressure (1 bar). The periodic boundary condition was applied in all three directions. Electrostatic interactions were calculated with the Particle Mesh Ewald (PME) method. [93] The time step for the MD simulation was 1.5 fs. Atomic coordinates were recorded for every 7.5 ps for trajectory analysis. Metal clusters and ssDNA sequences ($ssdA_{12}$, $ssdT_{12}$, $ssdG_{12}$ and $ssdC_{12}$) were kept $\sim$6.0 $\mathring{A}$ distance apart from each other in the initial geometry of the MD simulation, as shown in the Fig. 5.1. The MD trajectory was viewed by Visual Molecular Dynamics (VMD) software. [102]

Thermodynamic integration (TI) [301] as implemented in the GROMACS-4.0.7 MD package was employed to compute the binding free energies of the metal clusters and ssDNA sequences by introducing various coupling parameters (λ) in the Hamiltonian (H).

The binding free energies (ΔF_{bind}) were computed by considering two different thermodynamic cycles (See Fig. 5.2) based on the previous work. [301, 302] In the former case (Scheme -I), ${\Delta F_{bind}}^{I}$ was defined as the free energy difference between the bound (${\Delta F_b}^{I}$) and unbound states (${\Delta F_{unb}}^{I}$). In the latter case, Scheme -II, ${\Delta F_{bind}}^{II}$ the free energy difference between the complex formation (${\Delta F_{comp}}^{II}$) and solvation (${\Delta F_{sol}}^{II}$) was considered. This calculation required the computations to annihilate and create metal clusters in the unbound, free and bound states. The van der Waals (vdW) interactions were annihilated/created using λ values of 0.00, 0.25, 0.50, 0.75 and 1.00. Soft-core LJ potentials were employed with soft-core parameter α=0.5 and λ power $p = 1$. At each λ value, $(\delta H/\delta\lambda)$ was extracted from the 1.5 ns trajectory. To eliminate the sampling problems associated with decoupling vdW parameters, position restraints were applied to metal cluster (Ag_{12} or Au_{12}) in the bound state for higher λ values.

For DFT calculations, final conformers (after 1.5 ns) of nanocomposites were considered. DFT calculations were carried out using the SIESTA package. [75] Troullier-Martins norm-conserving pseudopotentials in the Kleinman-Bylander form were used together with the Generalized Gradient Approximation (GGA) for the exchange-correlation energy functional in the version of Perdew, Burke and Ernzerhof (PBE). [60] A double-ζ basis (DZP) set with the polarization orbitals was included for all atoms [203] together with

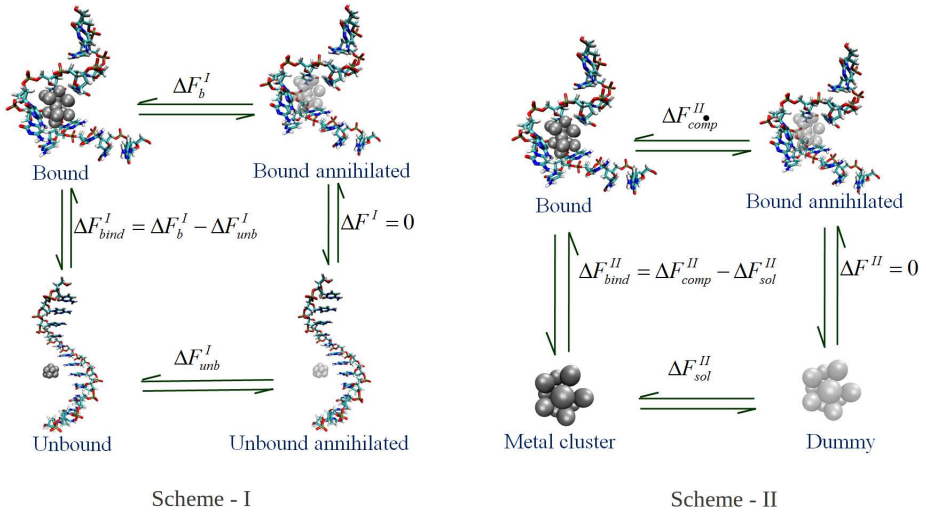

Figure 5.2: Schematic representations of two different thermodynamic cycles (Scheme-I and Scheme-II) used for free energy computations.

a real-space mesh cut-off of 300 Ry. All calculations were performed in a $60\mathring{A} \times 60\mathring{A} \times 60\mathring{A}$ supercell, which was large enough for interactions between the neighboring fragments to be negligible. DFT calculations were carried out by considering molecular system (with a single k-point, to be precise, the gamma point) with the MD simulated structure alone. The Na^+ and water molecules were removed from the final conformers. The negatively charged ssDNA were neutralized by protonating phosphate group, [209] which is reported to be an appropriate model for similar kind of systems. [211, 213, 214, 216] Absorption coefficients are calculated from imaginary part of dielectric constant. The calculations were performed using the simplest approach based on the dipolar transition matrix element between different eigenfunctions of the self-consistent Hamiltonian. [229] The reliability of this DFT method already has been proved for similar kind of systems. [123, 205–207]

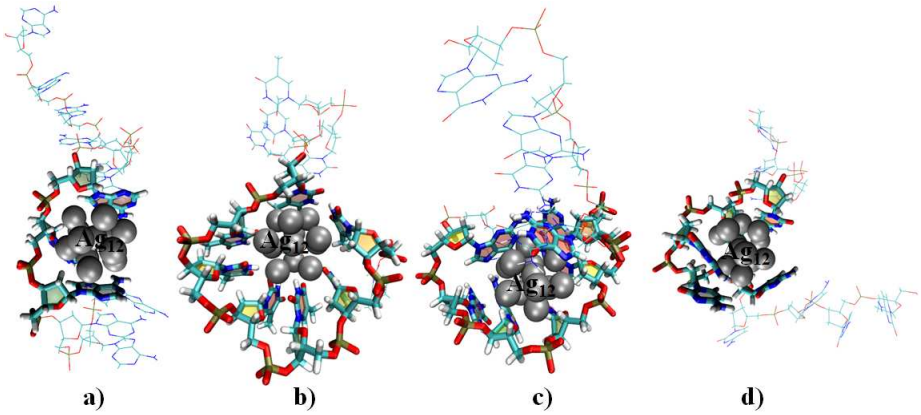

Figure 5.3: The configurations of Ag_{12}-$ssdA_{12}$ (a), Ag_{12}-$ssdT_{12}$ (b), Ag_{12}-$ssdG_{12}$ (c) and Ag_{12}-$ssdC_{12}$ (d) after 1.5 ns. For clarity, Ag_{12} clusters and nearby nucleobases are represented in sphere and tube formats, respectively. Nucleobases far from the Ag_{12} clusters are shown in wire frame. The water molecules and the counter ions (Na^+) are not shown.

5.3 Results and Discussion

5.3.1 Structural analysis of Ag_{12}/Au_{12} and ssDNA sequences in aqueous media

Our studies show that Ag_{12} and Au_{12} clusters are stable after 1.5 ns simulation in aqueous media at 300 K. The clusters are in quasi-spherical shape with the average radius of 2.88 $\AA$ for Ag_{12} and 2.82 $\AA$ for Au_{12}. In addition, simulations of ssDNA scaffolds alone in aqueous media provide evidence for the stability of its helical shape.

5.3.2 Structural and energetic analysis of Ag_{12}-ssDNA nanocomposites

For a nanocomposites simulation, Ag_{12} cluster was placed $\sim$6.0 $\mathring{A}$ apart from ssDNA in order to understand the mode of interaction during the course of MD simulation (see Fig. 5.1). After 0.1-0.2 ns, the ssDNA starts to wrap around the Ag_{12} cluster. Herein, we report the results after 1.5 ns MD simulations, where the fluctuations in total energies are quite negligible. The simulation shows that the environment around the Ag_{12} cluster depending upon the nature of ssDNA sequences, $ssdA_{12}$, $ssdT_{12}$, $ssdG_{12}$ and $ssdC_{12}$. The final structures are shown in the Fig. 5.3. Our computations provide the evidence that the silver cluster (Ag_{12}) is always surrounded by the nucleobases and not by the phosphates as reported in the previous experimental studies. [303] The simulation shows that the wrapping around the metal cluster completely switches the helical shape of initial conformer of ssDNA scaffolds to the folded conformers. Two types of interactions are found between the ssDNA and clusters, which are π-stacking and bonding *via* specific atom of the nucleobases (Nitrogen and/or Oxygen, for labelling see Fig. 1.2a).

The different amount of folding in ssDNA scaffolds and number of nucleobase around the clusters are reflected in their interaction energies (between the ssDNA and metal clusters). In order to quantitatively compare the E_{int} of the final configuration (after 1.5 ns), E_{int} of nanocomposites are given in the Table 5.1. The interaction energy order is $ssdG_{12} < ssdC_{12} < ssdT_{12} < ssdA_{12}$, which is directly proportional to the distance and number of nucleobases closely present around the cluster (see Fig. 5.3 and Table 5.1). The

Table 5.1: Number of nucleobases (N) involving in two types of interactions, computed interaction energy (E_{int} in kJ mol^{-1}) at 1.5 ns and binding free energy (ΔF_{bind} in kJ mol^{-1}, both scheme-I and scheme-II in Fig. 5.2) values for the simulated Ag_{12}-ssDNAs nanocomposites. N' and N'' are the number of nucleobases, interacting *via* π-cloud and specific atoms (Nitrogen and/or oxygen).

Systems	N	N'	N''	E_{int}	$\Delta F_{bind}{}^{I}$	$\Delta F_{bind}{}^{II}$
Ag_{12}-ssA_{12}	3	2	1	-450.30	-72.05	-739.53
Ag_{12}-ssT_{12}	7	2	5	-583.57	-434.80	-1222.77
Ag_{12}-ssG_{12}	5	3	2	-689.55	-557.98	-1223.23
Ag_{12}-ssC_{12}	5	5	-	-587.19	-156.11	-1176.88

$ssdG_{12}$ interacts strongly with Ag_{12} cluster (E_{int} = -689.55 kJ mol^{-1}) than other ssDNA sequences, as in case of $ssdG_{12}$, five nucleobases surround the cluster within 2.95-3.50 $\mathring{A}$, where three nucleobases interact *via* π-cloud of purine base and two bases interact through N3 atom of purine base as in Fig. 5.3c. However, in case of Ag_{12}-$ssdA_{12}$, only three bases (two *via* π-cloud and one *via* N3 atom) surround the Ag_{12} cluster within 3.08-3.68 $\mathring{A}$ (Fig. 5.3a). This results in lowest binding affinity (E_{int} = -450.30 kJ mol^{-1}) than the other ssDNA. $ssdC_{12}$ interacts with the metal cluster by π-cloud of five nucleobases within 3.16 -3.84 $\mathring{A}$, (Fig. 5.3d). Interestingly, $ssdT_{12}$ interacts with metal cluster mainly by O2 atom of the nucleobases (five nucleobase by O2 and two nucleobases by π-cloud, see Fig. 5.3b). Although it contains more number of nucleobases around the cluster, the lesser number of π- stacking nucleobases results in lower interaction energy. These results suggest that the interaction of nucleobases *via* π-cloud plays a crucial role in their binding affinity than the interaction *via* specific atom. The interaction *via* π-cloud is not seen in the previous results for silver cluster (Ag_n,

n=1, 6) with one or two nucleobases based on DFT. In fact, the DFT study shows that the interaction is *via* specific nitrogen or oxygen atom of the nucleobases. [288] This proves that complete sequence and its environments are necessary to understand the interaction between the ssDNA and metal clusters.

In addition to the interaction energy, we have calculated the binding free energies (ΔF_{bind}) for all the systems and those are reported in the Table 5.1. ΔF_{bind} are computed using two different thermodynamical cycles as shown in Fig. 5.2 (scheme -I and scheme -II). ${\Delta F_{bind}}^{I}$ accounts only the interaction between ssDNA and the metal cluster, while ${\Delta F_{bind}}^{II}$ considers the effect due to the solvation of metal cluster too. The computed free energies by two different methods follow the same trend ($ssdG_{12} < ssdT_{12} < ssdC_{12} < ssdA_{12}$) as those of the interaction energy order, except that the inclusion of conformational change results in higher interaction energy for $ssdT_{12}$ than $ssdC_{12}$. The huge magnitude difference between ${\Delta F_{bind}}^{I}$ and ${\Delta F_{bind}}^{II}$ are due to the presence of solvation energy of ssDNA in the case of ${\Delta F_{bind}}^{II}$. The calculated interaction energies using three different methods indicate that the $ssdG_{12}$ wraps the Ag_{12} cluster with strong π-interaction *via* 5-nucleobases than the $ssdT_{12}$, $ssdC_{12}$ and $ssdA_{12}$ scaffolds.

5.3.3 Structural and energetic analysis of Au_{12}-ssDNA

Following the Ag_{12} cluster, the interaction between Au_{12} and ssDNA are studied in order to understand their size effect. Similar to the silver, the interaction towards the gold cluster change the initial shape of ssDNA to

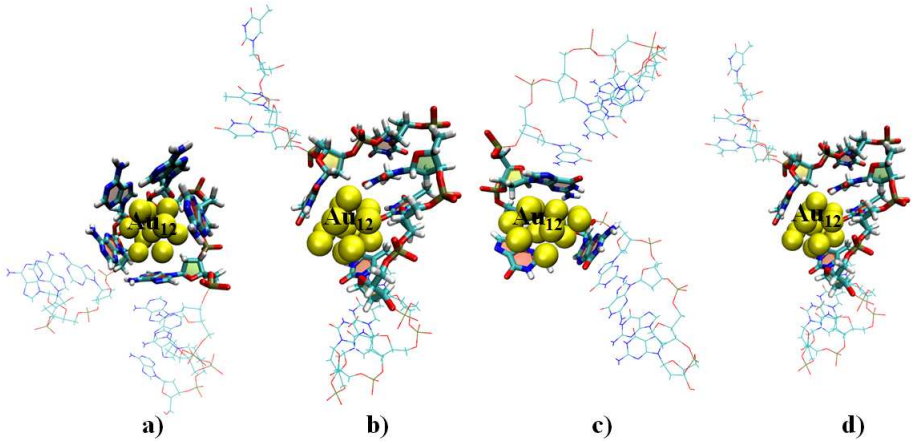

Figure 5.4: The configurations of Au_{12}-$ssdA_{12}$ (a), Au_{12}-$ssdT_{12}$ (b), ug_{12}-$ssdG_{12}$ (c) and Au_{12}-$ssdC_{12}$ (d) after 1.5 ns. For clarity, Au_{12} clusters and nearby nucleobases are represented in sphere and tube formats, respectively. Nucleobases far from the Au_{12} clusters are shown in wire frame. The water molecules and the counter ions (Na^+) are not shown.

the folded conformer (Fig. 5.4). The gold cluster interacts with the various nucleobases mainly *via* the π-electron cloud rather than the specific atoms.

Similar to the Ag_{12} cluster, interaction *via* π-electron cloud was not observed in the previously reported DFT studies between metal cluster and nucleobase molecules. [145, 289] The computed interaction energy order for Au_{12}-ssDNA nanocomposites is Au_{12}-$ssdA_{12}$ < Au_{12}-$ssdC_{12}$ < Au_{12}-$ssdG_{12}$ < Au_{12}-$ssdT_{12}$. In essence, in comparison to Ag_{12} cluster, Au_{12} prefer to wrap with more number of adenine nucleotide scaffold. In the case of Au_{12} cluster, $ssdA_{12}$ interact more with E_{int} of -748.39 kJ mol^{-1}, where five nucleobases surround the metal cluster within 2.83-3.25 $\AA$. Note that, all the five adenine nucleobases interact *via* π-cloud (Fig. 5.4a) of purine ring. Similarly,

Table 5.2: Number of nucleobases (N) involving in two types of interactions, computed interaction energy (E_{int} in kJ mol^{-1}) at 1.5 ns and binding free energy (ΔF_{bind} in kJ mol^{-1}, both scheme-I and scheme-II in Fig. 5.2) values for the simulated Au_{12}-ssDNAs nanocomposites. N' and N'' are the number of nucleobases, interacting *via* π-cloud and specific atoms (Nitrogen and/or oxygen).

Systems	N	N'	N''	E_{int}	$\Delta F_{bind}{}^{I}$	$\Delta F_{bind}{}^{II}$
Au_{12}-ssA_{12}	5	5	-	-748.39	-664.59	-1426.53
Au_{12}-ssT_{12}	4	2	2	-570.10	-139.37	-704.93
Au_{12}-ssG_{12}	3	3	-	-629.54	-260.45	-807.38
Au_{12}-ssC_{12}	4	4	-	-633.89	-638.35	-1063.27

$ssdG_{12}$ and $ssdC_{12}$ interact with Au_{12} cluster with three and four nucleobases within 3.04-3.20 $\mathring{A}$ and 3.01-3.36 $\mathring{A}$, respectively *via* π-cloud. Although $ssdC_{12}$ (Fig. 5.4d) has more nucleobases around the gold cluster, its smaller size results in less binding interaction than the $ssdG_{12}$ (Fig. 5.4c). On the otherhand for $ssdT_{12}$, two nucleobases interact with Au_{12} cluster *via* π-cloud and the two interact *via* oxygen of C(4)=O like Ag_{12}-$ssdT_{12}$ (within 3.05-3.62 $\mathring{A}$). Among the four ssDNA, both silver and gold clusters prefer to interact with $ssdT_{12}$ *via* O2 atom of pyrimidine ring rather than π-cloud.

We have computed the binding free energies for all the systems and have reported them in the Table 5.2. The computed free energies in two different methods follow the same trend (Au_{12}-$ssdA_{12}$ < Au_{12}-$ssdC_{12}$ < Au_{12}-$ssdG_{12}$ < Au_{12}-$ssdT_{12}$) and also agrees with the interaction energy order. Three different studies provide evidence that the $ssdA_{12}$ interacts with the Au_{12} cluster with more number of nucleotides than the $ssdT_{12}$, $ssdC_{12}$ and $ssdG_{12}$ scaffolds.

MD simulations demonstrate a detail binding regime between ssDNA

with Ag_{12} and Au_{12} cluster in 1.5 ns time scale. Our results based on number of wrapping nucleobases show that the purine containing nucleobases interact more with the Ag_{12} and Au_{12} clusters than the pyrimidine containing nucleobases, which are in good agreement with the already reported DFT results. [289] Moreover, the computed binding energy in the MD simulation completely depends upon the number of nucleobases present near the metal clusters. However, the systems considered in this work are more flexible and the extended simulation might lead to another local minimum, where the metal clusters could be surrounded by the same number of nucleobases. In order to overcome this problem, we have considered the composites configuration with the same number of nucleobases wrapped around the metal clusters and have computed the interaction energy using DFT method in the gas phase. We have created the structures of M_{12}-$ssdG_{12}$ (M=Ag, Au) from the final MD structure of Ag_{12}-$ssdG_{12}$ and Au_{12}-$ssdA_{12}$ with five nucleobases around the clusters from the final MD structure of Au_{12}-$ssdA_{12}$. When comparing Ag_{12}-$ssdG_{12}$ and Au_{12}-$ssdG_{12}$ composites with same number of nearby nucleobases, Ag_{12} prefers to bind more (54.99 kJ mol^{-1}) with $ssdG_{12}$ than Au_{12}. On the other hand, between the Ag_{12}-$ssdA_{12}$ and Au_{12}-$ssdA_{12}$ composites, Au_{12} interacts more (31.84 kJ mol^{-1}) with $ssdA_{12}$ than Ag_{12}.

5.3.4 Absorption Spectra

The DNA encapsulated silver and gold clusters are known for its strong fluorescent properties. [241, 259, 260, 263–269] The computational studies are

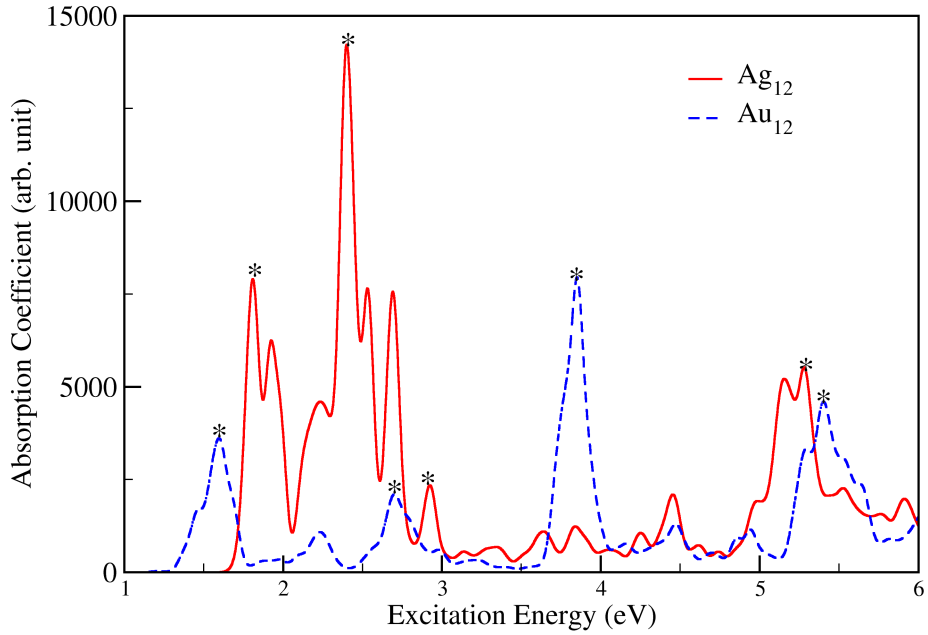

Figure 5.5: Computed absorption spectra of Ag_{12} and Au_{12} clusters. High intensity peaks are indicated '*' notation and their values are given in Table 5.3. The line spectra are broadened with Gaussian functions of width 0.05 eV.

required for the complete understanding of the linear optical properties including absorption and fluorescence processes. The absorption spectra are computed for all the systems in order to compare with the experimental spectra. The corresponding densities of states (DOS) together with partial density of states (pDOS) are calculated in order to explain the calculated absorption spectra.

The absorption spectra of Ag_{12} and Au_{12} alone are shown in Fig. 5.5. We find peaks at 1.80, 2.40, 2.70 and 5.26 eV for Ag_{12} and 1.60, 2.70, 3.85 and 5.40 eV for Au_{12} (see Fig. 5.5 and Table 5.3). The Au_{12} cluster shows 0.3-1.0 eV shift (blueshift) to the high energy three peaks (2.40-5.26 eV) when

Table 5.3: Excitation energies (eV) corresponding to intense peaks of the Ag_{12}, Au_{12}, ssDNAs, Ag_{12}-ssDNAs and Au_{12}-ssDNAs.

Systems	Transition Energy (eV)
Ag_{12}	1.80, 2.40, 2.70, 5.26 *(3.42, 3.91, 4.38) Ref. [304]*
Au_{12}	1.60, 2.70, 3.85, 5.40 *(1.63, 2.63, 2.76, 4.17, 5.00) Ref. [305]*
ssA_{12}	3.90, 4.68, 4.89, 5.67
ssT_{12}	3.63, 4.64, 4.91, 5.67
ssG_{12}	3.86, 4.16, 5.50, 5.90
ssC_{12}	4.14, 4.64, 5.03, 5.62
Ag_{12}-ssA_{12}	2.41, 3.80, 4.71, 5.05, 5.62
Ag_{12}-ssT_{12}	2.19, 2.46, 3.56, 4.80, 5.67
Ag_{12}-ssG_{12}	1.58, 2.43, 2.64, 3.87, 4.20, 5.89
Ag_{12}-ssC_{12}	2.27, 2.67, 3.99, 5.00 *(2.14, 2.82, 3.65, 4.43) Ref. [285]*
Au_{12}-ssA_{12}	1.62, 3.84, 4.98, 5.41
Au_{12}-ssT_{12}	1.64, 3.50, 4.87, 5.68
Au_{12}-ssG_{12}	1.74, 3.91, 5.73
Au_{12}-ssC_{12}	2.42, 3.00, 4.09, 5.07, 5.48

compared to the Ag_{12}. This is because of the smaller size of Au_{12} cluster (radius $\approx$ 2.82 $\mathring{A}$) than the Ag_{12} (radius $\approx$ 2.88 $\mathring{A}$). Decrease in the Au_{12} cluster size increases the energy difference between the orbitals (see Fig. 5.6), which is the reason for its blue shift. This trend is also correlated with the relativistically enhanced stronger s-d hybridisation and d-d interaction in the orbitals of Au_{12} than in Ag_{12}, which is already reported for similar kind of systems. [306,307] This shift is in good agreement with the energy difference between the low energy molecular orbitals (MO) (see Fig. 5.6 and Table 5.3) for both the systems. The computed absorption spectra values of cluster alone (1-4 eV) are comparable with already reported calculated values (Ag_{12} 2.5-4 eV [304] and Au_{12} 1-3 eV [305]) elsewhere.

Similarly, the absorption spectra of the $ssdA_{12}$, $ssdT_{12}$, $ssdG_{12}$ and $ssdC_{12}$

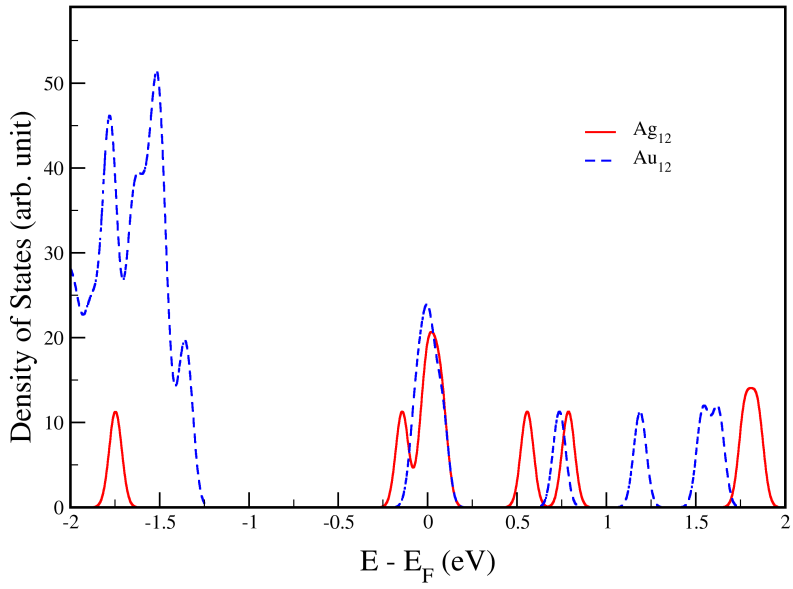

Figure 5.6: Computed electronic density of states (DOS) for Ag_{12} and Au_{12} clusters using DFT. The energy is scaled with respect to Fermi energy (E_F).

alone have been studied. All the sequences show peaks > 3 eV (See Fig. 5.7 and Table 5.3) of excitation energy, which obviously correspond to π-π^* transition. [123, 205] The computed excitation energies are in good agreement with the already reported results for DNA. [123, 205] The structural differences between various sequences is the reason for shift (red/blue shift) in the absorption peaks (see Table 5.3 and Fig. 5.7). Following the individual clusters and ssDNA, the absorption spectra for Ag_{12}-ssDNA and Au_{12}-ssDNA nanocomposites have been analyzed in detail.

The computed absorption spectra of Ag_{12}-ssDNA and Au_{12}-ssDNA nanocomposites are shown in Fig. 5.9 and Fig. 5.11, respectively. The observed plots provide the evidence that the metal dependent (1-3 eV) and ssDNA dependent (>3 eV) peaks are distinct. This is reflected in the density of states

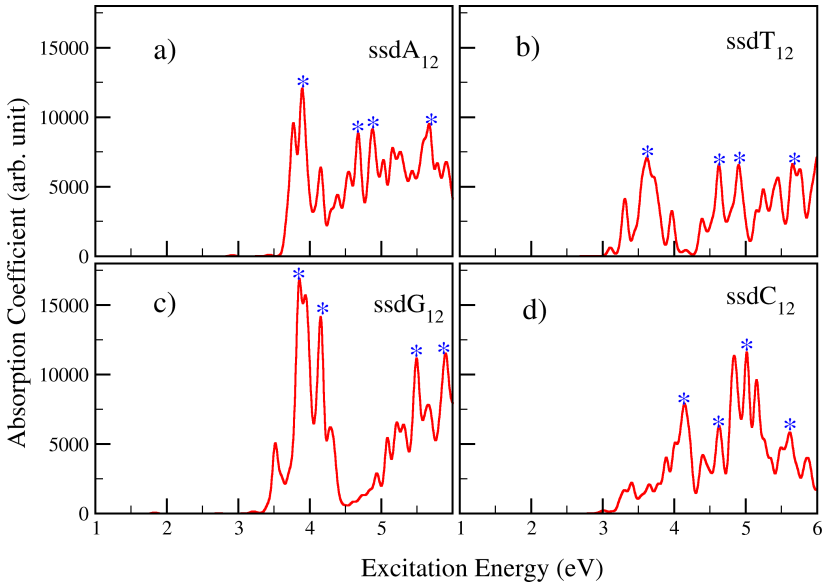

Figure 5.7: Computed absorption spectra for different ssDNA (ssA_{12} (a), ssT_{12} (b), ssG_{12} (c) and ssC_{12} (d)). High intensity peaks are indicated by '*' notations and their values are given in Table 5.3. The line spectra are broadened with Gaussian functions of width 0.05 eV.

(DOS, see Fig. 5.8, Fig. 5.10 and Fig. 5.12), where there is no overlap between metal and ssDNA dependent orbitals. In addition, absorption peaks with lower transition energies correspond to the metal. This is also clear from DOS plot of Ag_{12}-ssDNA and Au_{12}-ssDNA (Fig. 5.10 and Fig. 5.12), where the highest occupied MO (HOMO), HOMO-1, lowest unoccupied MO (LUMO) and LUMO+1, LUMO+2 molecular orbitals are solely localized on metal cluster, whereas HOMO-2 is localized on ssDNA (see Fig. 5.13 for Ag_{12}-ssC_{12}). The interactions between the metal cluster and ssDNA in composites, red shifts the metal dependent absorption peaks, while, the absorption peaks of sequences, $ssdA_{12}$, $ssdT_{12}$, $ssdG_{12}$ and $ssdC_{12}$ are not affected in the composites. The computed absorption spectra values of ssDNA alone ($>$ 3 eV) and cluster alone (1-3 eV) of the nanocomposites are well comparable with

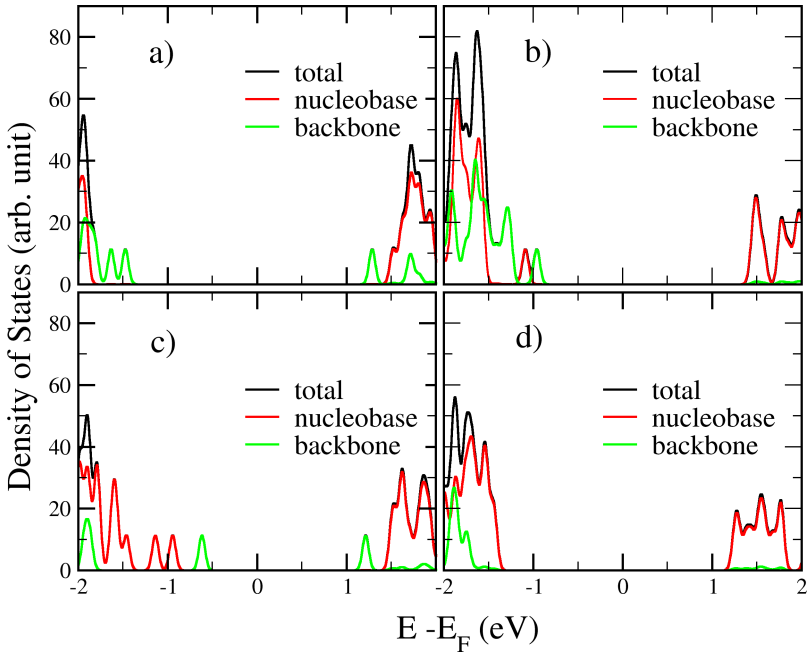

Figure 5.8: Electronic total density of states (DOS) and projected density of states (pDOS) for different ssDNA (ssA_{12} (a), ssT_{12} (b), ssG_{12} (c) and ssC_{12} (d) (black, red and green denote DOS, pDOS of nucleobase and backbone, respectively)). The energy (E) is scaled with respect to the Fermi energy (E_F).

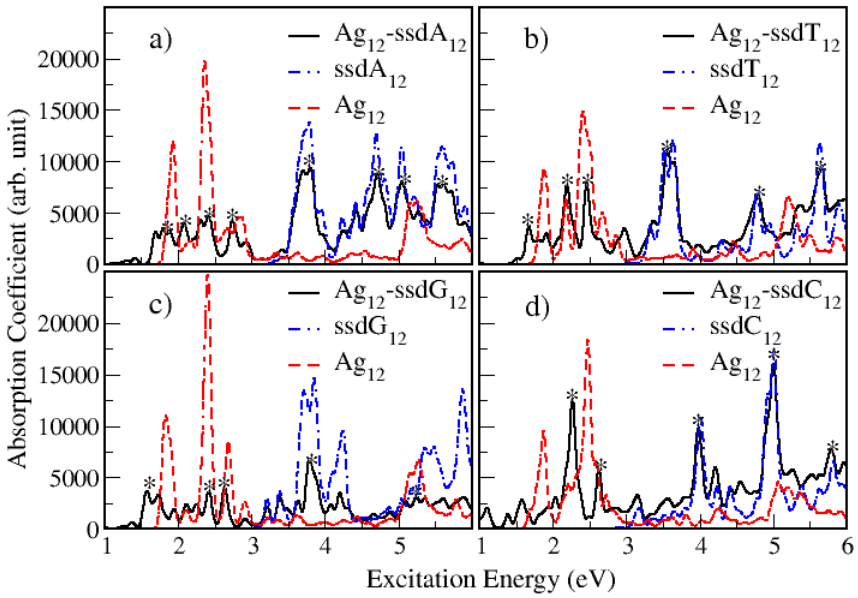

Figure 5.9: Computed absorption spectra of Ag_{12}-ssA_{12} (a), Ag_{12}-ssT_{12} (b), Ag_{12}-ssG_{12} (c) and Ag_{12}-ssC_{12} (d). High intensity peaks are indicated by '*' notations and their values are given in Table 5.3. The line spectra are broadened with Gaussian functions of width 0.05 eV.

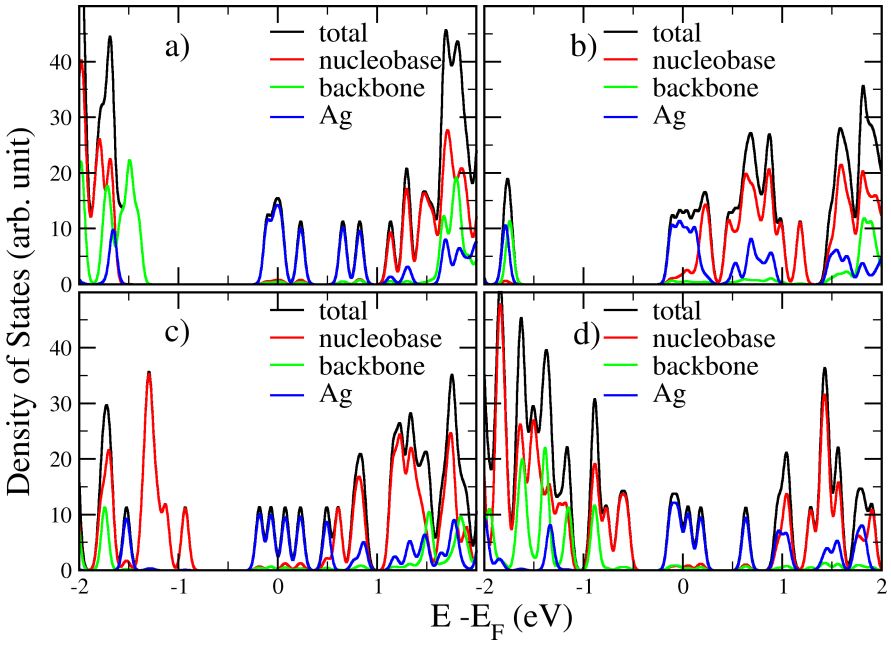

Figure 5.10: Electronic total density of states (DOS) and projected density of states (pDOS) of Ag_{12}-ssA_{12} (a), Ag_{12}-ssT_{12} (b), Ag_{12}-ssG_{12} (c) and Ag_{12}-ssC_{12} (d). The line spectra are broadened with Gaussian functions of width 0.05 eV.

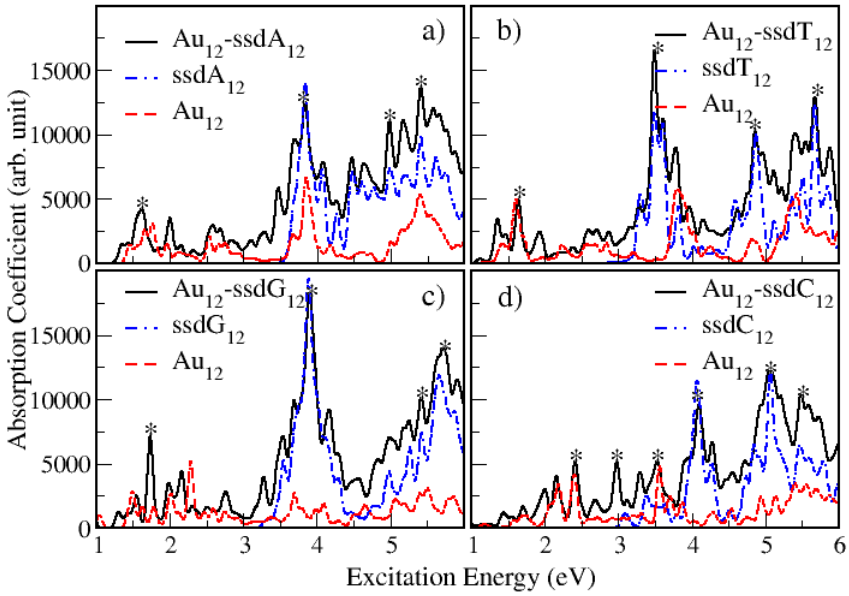

Figure 5.11: Computed absorption spectra of Au_{12}-ssA_{12} (a), Au_{12}-ssT_{12} (b), Au_{12}-ssG_{12} (c) and Au_{12}-ssC_{12} (d). High intensity peaks are indicated by '*' notations and their values are given in Table 5.3. The line spectra are broadened with Gaussian functions of width 0.05 eV.

already reported values (ssDNA > 3 eV, Ag_{12} 2.5-4 eV [304] and Au_{12} 1-3 eV [305]). The difference between the Ag_{12} absorption spectra value from the work of ref. [304] and ours is due to the different shape of the clusters in presence of nucleobases.

The computed four peaks (2.27 eV, 2.67 eV, 3.99 eV, and 5.00 eV) for Ag_{12}-$ssdC_{12}$ (Fig. 5.9d) are in good agreement with experimental (2.14 eV, 2.82 eV, 3.65 eV, 4.43 eV) [286] values. In fact, the small discrepancy in comparison to the experimental values could be due to the absence of explicit solvent and ions in the DFT calculations. The difference in size and stoichiometry of the metal clusters used in current study can also be the reason for this discrepancy. Our results suggest that the first two peaks arise from

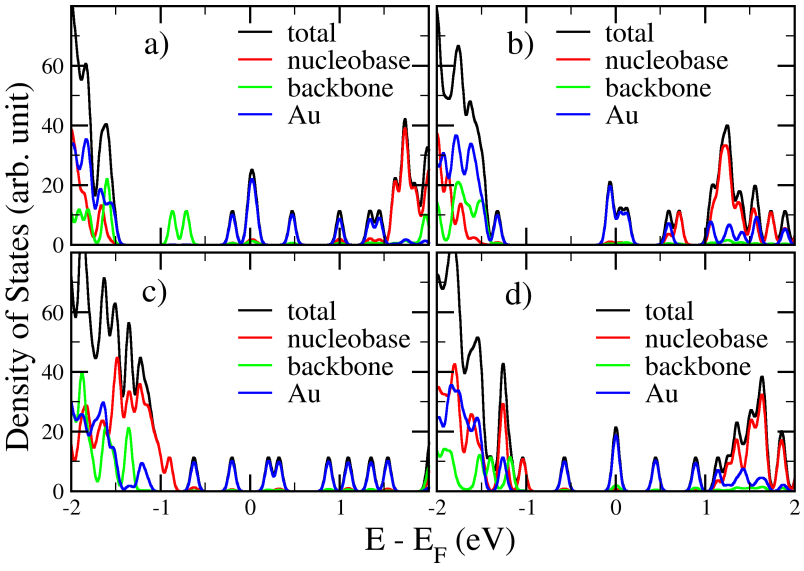

Figure 5.12: Electronic total density of states (DOS) and projected density of states (pDOS) of Au_{12}-ssA_{12} (a), Au_{12}-ssT_{12} (b), Au_{12}-ssG_{12} (c) and Au_{12}-ssC_{12} (d). The line spectra are broadened with Gaussian functions of width 0.05 eV.

the metal dependent orbitals while the second two peaks at higher energy originate due to the π-π^* transition from ssDNA scaffold in the absorption spectra.

5.4 Conclusions

The aim of this work is to understand the interaction between the silver (Ag_{12})/ gold (Au_{12}) clusters and various ssDNA sequences. Our calculations show that the metal clusters interact with ssDNA ($ssdA_{12}$, $ssdT_{12}$, $ssdG_{12}$ and $ssdC_{12}$) *via* both π-stacking or/and specific atom (Nitrogen and/or Oxygen, Fig. 5.3) of nucleobases. The observed π-stacking proves that the complete sequences are necessary in order to understand the interaction between ssDNA and metal clusters. Among the four sequences, $ssdG_{12}$ binds strongly

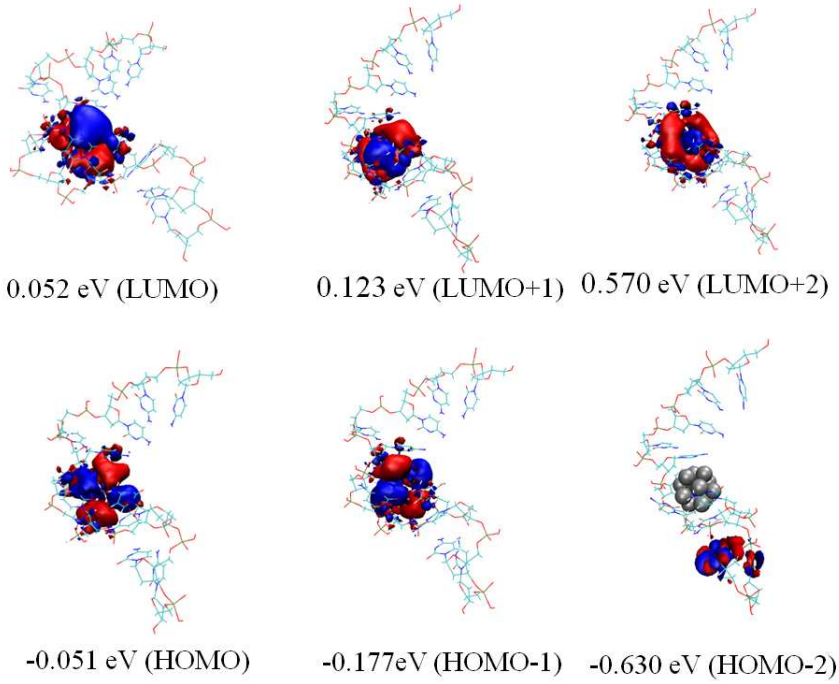

Figure 5.13: Highest occupied molecular orbital (HOMO) and lowest unoccupied molecular orbital (LUMO) of Ag_{12}-$ssdC_{12}$. Orbital energy is scaled with respect to Fermi-energy (E_F).

with silver (Ag_{12}) cluster and $ssdA_{12}$ with gold (Au_{12}) clusters, due to the number of nucleobases near the metal clusters. In addition, our studies provide evidence that the $ssdT_{12}$ prefer to bind with Ag_{12} and Au_{12} cluster *via* specific atoms (O4) rather than π-stacking, while other ssDNAs prefer to bind *via* π-stacking. The computed absorption spectra values of ssDNA alone (>3 eV) and cluster alone (1-3 eV) are comparable with already reported values (ssDNA >3 eV, Ag_{12} 2.5-4 eV [304] and Au_{12} 1-3 eV [305]). Finally, the absorption spectra of the metal cluster-ssDNA complexes show that the metal (Ag_{12} and Au_{12}) dependent electronic transitions do not overlap with the ssDNA dependent electronic transitions. This is due to the absence of orbital overlap between the metal and ssDNA for the low energy excitations. The computed four peaks for Ag_{12}-$ssdC_{12}$ are well comparable with the experimental results.

Chapter 6

Kinetic and Folding Pathway of Human Telomeric G-quadruplex*

6.1 Introduction

G-quadruplex DNA structures formed by the self-assembly of guanine-rich poly-nucleotides have a major role in maintaining the ends of chromosomes, the telomere. [308] Human telomeric DNA consists of tandem repeats ($d[5' - T_2AG_3]_n$) for 5-8 kb in length toward the end of chromosome and terminates in a single-stranded 3′-overhang of 100-200 nucleobases in length. [309, 310] In G-quadruplex, four guanine nucleobases are held in a plane by Hoogsteen hydrogen-bonds (H-bonds) with each other that form a cyclic structure with

*Work reported in this chapter is submitted for publication: P. K. Samanta and S. K. Pati (2014)

a central cavity. Each guanine comes from one strand and hence, the quadruplex form a four stranded structure. Also the guanine planes are stabilized by non-polar interaction between the stacked tetrads and the electrostatic interaction involving monovalent cations (*e.g.*, K^+, Na^+) sandwiched between two quartets reduce the repulsion between the aromatic oxygen atoms in neighboring guanines. [7,37–39] It can regulate gene expression and has an important role in several aspects of metabolism, such as transcription termination, splicing and translations. [43–47] It also has recently received great interest because of possible targets for cancer therapy. [48] Also, the drugs that bind to specific quadruplex DNAs can be used for the treatment of a variety of pathological conditions including cancer. [55] In time of cell division the length of telomere decreases in normal somatic cells and hence these progressive decreases limit the proliferative potential of the cells. In contrast to normal cells, most of the human tumor cells have functional telomerase which elongates the telomere. [34] In addition, synthetic G-quadruplexes are used as drugs for treating cancer [49–52], prevention of thrombosis [53] and inhibition of HIV replication. [54]

G-quadruplex DNA inhibits telomerase activity. The dynamics of enzyme-catalyzed unwinding depends on the folding pathway of G-quadruplex. [311] Therefore, it is important to study the folding pathway of the G-quadruplex to understand the functions of telomeres.

The kinetics of folding and unfolding of G-quadruplexes have been studied with different experimental techniques, including circular dichroism (CD), differential scanning calorimetry, isothermal titration calorimetry, optical tweezers experiments [312–314] and theoretically with molecular dynamics

simulations [315–319]. There are several studies which reported the existence of triplex intermediate during the unfolding of G-quadruplex. [314,320] However, the folding pathway of the G-quadruplex has not been fully understood yet. Recently, Li *et al.* have employed magnetic tweezers to investigate the folding kinetics of single human telomeric G-quadruplex with the sequence $d[G_3(T_2AG_3)_3]$ in 100 mM Na^+ buffer. [321] Their results probe the existence of triplex intermediate in the folding pathway of the G-quadruplex. Motivated by the experimental work [321], we have performed steered molecular dynamics simulation for the details study of the folding kinetics of G-quadruplexes. The ends of the molecule are linked to Hookean spring serving as force sensors whose ends move in opposite direction with constant velocity as like experimental work by Li *et al.* [321]. The stereochemistry of the glycosidic bonds (syn or anti), directions of strands (parallel or antiparallel), molecularity, the sequence and topology of the loops connecting the G-quartets and the sequences flanking the G-tetrads lead to different 3D orientation of a G-quadruplex. Also, the stability and configurations of the quadruplex depends upon the presence of specific metal cations. [36] We have considered two metal ions (K^+ and Na^+) with two different monomolecular G-quadruplex configurations and have studied whether both of their folding kinetics have G-triplex intermediates or not by calculating free energy profile of the folding pathways.

6.2 Computational Methods

For our study, we have considered two different monomolecular quadruplexes, (i) human telomeric repeat (seq1=$d[AG_3(T_2AG_3)_3]$) G-quadruplex in Na^+ solution (PDB ID: 143D) [322] and (ii) human telomeric G-quadruplex (seq2=$d[A_3G_3(T_2AG_3)_3A_2]$) in K^+ solution (PDB ID: 2HY9) [323]. The quadruplexes were solvated in a box of $5.0 \times 5.0 \times 25.0\ nm^3$. We considered transferable intermolecular potential three points (TIP3P) model for water solvent. [299, 300] Appropriate numbers of Na^+ or K^+ ions were added to electro-neutralize the systems. Simulations were run in the NPT ensemble using leap-frog algorithm for integrating Newtons equation of motion at constant temperature (300 K) and pressure (1 bar). The temperature was kept constant at 300 K by velocity rescaling with a stochastic term [88] and the pressure was kept constant at 1 bar using isotropic coupling to a Berendsen barostat [87]. An integrations time step of 1.5 fs was used and van der Waals interactions were calculated using a cutoff of 1.4 nm. At a distance smaller than 1.4 nm, electrostatic interactions were calculated explicitly, whereas long-range electrostatic interactions were calculated by particle-mesh Ewald summation. [93] All bonds were constrained using the LINCS algorithm. [324] All the simulations were carried out using GROMACS-4.0.7 [97] molecular dynamics software package with amber99 force field [296]. Initially the high energy contacts between the atoms in the initial conformations were removed by minimizing the energy using the steepest decent method. Following that, NPT simulations were carried out for 1 ns to equilibrate the entire systems.

After equilibration, we fixed one end of the monomolecular G-quadruplex

and allow the other end to move only along z-axis. A guiding potential,

$$h(r;\lambda) = \frac{k}{2}[\zeta(r) - \lambda]^2 \tag{6.1}$$

was added to control the end-to-end distances, ζ. The parameter, λ, was varied between 0-10 nm. A force constant of k=1000 kJ mol^{-1} nm^{-2} with two different constant velocities (1 nm ns^{-1} and 10 nm ns^{-1}) were used for the steered molecular dynamics simulations. The MD trajectory was visualized by Visual Molecular Dynamics (VMD) software. [102] Free energy changes during the stretching were calculated based on umbrella sampling method. [96] The free energies were calculated using weighted histogram methods as ensemble average. [96, 325, 326]

6.3 Results and Discussion

6.3.1 Equilibrium Simulations

Seq1 in Na^+ solution forms a basket structure characterized by anti-parallel strands, two lateral loops and one diagonal loop. Whereas, seq2 (in K^+ solutions) forms propeller structure characterized by mixed parallel and anti-parallel strands with lateral loops only. After 1 ns NPT simulation, we find that 3 Na^+ and 3 K^+ ions are positioned with in the central channel of the G-quadruplex for seq1 and seq2, respectively (see Fig. 6.1). The initial configuration did not change much after NPT equilibration.

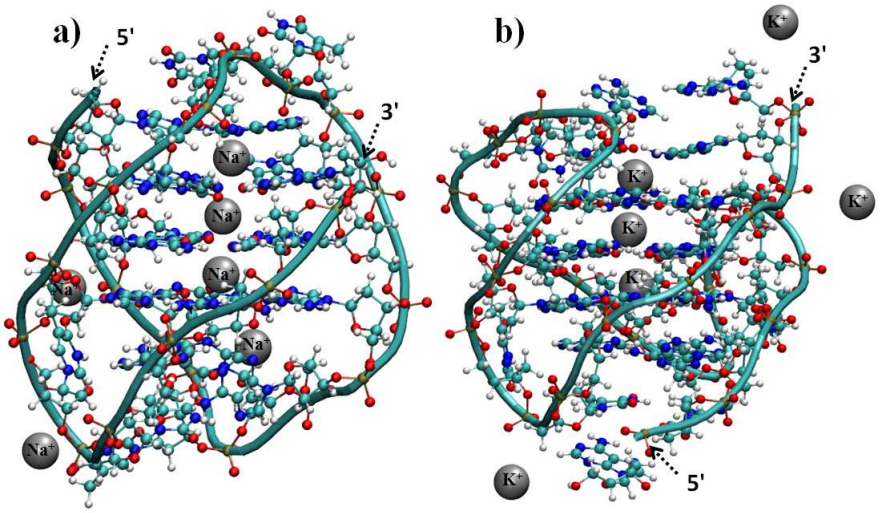

Figure 6.1: NPT equilibration structure of Na^+ solution (seq1 = $d[AG_3(T_2AG_3)_3]$, PDB ID: 143D) (a) and K^+ solution (seq2 = $d[A_3G_3(T_2AG_3)_3A_3]$, PDB ID: 2HY9) (b).

6.3.2 Force Induced Conformational Changes

The detailed structural changes along the pulling trajectory are described in Fig. 6.2 with pulling rate 1 nm ns^{-1}. The initial quadruplex structure (∼20 $\mathring{A}$) changed to stretched (unfolded) one which is ∼5-6 times of its initial contour length. With increase in the force (with time) the DNA extension length increases and finally becomes completely stretched. With increase in time and after ∼ 4 ns we find that initially, the one strand gets separated and then complete unfolding occurs. In fact, the unfolding occurs *via* G-triplex intermediates. This is because the G-triplex and G-tetrad are more stable than the GG base pair. [320] The triplex structures remain intact for around 4 ns (∼3 ns to ∼7 ns) and the alkali metal ions (K^+, Na^+) in those structures get sandwiched between the G-triplexes. Later on, after ∼ 9 ns the metal ions were released into the solvent and complete unfolding occurs.

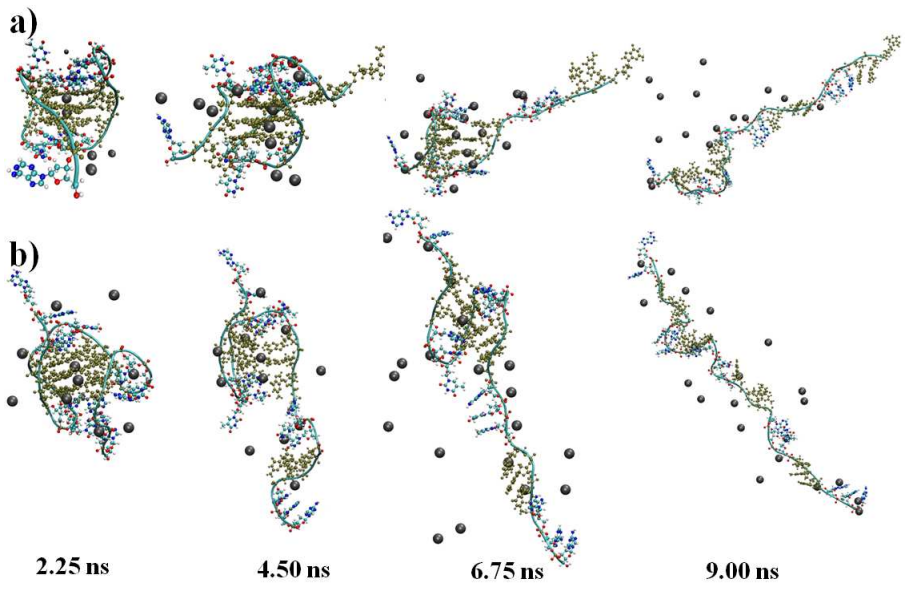

Figure 6.2: Evolution of the structure of G-quadruplex during the stretching of seq1 in Na^+ solution (a) and seq2 in K^+ solution (b).

6.3.3 Free Energy Profile

For the detailed understanding of the folding kinetics, we have calculated the potential of mean force (PMF) using umbrella sampling technique. Fig. 6.3 shows the potential of mean force (PMF) as a function of the end-to-end distance for both the G-quadruplexes; seq1 in Na^+ solution and seq2 in K^+ solution. Many different humps in case of G-quadruplex in Na^+ solution (Fig. 6.3) probe the complicated kinetics of folding pathway as found experimentally [314]. However, there is a simple kinetics of folding pathway for G-quadruplex in K^+ solution.

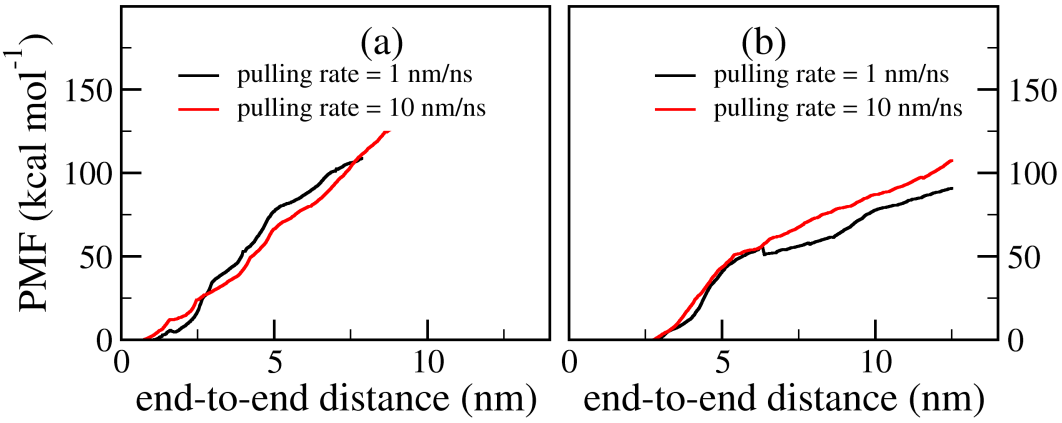

Figure 6.3: Potential of mean force (PMF) as a function of end-to-end distance (nm) for seq1 in Na^+ solution (a) and seq2 in K^+ solution (b).

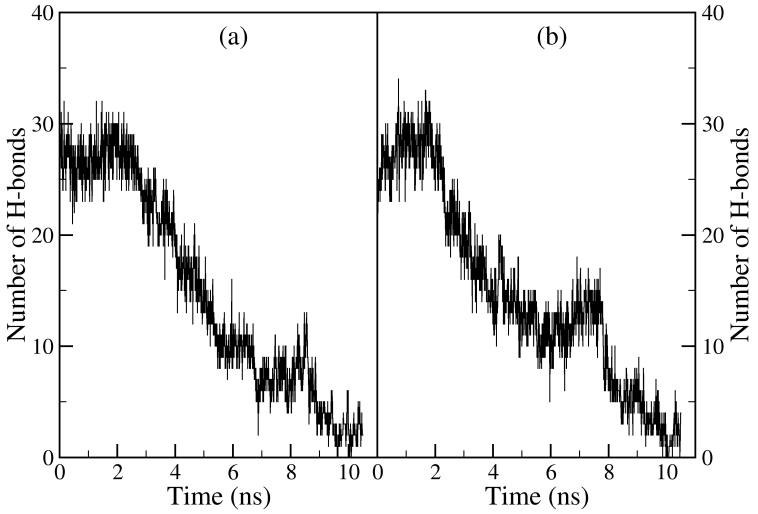

Figure 6.4: Number of H-bonds with time for seq1 in Na^+ solution (a) and seq2 in K^+ solution (b).

6.3.4 Hydrogen Bonding Profile

The hydrogen bond (H-bond) is represented as D-H...A where D is the donor atom and A is the acceptor atom. In case of DNA, D is nitrogen (N) atom and A is N or oxygen (O) atom. We used *g_hbond* GROMACS-4.0.7 utility to calculate number of H-bonds with cutoff D-A distance of 0.35 nm and cutoff angle 30°. With increase in the force, the DNA extension increases sharply and hence the number of H-bonds decreases (Fig. 6.4). For the complete stretched structure, the number of H-bonds becomes zero. For both seq1 in Na^+ solution (Fig. 6.4a) and seq2 in K^+ solution (Fig. 6.4b), we found that there was first decrease in the number of H-bonds, which implies that the G-quadruplex structure starts to break up. The number of H-bonds becomes stable around 7 ns of the MD simulation which reflects the existence of some intermediate conformation (Fig. 6.4) and the intermediate conformation after thorough analysis, is found to be the triplex conformation (Fig. 6.2).

6.4 Conclusions

To summarize, we have used atomistic molecular dynamics (MD) simulation to study the folding pathway of human telomeric G-quadruplex in presence of two different alkali metal ions (K^+ and Na^+). After NPT equilibration, we have found that 3 K^+ and 3 Na^+ ions are positioned within the central channel of the G-quadruplex to stabilize the overall structure. After equilibration, we fixed one end of the G-quadruplex and constrain the other end to move only along z-axis to make the quadruplex unfolded. We have found that unfolding occurs *via* G-triplex intermediates for both the ions solutions.

Therefore, our MD results suggest that the unfolding of G-quadruplex occurs *via* G-triplex intermediate, independent of the presence of cations (K^+, Na^+) and hence the special configuration of the G-quadruplexes.

Bibliography

[1] http://en.wikipedia.org/wiki/Pseudopotential .

[2] R. Dahm, Hum. Genet. **122**, 565 (2008).

[3] E. S. Lander, L. M. Linton, B. Birren, C. Nusbaum, M. C. Zody, J. Baldwin, K. Devon, K. Dewar, M. Doyle, W. FitzHugh, *et al.*, Nature **409**, 860 (2001).

[4] B. Budowle and A. van Daal, Biotechniques **46**, 339 (2009).

[5] K. Tanaka and M. Shionoya, Coord. Chem. Rev. **251**, 2732 (2007).

[6] S. Verma and F. Eckstein, Annu. Rev. Biochem. **67**, 99 (1998).

[7] D. E. Gilbert and J. Feigon, Curr. Opin. Struct. Biol. **9**, 305 (1999).

[8] S. Louise-May, P. Auffinger, and E. Westhof, Curr. Opin. Struct. Biol. **6**, 289 (1996).

[9] M. Zheng, A. Jagota, E. D. Semke, B. A. Diner, R. S. McLean, S. R. Lustig, R. E. Richardson, and N. G. Tassi, Nat. Mater. **2**, 338 (2003).

[10] M. Zheng, A. Jagota, M. S. Strano, A. P. Santos, P. Barone, S. G. Chou, B. A. Diner, M. S. Dresselhaus, R. S. Mclean, G. B. Onoa, *et al.*, Science **302**, 1545 (2003).

[11] I. D´iez and R. H. Ras, in *Advanced Fluorescence Reporters in Chemistry and Biology II* (Springer, 2010), vol. 9, pp. 307–332.

[12] J. D. Watson, F. H. Crick, *et al.*, Nature **171**, 737 (1953).

[13] R. E. Franklin and R. G. Gosling, Nature **171**, 740 (1953).

[14] M. H. F. Wilkins, A. R. Stokes, and H. R. Wilson, Nature **171**, 738 (1953).

[15] E. Chargaff, Experientia **6**, 201 (1950).

[16] J. Donohue and K. N. Trueblood, J. Mol. Biol. **2**, 363 (1960).

[17] O. Kennard and W. N. Hunter, Q. Rev. Biophys. **22**, 327 (1989).

[18] W. Saenger, *Principles of nucleic acid structure*, vol. 7 (Springer-Verlag New York, 1984).

[19] V. A. Bloomfield, D. M. Crothers, and I. Tinoco Jr, *Nucleic acids: structures, properties, and functions* (University science books, 2000).

[20] R. Wing, H. Drew, T. Takano, C. Broka, S. Tanaka, K. Itakura, and R. Dickerson, Nature **287**, 755.

[21] A. Ghosh and M. Bansal, Acta. Crystallogr. D Biol. Crystallogr. **59**, 620 (2003).

[22] A. Wang, G. J. Quigley, F. J. Kolpak, J. L. Crawford, J. H. Van Boom, G. van der Marel, and A. Rich, Nature **282**, 680 (1979).

[23] R. R. Sinden, *DNA structure and function* (Gulf Professional Publishing, 1994).

[24] A. Rich, A. H. Wang, and A. Nordheim, Nucleic Acid Research: Future Development p. 11 (1983).

[25] P. S. Ho, Proc. Natl. Acad. Sci. USA **91**, 9549 (1994).

[26] S. Shibutani, M. Takeshita, and A. P. Grollman, Nature **349**, 431 (1991).

[27] C. D. Claeboe, R. Gao, and S. M. Hecht, Nuc. Acids Res. **31**, 5685 (2003).

[28] R. W. Sinkeldam, N. J. Greco, and Y. Tor, Chem. Rev. **110**, 2579 (2010).

[29] D. Shin, R. W. Sinkeldam, and Y. Tor, J. Am. Chem. Soc. **133**, 14912 (2011).

[30] A. R. Hernández and E. T. Kool, Org. Lett. **13**, 676 (2011).

[31] G. H. Clever, C. Kaul, and T. Carell, Angew. Chem. Int. Ed. **46**, 6226 (2007).

[32] K. Tanaka, G. H. Clever, Y. Takezawa, Y. Yamada, C. Kaul, M. Shionoya, and T. Carell, Nat. Nanotechnol. **1**, 190 (2006).

[33] J. Müller, Nature **444**, 698 (2006).

[34] H. Yaku, T. Fujimoto, T. Murashima, D. Miyoshi, and N. Sugimoto, Chem. Commun. **48**, 6203 (2012).

[35] M. Fry, Frontiers in bioscience: a Journal and Virtual Library **12**, 4336 (2006).

[36] A. E. Engelhart, J. Plavec, O. Persil, and N. V. Hud, Nucleic Acid–Metal Ion Interactions. RSC Publishing pp. 118–153 (2009).

[37] R. Ida and G. Wu, J. Am. Chem. Soc. **130**, 3590 (2008).

[38] A. Bugaut, P. Murat, and S. Balasubramanian, J. Am. Chem. Soc. **134**, 19953 (2012).

[39] A. Jissy, U. Ashik, and A. Datta, J. Phys. Chem. C **115**, 12530 (2011).

[40] M. Webba da Silva, Chem. Eur. J. **13**, 9738 (2007).

[41] S. Burge, G. N. Parkinson, P. Hazel, A. K. Todd, and S. Neidle, Nuc. Acids Res. **34**, 5402 (2006).

[42] N. Zhang, A. Gorin, A. Majumdar, A. Kettani, N. Chernichenko, E. Skripkin, and D. J. Patel, J. Mol. Biol. **311**, 1063 (2001).

[43] H. Han and L. H. Hurley, Trends Pharmacol. Sci. **21**, 136 (2000).

[44] S. M. Kerwin, Curr. Pharm. Des. **6**, 441 (2000).

[45] J.-L. Mergny and C. Hélène, Nat. Med. **4**, 1366 (1998).

[46] A. Bugaut and S. Balasubramanian, Nuc. Acids Res. **40**, 4727 (2012).

[47] G. W. Collie and G. N. Parkinson, Chem. Soc. Rev. **40**, 5867 (2011).

[48] S. Neidle and M. A. Read, Biopolymers **56**, 195 (2000).

[49] D. J. Patel, A. T. Phan, and V. Kuryavyi, Nuc. Acids Res. **35**, 7429 (2007).

[50] C. R. Ireson and L. R. Kelland, Mol. Cancer Ther. **5**, 2957 (2006).

[51] S. Neidle and G. Parkinson, Nat. Rev. Drug Discov. **1**, 383 (2002).

[52] A. Siddiqui-Jain, C. L. Grand, D. J. Bearss, and L. H. Hurley, Proc. Natl. Acad. Sci. USA **99**, 11593 (2002).

[53] I. R. Krauss, A. Merlino, C. Giancola, A. Randazzo, L. Mazzarella, and F. Sica, Nuc. Acids Res. **39**, 7858 (2011).

[54] V. T. Mukundan, N. Q. Do, and A. T. Phan, Nuc. Acids Res. **39**, 8984 (2011).

[55] K. A. Olaussen, K. Dubrana, J. Domont, J.-P. Spano, L. Sabatier, and J.-C. Soria, Crit. Rev. Oncol. Hemat. **57**, 191 (2006).

[56] P. Hohenberg and W. Kohn, Phys. Rev. **136**, B864 (1964).

[57] W. Kohn and L. J. Sham, Phys. Rev. **140**, A1133 (1965).

[58] W. Kohn, Rev. Mod. Phys. **71**, 1253 (1999).

[59] D. Ceperley and B. Alder, Phys. Rev. Lett **45**, 566 (1980).

[60] J. P. Perdew, K. Burke, and M. Ernzerhof, Phys. Rev. Lett. **77**, 3865 (1996).

[61] J. P. Perdew and Y. Wang, Phys. Rev. B **45**, 13244 (1992).

[62] J. P. Perdew, J. Chevary, S. Vosko, K. A. Jackson, M. R. Pederson, D. Singh, and C. Fiolhais, Phys. Rev. B **46**, 6671 (1992).

[63] A. D. Becke, Phys. Rev. A **38**, 3098 (1988).

[64] C. Lee, W. Yang, and R. G. Parr, Phys. Rev. B **37**, 785 (1988).

[65] F. A. Hamprecht, A. J. Cohen, D. J. Tozer, and N. C. Handy, J. Chem. Phys. **109**, 6264 (1998).

[66] A. D. Boese, N. L. Doltsinis, N. C. Handy, and M. Sprik, J. Chem. Phys. **112**, 1670 (2000).

[67] A. D. Becke, J. Chem. Phys. **98**, 5648 (1993).

[68] T. Yanai, D. P. Tew, and N. C. Handy, Chem. Phys. Lett. **393**, 51 (2004).

[69] J.-D. Chai and M. Head-Gordon, Phys. Chem. Chem. Phys. **10**, 6615 (2008).

[70] G. Bachelet, D. Hamann, and M. Schlüter, Phys. Rev. B **26**, 4199 (1982).

[71] D. Vanderbilt, Phys. Rev. B **41**, 7892 (1990).

[72] M. Frisch, G. Trucks, H. B. Schlegel, G. Scuseria, M. Robb, J. Cheeseman, G. Scalmani, V. Barone, B. Mennucci, G. Petersson, *et al.*, Gaussian Inc., Wallingford (2009).

[73] M. W. Schmidt, K. K. Baldridge, J. A. Boatz, S. T. Elbert, M. S. Gordon, J. H. Jensen, S. Koseki, N. Matsunaga, K. A. Nguyen, S. Su, *et al.*, J. Comput. Chem. **14**, 1347 (1993).

[74] G. Te Velde, F. M. Bickelhaupt, E. J. Baerends, C. Fonseca Guerra, S. J. van Gisbergen, J. G. Snijders, and T. Ziegler, J. Comput. Chem. **22**, 931 (2001).

[75] J. M. Soler, E. Artacho, J. D. Gale, A. Garc´ia, J. Junquera, P. Ordejón, and D. Sánchez-Portal, J. Phys.: Condens. Matter. **14**, 2745 (2002).

[76] CPMD, http://www.cpmd.org/, Copyright IBM Corp 1990-2008, Copyright MPI f*ü*r Festk*ö*rperforschung Stuttgart, 1997–2001. .

[77] M. Elstner, D. Porezag, G. Jungnickel, J. Elsner, M. Haugk, T. Frauenheim, S. Suhai, and G. Seifert, Phys. Rev. B **58**, 7260 (1998).

[78] http://www.vasp.at/ .

[79] P. Giannozzi, S. Baroni, N. Bonini, M. Calandra, R. Car, C. Cavazzoni, D. Ceresoli, G. L. Chiarotti, M. Cococcioni, I. Dabo, *et al.*, J. Phys.: Condens. Matter. **21**, 395502 (2009).

[80] W. D. Cornell, P. Cieplak, C. I. Bayly, I. R. Gould, K. M. Merz, D. M. Ferguson, D. C. Spellmeyer, T. Fox, J. W. Caldwell, and P. A. Kollman, J. Am. Chem. Soc. **117**, 5179 (1995).

[81] A. D. MacKerell, D. Bashford, M. Bellott, R. Dunbrack, J. Evanseck, M. J. Field, S. Fischer, J. Gao, H. Guo, S. a. Ha, *et al.*, J. Phys. Chem. B **102**, 3586 (1998).

[82] A. D. MacKerell, M. Feig, and C. L. Brooks, J. Comput. Chem. **25**, 1400 (2004).

[83] A. D. MacKerell, N. Banavali, and N. Foloppe, Biopolymers **56**, 257 (2000).

[84] C. Oostenbrink, A. Villa, A. E. Mark, and W. F. Van Gunsteren, J. Comput. Chem. **25**, 1656 (2004).

[85] H. S. Hansen and P. H. Hünenberger, J. Comput. Chem. **32**, 998 (2011).

[86] L. Verlet, Phys. Rev. **159**, 98 (1967).

[87] H. J. Berendsen, J. P. M. Postma, W. F. van Gunsteren, A. DiNola, and J. Haak, J. Chem. Phys. **81**, 3684 (1984).

[88] G. Bussi, D. Donadio, and M. Parrinello, J. Chem. Phys. **126**, 014101 (2007).

[89] S. Nosé, J. Chem. Phys. **81**, 511 (1984).

[90] W. G. Hoover, Phys. Rev. A **31**, 1695 (1985).

[91] M. Parrinello and A. Rahman, J. Appl. Phys. **52**, 7182 (1981).

[92] P. P. Ewald, Ann. Physik **64**, 253 (1921).

[93] T. Darden, D. York, and L. Pedersen, J. Chem. Phys. **98**, 10089 (1993).

[94] U. Essmann, L. Perera, M. L. Berkowitz, T. Darden, H. Lee, and L. G. Pedersen, J. Chem. Phys. **103**, 8577 (1995).

[95] D. Frenkel and B. Smit, *Understanding molecular simulation: from algorithms to applications* (Access Online via Elsevier, 2001).

[96] J. Kästner, WIREs Comput. Mol. Sci. **1**, 932 (2011).

[97] B. Hess, C. Kutzner, D. Van Der Spoel, and E. Lindahl, J. Chem. Theory Comput. **4**, 435 (2008).

[98] P. Turner, Center for Coastal and Land-Margin Research, Oregon Graduate Institute of Science and Technology, Beaverton, OR (2005).

[99] T. Williams, C. Kelley, *et al.*, Official gnuplot documentation, http://sourceforge. net/projects/gnuplot (2010).

[100] R. Dennington, T. Keith, and J. Millam, Semichem Inc.: Shawnee Mission, KS (2009).

[101] A. Kokalj, J. Mol. Graphics Modell. **17**, 176 (1999).

[102] W. Humphrey, A. Dalke, and K. Schulten, J. Mol. Graph. **14**, 33 (1996).

[103] C. E. Crespo-Hernández, B. Cohen, P. M. Hare, and B. Kohler, Chem. Rev. **104**, 1977 (2004).

[104] R. B. Merrifield, J. Am. Chem. Soc. **85**, 2149 (1963).

[105] K. Tanaka and M. Shionoya, Coord. Chem. Rev. **251**, 2732 (2007).

[106] M. Barbatti, A. J. Aquino, J. J. Szymczak, D. Nachtigallová, P. Hobza, and H. Lischka, Proc. Natl. Acad. Sci. USA **107**, 21453 (2010).

[107] C. T. Middleton, K. de La Harpe, C. Su, Y. K. Law, C. E. Crespo-Hernández, and B. Kohler, Annu. Rev. Phys. Chem. **60**, 217 (2009).

[108] Z. Xu, D. R. Spring, and J. Yoon, Chem. Asian J. **6**, 2114 (2011).

[109] G. Brancolini and R. Di Felice, J. Chem. Phys. **134**, 205102 (2011).

[110] H. Liu, G. Li, H. Ai, J. Li, and Y. Bu, J. Phys. Chem. C **115**, 22547 (2011).

[111] H. Miyachi, T. Matsui, Y. Shigeta, and K. Hirao, Phys. Chem. Chem. Phys. **12**, 909 (2010).

[112] E. Shapir, G. Brancolini, T. Molotsky, A. B. Kotlyar, R. Di Felice, and D. Porath, Adv. Mater. **23**, 4290 (2011).

[113] P. K. Samanta, A. K. Manna, and S. K. Pati, Chem. Asian J. **7**, 2718 (2012).

[114] P. K. Samanta, G. Periyasamy, A. K. Manna, and S. K. Pati, J. Mater. Chem. **22**, 6774 (2012).

[115] J. A. Frey, R. Leist, and S. Leutwyler, J. Phys. Chem. A **110**, 4188 (2006).

[116] O. Khakshoor, S. E. Wheeler, K. Houk, and E. T. Kool, J. Am. Chem. Soc. **134**, 3154 (2012).

[117] A. Migliore, S. Corni, D. Varsano, M. L. Klein, and R. Di Felice, J. Phys. Chem. B **113**, 9402 (2009).

[118] J. Šponer, P. Jurecka, and P. Hobza, J. Am. Chem. Soc. **126**, 10142 (2004).

[119] D. Varsano, A. Garbesi, and R. Di Felice, J. Phys. Chem. B **111**, 14012 (2007).

[120] C. Boonlua, C. Vilaivan, H.-A. Wagenknecht, and T. Vilaivan, Chem. Asian J. **6**, 3251 (2011).

[121] G. Paragi, I. Pálinkó, C. Van Alsenoy, I. K. Gyémánt, B. Penke, and Z. Timár, New J. Chem. **26**, 1503 (2002).

[122] G. Paragi, E. Szájli, F. Bogár, L. Kovács, C. F. Guerra, and F. M. Bickelhaupt, New J. Chem. **32**, 1981 (2008).

[123] S. S. Mallajosyula and S. K. Pati, Angew. Chem. Int. Ed. **48**, 4977 (2009).

[124] N. J. Greco and Y. Tor, J. Am. Chem. Soc. **127**, 10784 (2005).

[125] L. Zhang, X. Chen, H. Liu, L. Han, R. I. Cukier, and Y. Bu, J. Phys. Chem. B **114**, 3726 (2010).

[126] L. Zhang, H. Li, X. Chen, R. I. Cukier, and Y. Bu, J. Phys. Chem. B **113**, 1173 (2009).

[127] F. Seela and M. Zulauf, Chem. Eur. J. **4**, 1781 (1998).

[128] F. Seela, M. Zulauf, M. Sauer, and M. Deimel, Helv. Chim. Acta **83**, 910 (2000).

[129] Y. Zhao, J. L. Knee, and A. M. Baranger, Bioorg. Chem. **36**, 271 (2008).

[130] M. Z. Zgierski, T. Fujiwara, W. G. Kofron, and E. C. Lim, Phys. Chem. Chem. Phys. **9**, 3206 (2007).

[131] A. D. Becke, J. Chem. Phys. **98**, 5648 (1993).

[132] B. Miehlich, A. Savin, H. Stoll, and H. Preuss, Chem. Phys. Lett. **157**, 200 (1989).

[133] Y. Zhao and D. G. Truhlar, Theor. Chem. Account **120**, 215 (2008).

[134] J.-D. Chai and M. Head-Gordon, J. Chem. Phys. **128**, 084106 (2008).

[135] G. Scalmani and M. J. Frisch, J. Chem. Phys. **132**, 114110 (2010).

[136] P. Jurečka, P. Nachtigall, and P. Hobza, Phys. Chem. Chem. Phys. **3**, 4578 (2001).

[137] P. K. Samanta, A. K. Manna, and S. K. Pati, J. Phys. Chem. B **116**, 7618 (2012).

[138] H. Y. Zhang, A. Calzolari, and R. Di Felice, J. Phys. Chem. B **109**, 15345 (2005).

[139] J. R. Blas, O. Huertas, C. Tabares, B. G. Sumpter, M. Fuentes-Cabrera, M. Orozco, P. Ordejón, and F. J. Luque, J. Phys. Chem. A **115**, 11344 (2011).

[140] S. R. Lynch, H. Liu, J. Gao, and E. T. Kool, J. Am. Chem. Soc. **128**, 14704 (2006).

[141] J. Gao, H. Liu, and E. T. Kool, Angew. Chem. Int. Ed. **44**, 3118 (2005).

[142] S. Boys and F. Bernardi, Mol. Phys. **19**, 553 (1970).

[143] S. Simon, M. Duran, and J. Dannenberg, J. Chem. Phys. **105**, 11024 (1996).

[144] P.-O. Löwdin, Rev. Mod. Phys. **35**, 724 (1963).

[145] P. Mohan, A. Datta, S. S. Mallajosyula, and S. K. Pati, J. Phys. Chem. B **110**, 18661 (2006).

[146] D. Varsano, R. Di Felice, M. A. Marques, and A. Rubio, J. Phys. Chem. B **110**, 7129 (2006).

[147] M. Fuentes-Cabrera, B. G. Sumpter, and J. C. Wells, J. Phys. Chem. B **109**, 21135 (2005).

[148] M. Gedik and A. Brown, J. Photochem. Photobiol. A **259**, 25 (2013).

[149] B. Kohler, J. Phys. Chem. Lett. **1**, 2047 (2010).

[150] G. Krishnan and O. Kühn, Chem. Phys. Lett. **435**, 132 (2007).

[151] M. Yang, Ł. Szyc, K. Rottger, H. Fidder, E. T. Nibbering, T. Elsaesser, and F. Temps, J. Phys. Chem. B **115**, 5484 (2011).

[152] G. Feitelson and M. Treinin, Computer **35**, 34 (2002).

[153] A. R. Hoelzel *et al.*, *Molecular genetic analysis of populations: a practical approach.* (IRL Press, 1992).

[154] N. G. Cooper, *The human genome project: Deciphering the blueprint of heredity* (University Science Books, 1994).

[155] J. Watson, T. Baker, S. Bell, A. Gann, M. Levine, and R. Losick, *Molecular Biology of the Gene, 5th ed.* (Peason Benjamin Cummings, 2004).

[156] P. Yakovchuk, E. Protozanova, and M. D. Frank-Kamenetskii, Nuc. Acids Res. **34**, 564 (2006).

[157] A. Ono, H. Torigoe, Y. Tanaka, and I. Okamoto, Chem. Soc. Rev. **40**, 5855 (2011).

[158] F. Wojciechowski and C. J. Leumann, Chem. Soc. Rev. **40**, 5669 (2011).

[159] M. J. Gait *et al.*, *Oligonucleotide synthesis: a practical approach* (IRL press Oxford, 1984).

[160] W. He, R. M. Franzini, and C. Achim, Progress in Inorg. Chem., Volume 55 pp. 545–612 (2008).

[161] Q. Shen, X. Guo, M. L. Steigerwald, and C. Nuckolls, Chem. Asian J **5**, 1040 (2010).

[162] K. Katoh, H. Isshiki, T. Komeda, and M. Yamashita, Chem. Asian J. **7**, 1154 (2012).

[163] K. Tanaka and M. Shionoya, J. Org. Chem. **64**, 5002 (1999).

[164] G. H. Clever and T. Carell, Angew. Chem. Int. Ed. **46**, 250 (2007).

[165] K. Tanaka, A. Tengeiji, T. Kato, N. Toyama, and M. Shionoya, Science **299**, 1212 (2003).

[166] K. Tanaka, Y. Yamada, and M. Shionoya, J. Am. Chem. Soc. **124**, 8802 (2002).

[167] Y. Takezawa, W. Maeda, K. Tanaka, and M. Shionoya, Angew. Chem. Int. Ed. **48**, 1081 (2009).

[168] T. Ihara, T. Ishii, N. Araki, A. W. Wilson, and A. Jyo, J. Am. Chem. Soc. **131**, 3826 (2009).

[169] D. Sen and W. Gilbert, Nature **344**, 410 (1990).

[170] V. A. Zakian, Science **270**, 1601 (1995).

[171] J. S. Lee, L. J. Latimer, and R. S. Reid, Biochem. Cell Biol. **71**, 162 (1993).

[172] D. O. Wood, M. J. Dinsmore, G. A. Bare, and J. S. Lee, Nuc. Acids Res. **30**, 2244 (2002).

[173] E. Meggers, P. L. Holland, W. B. Tolman, F. E. Romesberg, and P. G. Schultz, J. Am. Chem. Soc. **122**, 10714 (2000).

[174] K. Tanaka, A. Tengeiji, T. Kato, N. Toyama, M. Shiro, and M. Shionoya, J. Am. Chem. Soc. **124**, 12494 (2002).

[175] H. Weizman and Y. Tor, Chem. Commun. pp. 453–454 (2001).

[176] R. M. Franzini, R. M. Watson, G. K. Patra, R. M. Breece, D. L. Tierney, M. P. Hendrich, and C. Achim, Inorg. Chem. **45**, 9798 (2006).

[177] Z. Ma, F. Olechnowicz, Y. A. Skorik, and C. Achim, Inorg. Chem. **50**, 6083 (2011).

[178] D.-L. Popescu, T. J. Parolin, and C. Achim, J. Am. Chem. Soc. **125**, 6354 (2003).

[179] M. K. Schlegel, L.-O. Essen, and E. Meggers, J. Am. Chem. Soc. **130**, 8158 (2008).

[180] R. M. Watson, Y. A. Skorik, G. K. Patra, and C. Achim, J. Am. Chem. Soc. **127**, 14628 (2005).

[181] P. Aich, S. L. Labiuk, L. W. Tari, L. J. Delbaere, W. J. Roesler, K. J. Falk, R. P. Steer, and J. S. Lee, J. Mol. Biol. **294**, 477 (1999).

[182] E. Braun, Y. Eichen, U. Sivan, and G. Ben-Yoseph, Nature **391**, 775 (1998).

[183] T. Carell, C. Behrens, and J. Gierlich, Org. Biomol. Chem. **1**, 2221 (2003).

[184] J. C. Genereux and J. K. Barton, Chem. Rev. **110**, 1642 (2009).

[185] F. D. Lewis, T. Wu, Y. Zhang, R. L. Letsinger, S. R. Greenfield, and M. R. Wasielewski, Science **277**, 673 (1997).

[186] G. Taubes, Science **275**, 1420 (1997).

[187] S. Liu, G. H. Clever, Y. Takezawa, M. Kaneko, K. Tanaka, X. Guo, and M. Shionoya, Angew. Chem. Int. Ed. **50**, 8886 (2011).

[188] B. Liu, A. J. Bard, C.-Z. Li, and H.-B. Kraatz, J. Phys. Chem. B **109**, 5193 (2005).

[189] J. Richter, Physica E Low Dimens. Sys. Nanostruct. **16**, 157 (2003).

[190] G. H. Clever, S. J. Reitmeier, T. Carell, and O. Schiemann, Angew. Chem. Int. Ed. **49**, 4927 (2010).

[191] R. Freeman, T. Finder, and I. Willner, Angew. Chem. Int. Ed. **48**, 7818 (2009).

[192] J. Müller, Metallomics **2**, 318 (2010).

[193] P. Wang, C.-H. Leung, D.-L. Ma, W. Lu, and C.-M. Che, Chem. Asian J. **5**, 2271 (2010).

[194] G. Brancolini and R. Di Felice, J. Phys. Chem. B **112**, 14281 (2008).

[195] M. Fuentes-Cabrera, B. G. Sumpter, J. E. Šponer, J. Šponer, L. Petit, and J. C. Wells, J. Phys. Chem. B **111**, 870 (2007).

[196] S. S. Mallajosyula and S. K. Pati, J. Phys. Chem. B **111**, 13877 (2007).

[197] S. Johannsen, N. Megger, D. Böhme, R. K. Sigel, and J. Müller, Nat. Chem. **2**, 229 (2010).

[198] P. J. Hay and W. R. Wadt, J. Chem. Phys. **82**, 270 (1985).

[199] P. J. Hay and W. R. Wadt, J. Chem. Phys. **82**, 299 (1985).

[200] W. R. Wadt and P. J. Hay, J. Chem. Phys. **82**, 284 (1985).

[201] D. Andrae, U. Haeussermann, M. Dolg, H. Stoll, and H. Preuss, Theor. Chim. Acta. **77**, 123 (1990).

[202] A. E. Reed, R. B. Weinstock, and F. Weinhold, J. Chem. Phys. **83**, 735 (1985).

[203] O. F. Sankey and D. J. Niklewski, Phys. Rev. B **40**, 3979 (1989).

[204] S. S. Alexandre, B. J. Murta, J. M. Soler, and F. Zamora, Phys. Rev. B **84**, 045413 (2011).

[205] A. Hübsch, R. G. Endres, D. L. Cox, and R. R. Singh, Phys. Rev. Lett. **94**, 178102 (2005).

[206] S. S. Mallajosyula, J. Lin, D. Cox, S. Pati, and R. Singh, Phys. Rev. Lett. **101**, 176805 (2008).

[207] S. S. Mallajosyula, P. Parida, and S. K. Pati, J. Mater. Chem. **19**, 1761 (2009).

[208] F. C. Bernstein, T. F. Koetzle, G. J. Williams, E. F. Meyer Jr, M. D. Brice, J. R. Rodgers, O. Kennard, T. Shimanouchi, and M. Tasumi, J. Mol. Biol. **112**, 535 (1977).

[209] C. D. Churchill and S. D. Wetmore, Phys. Chem. Chem. Phys. **13**, 16373 (2011).

[210] D. Kosenkov, L. Gorb, O. V. Shishkin, J. Šponer, and J. Leszczynski, J. Phys. Chem. B **112**, 150 (2008).

[211] V. Labet, C. Morell, A. Grand, J. Cadet, P. Cimino, and V. Barone, Org. Biomol. Chem. **6**, 3300 (2008).

[212] P. Schyman, L. A. Eriksson, and A. Laaksonen, J. Phys. Chem. B **113**, 6574 (2009).

[213] P. Schyman, L. A. Eriksson, A. Laaksonen, *et al.*, Chem. Phys. Lett. **458**, 186 (2008).

[214] P. Schyman, R. bo Zhang, L. A. Eriksson, and A. Laaksonen, Phys. Chem. Chem. Phys. **9**, 5975 (2007).

[215] B. Xerri, C. Morell, A. Grand, J. Cadet, P. Cimino, and V. Barone, Org. Biomol. Chem. **4**, 3986 (2006).

[216] A. L. Millen, R. A. Manderville, and S. D. Wetmore, J. Phys. Chem. B **114**, 4373 (2010).

[217] Z. Dhaouadi, M. Nsangou, B. Hernández, F. Pflüger, J. Liquier, and M. Ghomi, Spectrochim. Acta. A **73**, 805 (2009).

[218] H. E. Herbert, M. D. Halls, H. P. Hratchian, and K. Raghavachari, J. Phys. Chem. B **110**, 3336 (2006).

[219] V. I. Poltev, V. M. Anisimov, V. I. Danilov, A. Deriabina, E. Gonzalez, D. Garcia, F. Rivas, A. Jurkiewicz, A. Leś, and N. Polteva, J. Mol. Struc.: Theochem. **912**, 53 (2009).

[220] V. I. Poltev, V. M. Anisimov, V. I. Danilov, T. Van Mourik, A. Deriabina, E. González, M. Padua, D. Garcia, F. Rivas, and N. Polteva, Int. J. Quantum Chem. **110**, 2548 (2010).

[221] A. L. Van Geet, J. Am. Chem. Soc. **94**, 5583 (1972).

[222] K. Leung, S. B. Rempe, and O. A. von Lilienfeld, J. Chem. Phys. **130**, 204507 (2009).

[223] H. R. Horton, L. A. Moran, K. G. Scrimgeour, M. D. Perry, and J. D. Rawn, *Principles of biochemistry* (Prentice Hall Upper Saddle River, 1996).

[224] S. Sakamoto, Y. Ohmachi, and M. Tomiya, in *J. Phys.: Conf. Ser.*, IOP Publishing (2007), vol. 61, pp. 1012–1016.

[225] T. Natsume, Y. Ishikawa, K. Dedachi, T. Tsukamoto, and N. Kurita, Int. J. Quantum Chem. **106**, 3278 (2006).

[226] H. Ehrenreich and M. H. Cohen, Phys. Rev. **115**, 786 (1959).

[227] J. Lindhard, Kgl. Danske Videnskab. Selskab Mat.-Fys. Medd. **28** (1954).

[228] P. Nozieres and D. Pines, Phys. Rev. **113**, 1254 (1959).

[229] C. K. Rowan and I. Paci, J. Phys. Chem. C **115**, 8316 (2011).

[230] S. S. Mallajosyula and S. K. Pati, Phys. Rev. Lett. **98**, 136601 (2007).

[231] J. Blumberger, L. Bernasconi, I. Tavernelli, R. Vuilleumier, and M. Sprik, J. Am. Chem. Soc. **126**, 3928 (2004).

[232] N. C. Seeman, Angew. Chem. Int. Ed. **37**, 3220 (1998).

[233] C. A. Mirkin, R. L. Letsinger, R. C. Mucic, and J. J. Storhoff, Nature **382**, 607 (1996).

[234] A. P. Alivisatos, K. P. Johnsson, X. Peng, T. E. Wilson, C. J. Loweth, M. P. Bruchez, and P. G. Schultz, Nature **382**, 609 (1996).

[235] Y. Takezawa and M. Shionoya, Acc. Chem. Res. **45**, 2066 (2012).

[236] E. T. Kool, Acc. Chem. Res. **35**, 936 (2002).

[237] G. H. Clever, Y. Söltl, H. Burks, W. Spahl, and T. Carell, Chem. Eur. J. **12**, 8708 (2006).

[238] J. B. Goodenough *et al.*, *Magnetism and the chemical bond*, vol. 98 (Interscience Publishers New York, 1963).

[239] O. Kahn *et al.*, *Molecular magnetism*, vol. 322 (WILEY-VCH New York, 1993).

[240] T. Vosch, Y. Antoku, J.-C. Hsiang, C. I. Richards, J. I. Gonzalez, and R. M. Dickson, Proc. Natl. Acad. Sci. USA **104**, 12616 (2007).

[241] J. Yu, S. Choi, and R. M. Dickson, Angew. Chem. Int. Ed. **48**, 318 (2009).

[242] C.-A. J. Lin, C.-H. Lee, J.-T. Hsieh, H.-H. Wang, J. K. Li, J.-L. Shen, W.-H. Chan, H.-I. Yeh, and W. H. Chang, J. Med. Biol. Eng. **29**, 276 (2009).

[243] I. D´iez and R. H. Ras, Nanoscale **3**, 1963 (2011).

[244] O. Kysil, K. Simonova, V. Frolov, E. Buzaneva, M. Köhler, G. Gobsch, U. Ritter, and P. Scharff, Mat.-wiss. u. Werkstofftech. **40**, 290 (2009).

[245] T.-H. Lee, J. I. Gonzalez, J. Zheng, and R. M. Dickson, Acc. Chem. Res. **38**, 534 (2005).

[246] C.-C. Huang, Z. Yang, K.-H. Lee, and H.-T. Chang, Angew. Chem. Int. Ed. **46**, 6824 (2007).

[247] T. G. Schaaff and R. L. Whetten, J. Phys. Chem. B **104**, 2630 (2000).

[248] I. L. Garzón, J. A. Reyes-Nava, J. Rodr´iguez-Hernández, I. Sigal, M. Beltrán, and K. Michaelian, Phys. Rev. B **66**, 073403 (2002).

[249] C. Gautier and T. Burgi, J. Am. Chem. Soc. **130**, 7077 (2008).

[250] C. E. Román-Velázquez, C. Noguez, and I. L. Garzón, J. Phys. Chem. B **107**, 12035 (2003).

[251] P. Crespo, R. Litrán, T. Rojas, M. Multigner, J. De la Fuente, J. Sánchez-López, M. Garcia, A. Hernando, S. Penadés, and A. Fernández, Phys. Rev. Lett. **93**, 087204 (2004).

[252] U. Maitra, B. Das, N. Kumar, A. Sundaresan, and C. Rao, ChemPhysChem **12**, 2322 (2011).

[253] R. C. Triulzi, M. Micic, S. Giordani, M. Serry, W.-A. Chiou, and R. M. Leblanc, Chem. Commun. pp. 5068–5070 (2006).

[254] C.-C. Huang, C.-K. Chiang, Z.-H. Lin, K.-H. Lee, and H.-T. Chang, Anal. Chem. **80**, 1497 (2008).

[255] D. Yang, M. J. Campolongo, N. Tran, T. Nguyen, R. C. Ruiz, J. S. Kahn, and D. Luo, WIREs Nanomed. Nanobiotechnol. **2**, 648 (2010).

[256] L. Hao, P. C. Patel, A. H. Alhasan, D. A. Giljohann, and C. A. Mirkin, Small **7**, 3158 (2011).

[257] R. Y. Tsien, Annu. Rev. Biochem. **67**, 509 (1998).

[258] W. C. Chan and S. Nie, Science **281**, 2016 (1998).

[259] J. Zheng and R. M. Dickson, J. Am. Chem. Soc. **124**, 13982 (2002).

[260] S.-I. Tanaka, J. Miyazaki, D. K. Tiwari, T. Jin, and Y. Inouye, Angew. Chem. Int. Ed. **50**, 431 (2011).

[261] J. Zhang, S. Xu, and E. Kumacheva, Adv. Mater. **17**, 2336 (2005).

[262] I. D´iez, M. Pusa, S. Kulmala, H. Jiang, A. Walther, A. S. Goldmann, A. H. Müller, O. Ikkala, and R. H. Ras, Angew. Chem. Int. Ed. **48**, 2122 (2009).

[263] E. G. Gwinn, P. O'Neill, A. J. Guerrero, D. Bouwmeester, and D. K. Fygenson, Adv. Mater. **20**, 279 (2008).

[264] J. T. Petty, J. Zheng, N. V. Hud, and R. M. Dickson, J. Am. Chem. Soc. **126**, 5207 (2004).

[265] J. T. Petty, C. Fan, S. P. Story, B. Sengupta, A. St. John Iyer, Z. Prudowsky, and R. M. Dickson, J. Phys. Chem. Lett. **1**, 2524 (2010).

[266] J. Sharma, H.-C. Yeh, H. Yoo, J. H. Werner, and J. S. Martinez, Chem. Commun. **46**, 3280 (2010).

[267] J.-Y. Kim and J.-S. Lee, Nano Lett. **9**, 4564 (2009).

[268] Y. Bao, C. Zhong, D. M. Vu, J. P. Temirov, R. B. Dyer, and J. S. Martinez, J. Phys. Chem. C **111**, 12194 (2007).

[269] C.-A. J. Lin, T.-Y. Yang, C.-H. Lee, S. H. Huang, R. A. Sperling, M. Zanella, J. K. Li, J.-L. Shen, H.-H. Wang, H.-I. Yeh, *et al.*, Acs Nano **3**, 395 (2009).

[270] R. Schreiber, S. Kempter, S. Holler, V. Schüller, D. Schiffels, S. S. Simmel, P. C. Nickels, and T. Liedl, Small **7**, 1795 (2011).

[271] R. J. Macfarlane, B. Lee, M. R. Jones, N. Harris, G. C. Schatz, and C. A. Mirkin, Science **334**, 204 (2011).

[272] B. Sengupta, C. M. Ritchie, J. G. Buckman, K. R. Johnsen, P. M. Goodwin, and J. T. Petty, J. Phys. Chem. C **112**, 18776 (2008).

[273] J. J. Gossett and S. C. Harvey, Nano Lett. **11**, 604 (2010).

[274] N. C. Seeman, Nature **421**, 427 (2003).

[275] H. Yan, S. H. Park, G. Finkelstein, J. H. Reif, and T. H. LaBean, Science **301**, 1882 (2003).

[276] J. Zheng, P. R. Nicovich, and R. M. Dickson, Annu. Rev. Phys. Chem. **58**, 409 (2007).

[277] M. H. Muhammed and T. Pradeep, in *Advanced fluorescence reporters in chemistry and biology II* (Springer, 2010), vol. 9, pp. 333–353.

[278] N. W. Ashcroft and N. D. Mermin, *Solid State Physics* (Rinehart and Winston, New York, 1976).

[279] M. B. Mohamed, V. Volkov, S. Link, and M. A. El-Sayed, Chem. Phys. Lett. **317**, 517 (2000).

[280] G. Boyd, Z. Yu, and Y. Shen, Phys. Rev. B **33**, 7923 (1986).

[281] C. D. Geddes, A. Parfenov, I. Gryczynski, and J. R. Lakowicz, J. Phys. Chem. B **107**, 9989 (2003).

[282] S. Link and M. A. El-Sayed, Annu. Rev. Phys. Chem. **54**, 331 (2003).

[283] J. Zheng, C. Zhang, and R. M. Dickson, Phys. Rev. Lett. **93**, 077402 (2004).

[284] T. Yamane and N. Davidson, Biochimica et Biophysica Acta (BBA)-Specialized Section on Nucleic Acids and Related Subjects **55**, 609 (1962).

[285] K. Luk, A. Maki, and R. Hoover, J. Am. Chem. Soc. **97**, 1241 (1975).

[286] C. M. Ritchie, K. R. Johnsen, J. R. Kiser, Y. Antoku, R. M. Dickson, and J. T. Petty, J. Phys. Chem. C **111**, 175 (2007).

[287] H.-C. Yeh, J. Sharma, H. Yoo, J. S. Martinez, and J. H. Werner, International Society for Optics and Photonics (2010), vol. 7576.

[288] V. Soto-Verdugo, H. Metiu, and E. Gwinn, J. Chem. Phys. **132**, 195102 (2010).

[289] E. Kryachko and F. Remacle, Nano Lett. **5**, 735 (2005).

[290] S. Piana and A. Bilic, J. Phys. Chem. B **110**, 23467 (2006).

[291] O.-S. Lee and G. C. Schatz, J. Phys. Chem. C **113**, 2316 (2009).

[292] O.-S. Lee and G. C. Schatz, J. Phys. Chem. C **113**, 15941 (2009).

[293] O.-S. Lee, T. R. Prytkova, and G. C. Schatz, J. Phys. Chem. Lett. **1**, 1781 (2010).

[294] J. P. Doye and D. J. Wales, New J. Chem. **22**, 733 (1998).

[295] D. Case, T. Darden, T. Cheatham III, C. Simmerling, J. Wang, R. Duke, R. Luo, R. Walker, W. Zhang, K. Merz, *et al.*, University of California, San Francisco, AMBER 11 (2010).

[296] W. D. Cornell, P. Cieplak, C. I. Bayly, I. R. Gould, K. M. Merz, D. M. Ferguson, D. C. Spellmeyer, T. Fox, J. W. Caldwell, and P. A. Kollman, J. Am. Chem. Soc. **117**, 5179 (1995).

[297] P. Guan, D. Mckenzie, and B. Pailthorpe, J. Phys.: Condens. Matter. **8**, 8753 (1996).

[298] T. Halicioglu and G. Pound, Physica status solidi (a) **30**, 619 (1975).

[299] M. W. Mahoney and W. L. Jorgensen, J. Chem. Phys. **112**, 8910 (2000).

[300] W. L. Jorgensen, J. Am. Chem. Soc. **103**, 335 (1981).

[301] C. Chipot and A. Pohorille, *Free energy calculations: theory and applications in chemistry and biology*, vol. 86 (Springer, 2007).

[302] R. R. Johnson, A. Johnson, and M. L. Klein, Small **6**, 31 (2010).

[303] R. M. Izatt, J. J. Christensen, and J. H. Rytting, Chem. Rev. **71**, 439 (1971).

[304] M. Harb, F. Rabilloud, D. Simon, A. Rydlo, S. Lecoultre, F. Conus, V. Rodrigues, and C. Félix, J. Chem. Phys. **129**, 194108 (2008).

[305] J. C. Idrobo, W. Walkosz, S. F. Yip, S. Öğüt, J. Wang, and J. Jellinek, Phys. Rev. B **76**(20), 205422 (2007).

[306] H. Häkkinen, M. Moseler, and U. Landman, Phys. Rev. Lett. **89**, 033401 (2002).

[307] S. Öğüt, J. C. Idrobo, J. Jellinek, and J. Wang, J. Clust. Sci. **17**, 609 (2006).

[308] R. H. Shafer and I. Smirnov, Biopolymers **56**, 209 (2000).

[309] E. H. Blackburn and J. G. Gall, J. Mol. Biol. **120**, 33 (1978).

[310] R. K. Moyzis, J. M. Buckingham, L. S. Cram, M. Dani, L. L. Deaven, M. D. Jones, J. Meyne, R. L. Ratliff, and J.-R. Wu, Proc. Natl. Acad. Sci. USA **85**, 6622 (1988).

[311] J. Liu, C. Chen, Y. Xue, Y.-h. Hao, and Z. Tan, J. Am. Chem. Soc. **132**, 10521 (2010).

[312] B. I. Kankia and L. A. Marky, J. Am. Chem. Soc. **123**, 10799 (2001).

[313] C. M. Olsen, W. H. Gmeiner, and L. A. Marky, J. Phys. Chem. B **110**, 6962 (2006).

[314] R. D. Gray and J. B. Chaires, Nuc. Acids Res. **36**, 4191 (2008).

[315] E. Gavathiotis and M. S. Searle, Org. Biomol. Chem. **1**, 1650 (2003).

[316] M. Cavallari, A. Calzolari, A. Garbesi, and R. Di Felice, J. Phys. Chem. B **110**, 26337 (2006).

[317] R. Štefl, T. E. Cheatham, N. Špačková, E. Fadrná, I. Berger, J. Koča, and J. Šponer, Biophys. J. **85**, 1787 (2003).

[318] R. D. Gray, J. Li, and J. B. Chaires, J. Phys. Chem. B **113**, 2676 (2009).

[319] H. Li, E.-h. Cao, and T. Gisler, Biochem. Biophys. Res. Commun. **379**, 70 (2009).

[320] T. Mashimo, H. Yagi, Y. Sannohe, A. Rajendran, and H. Sugiyama, J. Am. Chem. Soc. **132**, 14910 (2010).

[321] W. Li, X.-M. Hou, P.-Y. Wang, X.-G. Xi, and M. Li, J. Am. Chem. Soc. **135**, 6423 (2013).

[322] Y. Wang and D. J. Patel, Structure **1**, 263 (1993).

[323] J. Dai, C. Punchihewa, A. Ambrus, D. Chen, R. A. Jones, and D. Yang, Nuc. Acids Res. **35**, 2440 (2007).

[324] B. Hess, H. Bekker, H. J. Berendsen, and J. G. Fraaije, J. Comput. Chem. **18**, 1463 (1997).

[325] S. Kumar, J. M. Rosenberg, D. Bouzida, R. H. Swendsen, and P. A. Kollman, J. Comput. Chem. **13**, 1011 (1992).

[326] M. Souaille and B. Roux, Comput. Phys. Commun. **135**, 40 (2001).

Other Publications by the Author

1. *"Understanding the Binding Mechanism of Various Chiral SWCNTs and ssDNA: A Computational Study"*
   Siamkhanthang Neihsial, Ganga Periyasamy, **Pralok K. Samanta**, and Swapan K. Pati,
   J. Phys. Chem. B **116**, 14754-14759 (2012).

2. *"Molecular Architectonics of Stereochemically Constrained π-Complementary Functional Modules"*
   M. B. Avinash, **P. K. Samanta**, K. V. Sandeepa, S. K. Pati, and T. Govindaraju,
   Eur. J. Org. Chem., 5838-5847 (2013).

3. *"A Probe for Ratiometric Near-infrared Fluorescence and Colorimetric Hydrogen Sulfide Detection and Imaging in Live Cells"*
   D. Maity, R. Anand, **P. K. Samanta**, D. Karthigeyan, T. K. Kundu, S. K. Pati, and T. Govindaraju,
   RSC Adv., DOI: 10.1039/C4RA00401A (2014).